BCS Mean-Field Theory for Trapped Fermions

BCS-Theorie für Fermionen
im harmonischen Fallenpotenzial

André Becker

Masterarbeit in theoretischer Physik

unter Anleitung von

Priv.-Doz. Dr. Axel Pelster

Fachbereich Physik
TU Kaiserslautern
29. März 2021

Abstract

Macroscopic quantum effects have become a hot topic in the last decades and have been studied extensively. The BEC-BCS crossover offers the unique possibility to investigate two macroscopic quantum effects by a smooth crossover. On one side, there is the fermionic Bardeen-Cooper-Schrieffer (BCS) phase characterised by large Cooper pairs. On the other side two fermionic atoms form tightly-bound bosonic dimers, which occupy the ground state macroscopically denoted as Bose-Einstein condensation (BEC).
Cooling ^{6}Li within a harmonic potential and tuning the s-wave scattering length via Feshbach resonance, the BCS-BEC crossover is realised experimentally. This experiment is performed at the local university in the group of Artur Widera. Through our theoretical investigations, we work towards providing new insights and support in understanding quantitatively the experimental results.

For this purpose, we take into account the BCS mean-field theory and include the harmonic trapping potential via the local-density approximation (LDA). Based on this mean-field approach, we derive analytically and solve numerically the two algebraic self-consistency equations for both the order parameter and the particle-number density. The experimental determination of particle number and temperature has turned out to be difficult in the BCS limit. So far, estimating the temperature has only been possible via the adiabatic sweeping thermometry, where one sweeps isentropically from the BCS to the BEC limit.
In view of developing a direct thermometer in the BCS limit, the column density as the particle-number density integrated along an observational direction is the experimentally measurable quantity. To this end, our theoretical approach provides the possibility to study the impact of temperature and particle number on this column density.

Zusammenfassung

Makroskopische Quanteneffekte haben sich in den letzten Jahrzehnten zu einem bedeutsamen physikalischen Gebiet entwickelt und wurden ausgiebig experimentell und theoretisch untersucht. In diesem Kontext bietet der BEC-BCS Crossover die einzigartige Möglichkeit, zwei dieser makroskopischen Effekte durch einen kontinuierlichen Übergang zu verbinden. Der eine Grenzfall bezeichnet den fermionischen Limes und wird als Bardeen-Cooper-Schrieffer (BCS) Phase bezeichnet. Charakteristisch hierfür sind große Cooper-Paare von ^{6}Li-Atomen. Auf der anderen Seite ist der bosonische Bereich, indem sich zwei fermionische ^{6}Li Atome zu einem bosonischen Molekül zusammenschließen. Für hinreichend tiefe Temperaturen bevölkern diese den Grundzustand makroskopisch, was als Bose-Einstein-Kondensation (BEC) bezeichnet wird.
Werden nun ^{6}Li Atome innerhalb eines harmonischen Fallenpotenzials zu hinreichend tiefen Temperaturen gekühlt, so lässt sich die interatomare Wechselwirkung mit Hilfe der Feshbach-Resonanz regulieren und in der Folge der BEC-BCS Crossover auch experimentell realisieren. Dieses Experiment wird an der hiesigen TU Kaiserslautern in der Gruppe von Artur Widera durchgeführt. Durch unsere theoretischen Untersuchungen arbeiten wir darauf hin, neue Einsichten und Unterstützung bei der quantitativen Auswertung der experimentellen Daten zu bieten.

Hierzu führen wir eine BCS-Molekularfeldtheorie ein, in der wir durch die lokale Dichtenapproximation (LDA) das entsprechende experimentelle Fallenpotenzial berücksichtigen. Auf Grundlage dieses Ansatzes lassen sich analytisch zwei Selbstkonsistenzgleichungen herleiten, die wir numerisch lösen, um das chemische Potenzial und den Ordnungsparameter zu bestimmen. In dem BCS Bereich hat es sich als äußerst diffizil erwiesen, experimentell Teilchenzahl und Temperatur zu bestimmen. Bislang bestand die einzige Möglichkeit der Temperaturbestimmung darin, adiabatisch in den BEC Bereich durch einen isentropischen Übergang vorzudringen und dort die Temperatur zu bestimmen.
Im Hinblick auf ein direktes Thermometer im BCS Bereich wird die entlang einer Richtung integrierte Teilchenzahldichte untersucht. Im BCS Bereich ist dies die experimentell zugängliche Größe. Daher untersuchen wir theoretisch, wie sie von Teilchenzahl und Temperatur beeinflusst wird.

Contents

1. Introduction

In recent years, macroscopic quantum effects have become a hot topic, as can be read off from the six Nobel Prizes that have been awarded in this field since 1996. The first of these prizes was awarded for the discovery of the extraordinary phases of liquid ^{3}He [1], followed by the quantum Hall effect [2] and the discovery of Bose-Einstein condensation [3]. The theoretical description for superconductors and superfluids led to another Nobel price [4], as well as giant magnetoresistance [5] and finally topological quantum matter [6].
This raises the question of what constitutes a macroscopic quantum effect. Considering quantum mechanical effects on the microscopic length scale that lead to a collective behaviour, which is visible on a macroscopic length scale, we are dealing with a macroscopic quantum phenomenon. In the following we will give an overview of the history of macroscopic quantum effects in the low-temperature regime. In particular, we will discuss the history of Bose-Einstein condensation (BEC) and Bardeen-Cooper Schrieffer (BCS) theory, which are linked by the BEC-BCS crossover, which represents the unique opportunity to realize a smooth crossover between those two macroscopic quantum effects. This will provide a basis for the further course of this thesis, in which we will consider a BCS mean-field theory to investigate the fermionic regime of a corresponding ^{6}Li experiment, which is realised for instance in the group of Artur Widera at TU Kaiserslautern.

1.1. History of Low-Temperature Physics

At the beginning of the 20th century, the Dutch physicist H. Kamerlingh Onnes experimented with liquid helium and used it to cool mercury [7]. Hereby, he found out that the electrical resistance vanishes at a critical temperature of 4.2 K. Later, it was found out by W. Meissner and R. Ochsenfeld that below this critical temperature also the magnetic field is expelled from the sample [8]. Due to this observation, this effect, which has become known as superconductivity, cannot be explained classically. Thus, it was the first observation of a macroscopic quantum effect. Consequently, theorists searched for a suitable quantum mechanical explanation. A milestone was made by L. Cooper in 1956: Considering a small attractive interaction between two electrons at the Fermi edge, a paired state occurs, which is a consequence of the lower energy compared to the Fermi energy [9]. This small attractive interaction is a consequence of the electron-phonon interaction. In metals electrons can be described approximately by the free electron gas, whereas the positive ions are placed in a rigid lattice [7]. Thermal fluctuations excite lattice vibrations, which are called phonons and cause despite the preserve of a repulsive Coulomb interaction an additional attraction between electrons at larger distances. The magnitude of this interaction is quite weak, which corresponds to the observation that superconductivity appears at low temperatures, otherwise thermal energy breaks up the Cooper pairs. In the following year, J. Bardeen, L. Cooper and J. Schrieffer formulated a theory on the basis of a condensate of Cooper pairs at the Fermi edge, which is denoted as BCS theory [10]. With the help of this theory, the quantum phenomenon of superconductivity can be studied microscopically, which resulted in the Nobel Prize in 1972 for J. Bardeen, L. Cooper and J. Schrieffer [11].

In 1925, A. Einstein predicted for a gas of bosons a new state of matter, which gives

rise to an additional macroscopic many-body phenomenon: Considering the work of the Indian physicist S. Bose about the quantum statistics of massless photons [12], A. Einstein predicted the condensation of an ideal gas of massive bosons at temperatures close to absolute zero [13]. A first realisation was believed to be found in 1937 by P. Kapitsa, J. Allan and D. Misener for ^{4}He [14, 15]. Below a critical temperature ^{4}He behaves like a fluid with zero viscosity. This was the first observation of a new state of matter, denoted as superfluidity, which defines also a macroscopic quantum effect. One year later, F. London suggested this superfluid state to be the manifestation of Bose-Einstein condensation, since the expected critical temperature of this phenomenon agrees approximately with the temperature, where ^{4}He becomes superfluid [16]. However, in the further course it was found out that the basic requirement for a BEC is not fulfilled, i.e. the ground state is not occupied macroscopically due to the strong correlations between individual helium atoms [17]. To determine superfluidity, a criterion was presented by the Russian physicist L. Landau [18]. This criterion is not fulfilled by an ideal Bose gas due to the lacking interaction, thus it cannot become superfluid. Nevertheless, a deeper relationship between superfluidity and Bose-Einstein condensation was found, but turned out to be much more involved [17]. Besides the bosonic helium isotope ^{4}He, there is also a fermionic one ^{3}He, which was also investigated in the low-temperature regime during the 1970s by D. Osheroff, D. Lee and R. Richardson [19]. Analogously to the bosonic case, ^{3}He becomes superfluid, too. However, the critical temperature is lower compared to the bosonic case by more than three orders of magnitude. At first sight, this does not seem to do justice to the typical properties of fermionic atoms: Considering the fundamental Pauli exclusion principle, each available state for fermions, can be occupied only once [20]. This leads to the vivid description of fermions as antisocial particles in comparison to bosons as social particles. However, a generalisation of the previously motivated BCS theory leads to the explanation for superfluidity in the fermionic helium isotope. Two ^{3}He atoms form a Cooper pair and become finally bosonic, whereas in the standard BCS theory individual electrons form bosonic Cooper pairs, which condense below a critical temperature leading to superfluidity. This reveals a central relation between superconductivity and superfluidity: A superconductor can be interpreted as a charged superfluid, which provides a link between the two macroscopic quantum phenomena.

Still pending was the direct experimental realisation of the Bose-Einstein condensate. Decisive progress was made during the 1980s, when new cooling and trapping methods using laser light were initiated by C. Cohen-Tannoudji, S. Chu and W. Phillips [21]. Laser cooling provided the possibility to both cool and trap alkali atoms, since their optical transitions can be stimulated by the light of available lasers [17]. Thus, alkali atoms became appropriate candidates for the experimental realisation of the BEC. Finally, in 1995 the BEC was realised for ^{87}Rb by C. Wiemann and E. Cornell at JILA , as well as for ^{23}Na by W. Ketterle at MIT, which earned them the Nobel Prize in 2001. Although atoms form dilute gases at these low temperatures, the interaction strength turned out to be easily tunable due to a so-called Feshbach resonance [22]. This simple controllability led to the idea of the quantum simulator by R. Feynman already in 1982 [23]. The main idea is to simulate complex many-body systems, which are impossible to be calculated by a classical Turing machine. Consequently, experiments in this field became of great interest, since they provide the property to be seen as an "artificial solid" [24].

This motivates the question how fermionic atoms behave in this low-temperature regime. Especially, as in 2003 a Bose-Einstein condensate was realized experimentally by M. Greiner et al. for molecules of two ^{40}K [25] and by M. Zwierlein et al. [26], as well as in 2004 by T. Bourdel et al. [27] for two ^{6}Li molecules. The experimental realisation of

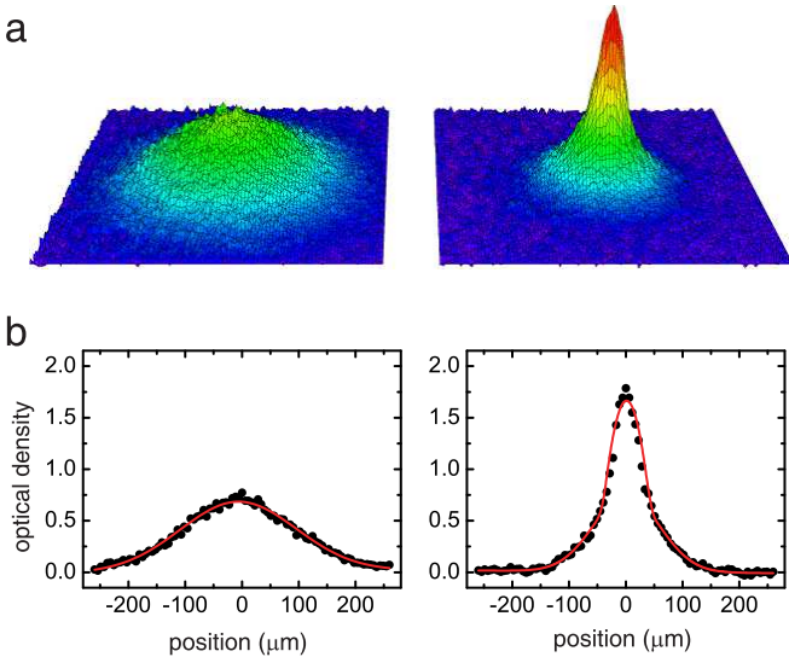

Figure 1.1.: Time-of-flight measurement of a ^{40}K molecular cloud for a temperature above the critical temperature for Bose-Einstein condensation on the left side and on the right below according to an experimental realisation from [25]. Panel **a** shows the surface plot of the optical density and panel **b** illustrates the cross-section through above images.

the BEC by M. Greiner et al. for ^{40}K is shown in Figure 1.1. At first sight, Bose-Einstein condensation of fermionic atoms seems contradictory. However, tuning the interaction strength between fermionic atoms provides the unique possibility to undergo a smooth crossover from the fermionic BCS regime to bosonic molecules in the BEC regime. This BCS-BEC crossover will be studied in more detail in the next section.

1.2. BCS-BEC Crossover

Since for the fermionic atoms ^{6}Li and ^{40}K a Bose-Einstein condensate has been observed as well as the BCS phase, both macroscopic phenomena need to be linked. A deeper investigation shows that there is no phase transition between both effects, but a smooth crossover which is denoted as BEC-BCS crossover.

In the following, we discuss the Feshbach resonance, which is the basis for the experimental investigation of the BEC-BCS crossover.

1.2.1. Feshbach Resonance

Regarding scattering processes in the low-temperature limit, a small velocity for the relative motion of the particles can be assumed [28]. Therefore, the interaction can be approximated by the s-wave scattering length, which determines the contact interaction strength

$$g = \frac{4\pi\hbar^2}{M} a_s. \tag{1.1}$$

To realise the BCS-BEC crossover experimentally a proper tool is needed, which allows to control this interatomic interaction strength. Therefore a constant magnetic field is ap-

plied to the fermionic atoms. The explanation for this phenomenon is known as Feshbach resonance: Considering scattering theory in nuclear physics, the American physicist H. Feshbach analysed multi-channel systems, consisting of at least one open and one closed channel. The open channel supports a scattering state, whereas the closed channel describes a bound state. Tuning the strength of the constant magnetic field allows us to control the coupling between open and closed channels due to the Zeeman effect. If the energy of the bound state and the scattering state coincide, the Feshbach resonance will occur. The Zeeman splitting of the energy levels of the atom

$$\Delta E_i = -\boldsymbol{\mu}_i \boldsymbol{B} \tag{1.2}$$

depends on the magnetic moment $\boldsymbol{\mu}_i$, which allows to control the relative energy between two channels. An approximative expression for the scattering length in the case of a Feshbach resonance is given by

$$a_{\mathrm{s}}(B) = a_{\mathrm{bg}} \left(1 - \frac{\Delta}{B - B_0}\right) \tag{1.3}$$

with the background scattering length a_{bg} and the width Δ of the resonance, which is inversely proportional to the difference of the magnetic moments between two atoms, one being in the open and one in the closed channel, respectively. The position of the resonance is denoted by the magnetic field B_0. From this we conclude that the scattering length diverges in the limit that the magnetic field B approaches to the resonant magnetic field B_0.

As mentioned previously, we set up a theory for ^{6}Li. Consequently, we point out, how the previous results can be implemented to our case. Therefore we show the ground and first excited state of ^{6}Li in Figure 1.2. Applying a magnetic field B larger than 500 G, ^{6}Li is fully polarised and consequently, all spins are aligned in the same direction for the lowest hyperfine states [29] .

1.2.2. History of BEC-BCS Crossover

At first glance, we can see in the BCS as well as in the BEC regime the occurrence of superfluidity for temperatures below a critical temperature. This indicates the existence of similarities between both macroscopic quantum effects.

First considerations regarding a smooth crossover from the BCS to the BEC regime were made in solid-state physics: D. Eagles took into account superconductivity in metals with a very low electron density, where a strong interaction between electrons leads to pairing effects without superconductivity [31]. Simultaneously, A. Legget discussed the possibility of a crossover between BCS and BEC for ^{3}He [32]. From this the BCS mean-field theory was extended by a variational approach to provide a qualitative suitable description for an arbitrary strength of the attractive interaction between electrons. The central difference between the standard BCS mean-field theory and the crossover is given for the zero-temperature case by the chemical potential, which is in the first case equal to the Fermi energy E_{F} and has to be solved self-consistently with the order parameter in the latter case [33]. This approach was generalized to finite temperatures by P. Nozières and S. Schmitt-Rink in 1985, who calculated the critical temperature T_C for superfluidity in the BCS limit for both weak and strong interaction [34]. Finally, in 1993 C. Sá de Melo, M. Randeria and J. Engelbrecht investigated the whole BEC-BCS crossover based on a path-integral formulation [35, 36]. Figure 1.3 show their result for the critical temperature

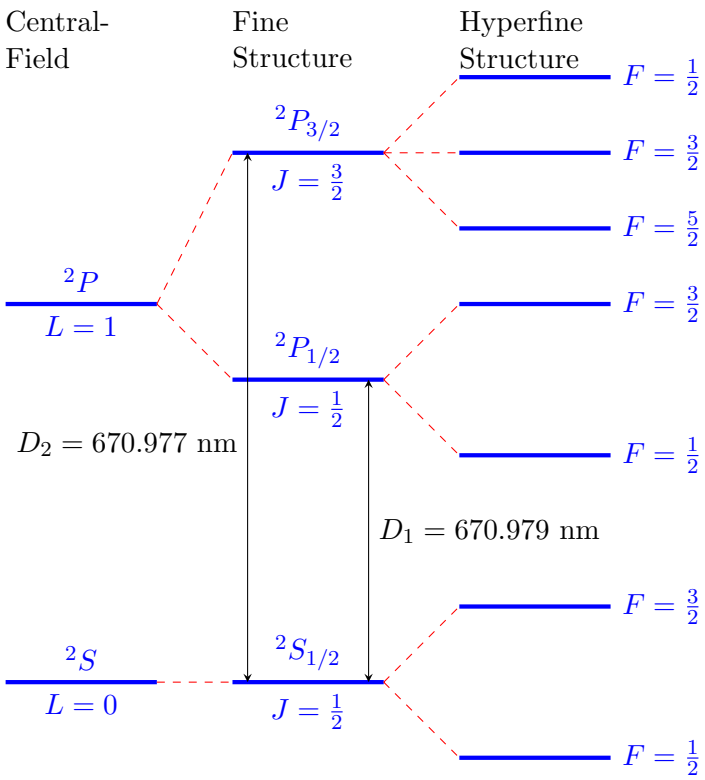

Figure 1.2.: Ground state and first excited state of ^{6}Li according to [29]. Laser light resonant to the D_2 transition ($2^2S_{1/2} \leftrightarrow 2^2P_{3/2}$) is applied for laser cooling [30]. The interaction between mixtures of the two spin states $|F = 1/2,\ m_F = +1/2\rangle$ and $|F = 1/2,\ m_F = -1/2\rangle$ of the ground state is controlled via Feshbach resonace, which allows the experimental realisation of the BEC-BCS crossover.

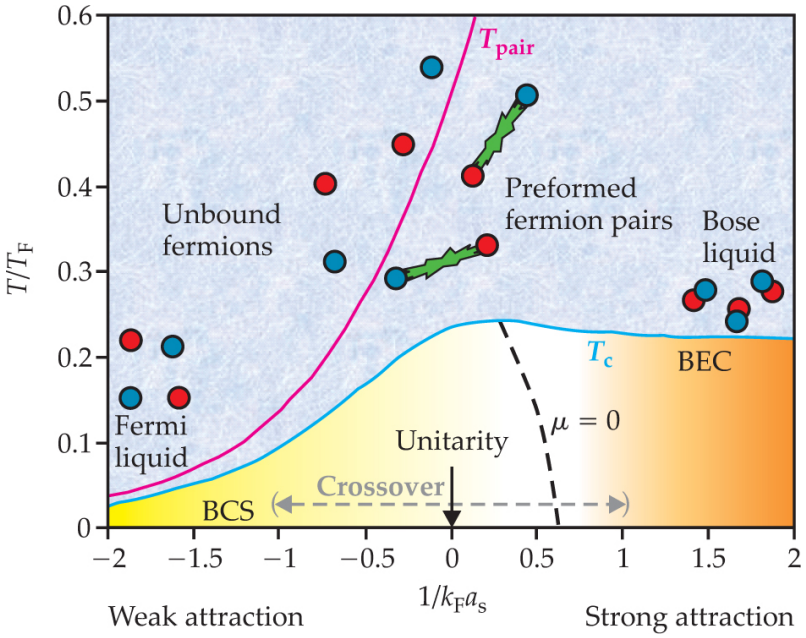

Figure 1.3.: The blue line shows the behaviour of the critical temperature during the BEC-BCS crossover within a beyond mean-field theory, whereas the pink curve shows the BCS mean-field theory. In the BCS-regime $1/a_s k_F < 0$ the fermionic atoms form large Cooper pairs, whereas in the BEC regime $1/a_s k_F > 0$ two ^{6}Li atoms create tightly bound molecules. These two regimes are linked by the strongly interacting unitary regime. Taken from [37].

as function of the dimensionless parameter $1/k_F a_s$, where a_s is the s-wave scattering length and k_F is the Fermi wave vector. Especially, the beyond mean-field approach, which considers the second-order correction, denoted as Gaussian fluctuations, offers the possibility to investigate the complete crossover. In contrast to that, the BCS mean-field theory leads to a critical temperature that diverges in the BEC limit. Experimentally, the s-wave scattering length is tunable with the previously introduced Feshbach resonance. Considering a weak attraction, which is characterised by small negative s-wave scattering lengths, we are in the limiting case $1/a_s k_F \to -\infty$. A strong attraction $a_s > 0$ is resolved by the formation of tightly bound molecules denoted as the BEC limit, which is characterised by $1/a_s k_F \to \infty$. Between these two regimes, the scattering length diverges at the threshold for bound state formation.

Starting with the experiments in 2003, the BEC-BCS crossover has been realised in several groups experimentally. Hereby, superfluidity was studied during the BEC-BCS crossover initiated by M. Zwierlein et al. [38], as we can see in Figure 1.4. The occurrence of quantised vortices proves the superfluidity, as it has been predicted by L. Onsager in 1949 [39].

After the experimental realisation of a lower dimensional BEC in 2001 in the group of W. Ketterle [40], the possibility of a BEC-BCS crossover in lower-dimension was taken into account. Since the superfluid transition in 2D is of the Berezinskii-Kosterlitz-Thouless type [41] and there is also no unitary regime, because pair binding occurs already at arbitrary weak attractive interactions [42], the 2D BEC-BCS crossover was investigated experimentally. Typically, these experiments are dealing with large particle-numbers $N > 10^5$. However, L. Bayha et al. realised in 2020 the phase transition from normal to superfluid for only six atoms of ^{6}Li [43].

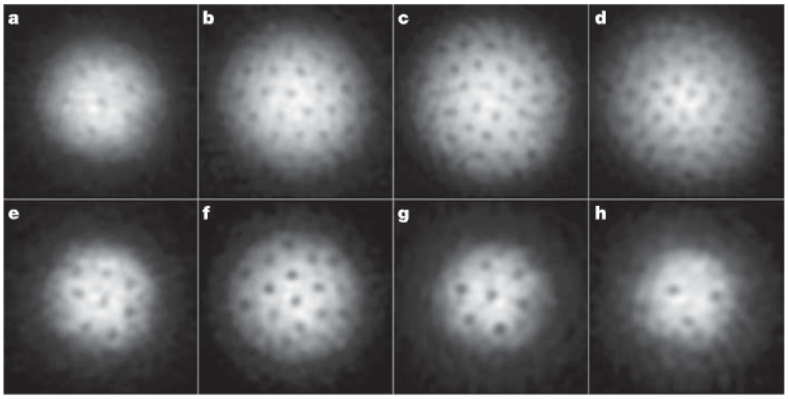

Figure 1.4.: Vortices in a gas of fermionic ^{6}Li atoms on the BEC- and BCS-side of the crossover. Stirring in the fermionic cloud followed by an equilibration leads to the formation of vortices. The magnetic fields start in the BEC limit and go to the BCS regime. They are given by 740 G **(a)**, 766 G **(b)**, 792 G **(c)**, 812 G **(d)**, 833 G **(e)**, 843 G **(f)**, 853 G **(g)** and 863 G **(h)**. Taken from [38].

At the local university, the BEC-BCS crossover has been realised in the group of Artur Widera for ^{6}Li [30]. Figure 1.5 shows the realisation of the BEC-BCS crossover. This setup allowed further investigations: Recently laser speckle potentials were taken into account to study localisation effects in the cloud of ^{6}Li atoms. Therefore the impact of this disorder potential on the measured column density, which denotes particle-number density integrated in z-direction, was determined in the BEC limit [44, 45].

1.3. Outline of Thesis

In this thesis, we set up the theoretical description for the corresponding ^{6}Li BEC-BCS crossover experiment, where we focus on the BCS limit. To this end, we consider a BCS mean-field approach, which leads primarily to the evaluation of two self-consistency equations. This investigation is split into two major parts:
First, we consider the homogeneous case and in the next step, we introduce a harmonic trapping potential in accordance with the experimental conditions. This gives us finally the possibility to relate the data from the experiment to our theoretical results. Especially, the experimental determination of both temperature and particle number is quite difficult. Therefore, our theoretical investigations should help to specify these two quantities.

In **chapter 2** we introduce a many-particle Hamiltonian to describe the interacting ^{6}Li atoms. To solve this Hamilton operator approximately, a mean-field approach is introduced, where we consider the Bogoliubov channel to treat the characteristic Cooper pairs of the BCS regime. At this point the order parameter for superfluidity caused by the presence of Cooper pairs is taken into account. Finally the Hamilton operator is transformed into the reciprocal space and diagonalised by a Bogoliubov transformation.
In mean-field theory the free energy becomes a function of the order parameter for superfluidity. In order to reduce the impact of the order parameter on the free energy, the principle of minimal sensitivity leads to an equation for determining the order parameter. Since we are dealing with the grand-canonical ensemble, the corresponding condition for the particle number leads to a second equation. Both equations for order parameter and particle number denote the two self-consistency equations.

Chapter 3 investigates the two self-consistency equations for the homogeneous case. First

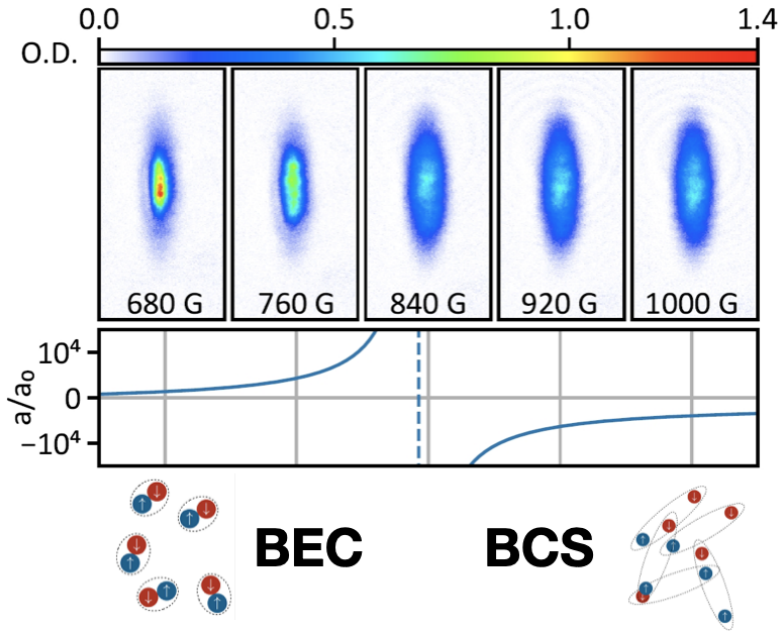

Figure 1.5.: Optical density distribution of ^{6}Li from [30]. Tuning the magnetic field strength allows to control the scattering length a_s according to the Feshbach resonance (1.3). On the left side, we can see the bosonic side, where fermionic ^{6}Li atoms form tightly bound dimers, which create a Bose-Einstein condensate, whereas the right side is the fermionic regime with the BCS phase. Both regimes are linked by the unitary Fermi gas, where the scattering length goes to infinity. Especially, we can see that the Fermi pressure is more repulsive compared to the bosonic interaction, since the density cloud in the BEC regime is narrower compared to the BCS regime.

of all, the zero-temperature limit is considered. Thus, the dependence of order parameter and chemical potential on the interaction strength is analysed perturbatively. This generates analytic approximations for both quantities in the BCS regime, which are compared to the corresponding numerical results. Furthermore, as the temperature dependence is important to obtain a possible thermometer for the experiment, the numerical investigation of the temperature dependence on chemical potential and order parameter is carried out subsequently.

In order to adapt the theoretical considerations of the homogeneous Fermi gas to the experiment, we use the local-density approximation (LDA) in **chapter 4** to introduce the harmonic trapping potential to our theory. Thus, we consider the two self-consistency equations with the trapping potential. This allows us to determine the spatial behaviour of the particle-number density based the particle-number equation, which is an experimentally accessible quantity. Since we are interested in figuring out the temperature dependence of the particle-number density, we start with the simple case of temperatures above the critical temperature, where the order parameter vanishes. In this case, we only have to evaluate one of the two self-consistency equations. From this analytic expressions for the particle-number density and the corresponding particle number can be generated by using polylogarithmic functions. Additionally, in the superfluid phase, which is characterised by temperatures below the critical temperature, we determine the spatial dependence of the order parameter.

These results enable us to compare the theoretical particle-number densities with the experimental ones. For this purpose, we compare the column density, which denotes the simply integrated particle number density and is measured in the experiment, with our theoretical expectations. First we empirically prove that LDA is appropriate to describe the experimental data. In the theoretical evaluation of the column density we distinguish between the superfluid and ideal Fermi gas to check the occurrence of superfluidity in the experiment. Especially, we vary the particle number and temperature in our theory and compare these results with the experimental data in **chapter 5**.

Chapter 6 summarises the results of this thesis and **chapter 7** gives an outlook which questions still remain open offering opportunities for future investigations.

2. BCS Mean-Field Theory

As pointed out in the introduction, considering ^{6}Li atoms in the ultracold regime for small negative scattering lengths, the condensation of Cooper pairs occurs, which allows us to work out the BCS mean-field theory [17]. For the sake of simplicity, we restrict us to the homogeneous case, i.e. we neglect any confining potential. To this end, we consider the order parameter in form of the energy gap as a variational parameter, which is appropriately determined from extremising the free energy. This leads to the self-consistency equations, which specify both the energy gap and the chemical potential.

2.1. Mean-Field Approach

To set up a suitable theoretical description, we introduce the following second quantised many-body Hamilton operator for fermions

$$\hat{H} = \int \mathrm{d}^3x \Bigg\{ \sum_{\sigma=\uparrow,\downarrow} \hat{\psi}_\sigma^\dagger(\boldsymbol{x}) \left[-\frac{\hbar^2}{2M}\Delta_\mathrm{L} - \mu \right] \hat{\psi}_\sigma(\boldsymbol{x}) + g\, \hat{\psi}_\uparrow^\dagger(\boldsymbol{x}) \hat{\psi}_\downarrow^\dagger(\boldsymbol{x}) \hat{\psi}_\downarrow(\boldsymbol{x}) \hat{\psi}_\uparrow(\boldsymbol{x}) \Bigg\}. \tag{2.1}$$

It consists of the kinetic term with mass M, the chemical potential μ as a consequence of using the grand-canonical ensemble to fix the particle number. Here the first line describes free fermions. The second part describes the contact interaction, which acts only between spin up and down fermions due to the Pauli principle and whose strength is denoted by g. A general anti-commutator for arbitrary field operators $\hat{A}$ and $\hat{B}$

$$\{\hat{A}, \hat{B}\} = \hat{A}\hat{B} + \hat{B}\hat{A} \tag{2.2}$$

leads in the case of our fermionic second-quantised operators to the following anti-commutator algebra

$$\left\{ \hat{\psi}_\sigma(\boldsymbol{x}), \hat{\psi}_{\sigma'}^\dagger(\boldsymbol{x'}) \right\} = \delta_{\sigma,\sigma'} \delta(\boldsymbol{x} - \boldsymbol{x'}), \tag{2.3}$$

$$\left\{ \hat{\psi}_\sigma(\boldsymbol{x}), \hat{\psi}_{\sigma'}(\boldsymbol{x'}) \right\} = \left\{ \hat{\psi}_\sigma^\dagger(\boldsymbol{x}), \hat{\psi}_{\sigma'}^\dagger(\boldsymbol{x'}) \right\} = 0. \tag{2.4}$$

Looking at the interaction part of our Hamilton operator, we realise that this term is quartic in the fermionic operators. Our final aim is to determine the free energy of the Hamiltonian (2.1). This is analytically only possible for a Hamilton operator, which is at most quadratic in the field operators. Consequently, we have to reduce our problem to a second-order one. Therefore we introduce a mean-field approach, which allows us to treat the fourth-order term by second-order terms [46]

$$\begin{aligned} \hat{\psi}_\uparrow^\dagger \hat{\psi}_\downarrow^\dagger \hat{\psi}_\downarrow \hat{\psi}_\uparrow \approx\ & \underbrace{\langle \hat{\psi}_\uparrow^\dagger \hat{\psi}_\uparrow \rangle \hat{\psi}_\downarrow^\dagger \hat{\psi}_\downarrow + \hat{\psi}_\uparrow^\dagger \hat{\psi}_\uparrow \langle \hat{\psi}_\downarrow^\dagger \hat{\psi}_\downarrow \rangle - \langle \hat{\psi}_\uparrow^\dagger \hat{\psi}_\uparrow \rangle \langle \hat{\psi}_\downarrow^\dagger \hat{\psi}_\downarrow \rangle}_{\text{Hartree channel}} \\ & \underbrace{- \langle \hat{\psi}_\uparrow^\dagger \hat{\psi}_\downarrow \rangle \hat{\psi}_\downarrow^\dagger \hat{\psi}_\uparrow - \hat{\psi}_\uparrow^\dagger \hat{\psi}_\downarrow \langle \hat{\psi}_\downarrow^\dagger \hat{\psi}_\uparrow \rangle + \langle \hat{\psi}_\uparrow^\dagger \hat{\psi}_\downarrow \rangle \langle \hat{\psi}_\downarrow^\dagger \hat{\psi}_\uparrow \rangle}_{\text{Fock channel}} \\ & \underbrace{+ \langle \hat{\psi}_\uparrow^\dagger \hat{\psi}_\downarrow^\dagger \rangle \hat{\psi}_\downarrow \hat{\psi}_\uparrow + \hat{\psi}_\uparrow^\dagger \hat{\psi}_\downarrow^\dagger \langle \hat{\psi}_\downarrow \hat{\psi}_\uparrow \rangle - \langle \hat{\psi}_\uparrow^\dagger \hat{\psi}_\downarrow^\dagger \rangle \langle \hat{\psi}_\downarrow \hat{\psi}_\uparrow \rangle}_{\text{Bogoliubov channel}}. \end{aligned} \tag{2.5}$$

Here the first line contains the normal particle-number expectation values in the Hartree channel, the second part describes the anormal particle-number expectation values in the Fock channel and lastly the anormal pairing expectation values in the Bogoliubov channel.
We derive this second-order approximation by considering all possible combinations of second-order terms following from the initial fourth-order term. According to the rules of combinatorics, this results in $(4-1)! = 6$ possibilities for our second-order terms. However, this raises the question about the third term in each channel. This term guarantees that the right- and left-side of the equation are equivalent under the formation of the expectation value. The different sign of the Fock channel is a consequence of the anti-commutator algebra (2.2).
An appropriate physical description for the Cooper pairs is given by the Bogoliubov channel. Consequently, we will plug in only this term to our Hamiltonian (2.1) to set up our mean-field description

$$\begin{aligned}\hat{H} \approx \hat{H}_{\mathrm{MF}} = \int \mathrm{d}^3x \Bigg\{ \sum_{\sigma=\uparrow,\downarrow} \hat{\psi}_\sigma^\dagger(\boldsymbol{x}) \Big[-\frac{\hbar^2}{2M}\Delta_L - \mu \Big] \hat{\psi}_\sigma(\boldsymbol{x}) \\ + \Delta^* \hat{\psi}_\downarrow(\boldsymbol{x})\hat{\psi}_\uparrow(\boldsymbol{x}) + \Delta \hat{\psi}_\uparrow^\dagger(\boldsymbol{x})\hat{\psi}_\downarrow^\dagger(\boldsymbol{x}) - \frac{\Delta^*\Delta}{g} \Bigg\}\end{aligned} \tag{2.6}$$

with the order parameter for pairing

$$\Delta = g\langle \hat{\psi}_\downarrow(\boldsymbol{x})\hat{\psi}_\uparrow(\boldsymbol{x})\rangle \tag{2.7}$$

$$\Delta^* = g\langle \hat{\psi}_\uparrow^\dagger(\boldsymbol{x})\hat{\psi}_\downarrow^\dagger(\boldsymbol{x})\rangle. \tag{2.8}$$

This order parameter allows to describe the possible phases. The case $\Delta = 0$ describes the normal Fermi phase and the non-vanishing case $\Delta \neq 0$ denotes the superfluid phase with the formation of Cooper pairs. However, we introduce in (2.7), (2.8) an expectation value, which is not yet defined. In the following, we have to determine this expectation value self-consistently.
Hence, we introduce the partition function

$$Z = \mathrm{Tr}\big\{ e^{-\beta \hat{H}} \big\}. \tag{2.9}$$

Since our Hamilton operator (2.1) is not solvable as explained above, the idea comes up to introduce our mean-field approach into the partition function due to the following identity

$$Z = \mathrm{Tr}\big\{ e^{-\beta[\hat{H}_{\mathrm{MF}} + (\hat{H} - \hat{H}_{\mathrm{MF}})]} \big\}. \tag{2.10}$$

Assuming that our mean-field approach estimates the initial Hamiltonian appropriately, the difference between the mean-field and the original Hamiltonian is small, so a perturbative treatment of the partition function is justified. In Appendix A we derive the mean-field approximation of the partition function (A.34)

$$Z_{\mathrm{MF}} = \mathrm{Tr}\left\{ e^{-\beta \hat{H}_{\mathrm{MF}}} \right\}. \tag{2.11}$$

Thus, we neglect in the following fluctuations and restrict ourselves to the mean-field theory. The general relation between free energy and partition function is given by

$$F = -\frac{1}{\beta} \ln Z. \tag{2.12}$$

Therefore, we obtain for the mean-field free energy

$$F_{\mathrm{MF}} = -\frac{1}{\beta}\ln Z_{\mathrm{MF}}. \tag{2.13}$$

Regarding the expansion of the free energy (A.42), we have performed a finite truncation of this series after zeroth order. As the full free energy F does not depend on the order parameter, truncating the expansion of the free energy at the mean-field level yields a function, which depends on the order parameter. To minimize the impact, we apply the principle of minimal sensitivity [47, 48], yielding the extremalisation condition

$$\frac{\partial F_{\mathrm{MF}}(\Delta,\Delta^*)}{\partial\Delta^*} = \frac{\partial F_{\mathrm{MF}}(\Delta,\Delta^*)}{\partial\Delta} = 0. \tag{2.14}$$

Thus, the order parameter becomes in this way a variational parameter. The implementation of this extremalisation condition

$$\begin{aligned}\frac{\partial F_{\mathrm{MF}}(\Delta,\Delta^*)}{\partial\Delta^*} &= \frac{1}{\beta}\frac{1}{Z_{\mathrm{MF}}}\mathrm{Tr}\left[\frac{\partial e^{-\beta H_{\mathrm{MF}}}}{\partial\Delta^*}\right] = -\left\langle\frac{\partial\hat{H}_{\mathrm{MF}}}{\partial\Delta^*}\right\rangle_{\mathrm{MF}} \\ &= -\langle\hat{\psi}_\downarrow(\boldsymbol{x})\hat{\psi}_\uparrow(\boldsymbol{x})\rangle_{\mathrm{MF}} + \frac{\Delta}{g}\end{aligned} \tag{2.15}$$

determines the order parameter

$$\Delta = g\langle\hat{\psi}_\downarrow(\boldsymbol{x})\hat{\psi}_\uparrow(\boldsymbol{x})\rangle_{\mathrm{MF}}. \tag{2.16}$$

Comparing (2.7) with (2.16) fixes the expectation value as the mean-field expectation value

$$\langle\bullet\rangle = \langle\bullet\rangle_{\mathrm{MF}}, \tag{2.17}$$

which is given by

$$\langle\bullet\rangle_{\mathrm{MF}} = \frac{\mathrm{Tr}\{\bullet e^{-\beta\hat{H}_{\mathrm{MF}}}\}}{Z_{\mathrm{MF}}}. \tag{2.18}$$

2.2. Bogoliubov-Transformation

In order to diagonalise the Hamiltonian (2.6), we introduce a Bogoliubov rotation. First of all, we transform the Hamilton operator to the reciprocal space. For this purpose, we consider the Fourier series of our second quantised fermionic operators

$$\hat{\psi}_\sigma(\boldsymbol{x}) = \frac{1}{\sqrt{V}}\sum_{\boldsymbol{k}} e^{i\boldsymbol{k}\boldsymbol{x}}\hat{a}_{\boldsymbol{k},\sigma}, \quad \hat{a}_{\boldsymbol{k},\sigma} = \frac{1}{\sqrt{V}}\int \mathrm{d}^3x e^{-i\boldsymbol{k}\boldsymbol{x}}\hat{\psi}_\sigma(\boldsymbol{x}), \tag{2.19}$$

$$\hat{\psi}^\dagger_\sigma(\boldsymbol{x}) = \frac{1}{\sqrt{V}}\sum_{\boldsymbol{k}} e^{-i\boldsymbol{k}\boldsymbol{x}}\hat{a}^\dagger_{\boldsymbol{k},\sigma}, \quad \hat{a}^\dagger_{\boldsymbol{k},\sigma} = \frac{1}{\sqrt{V}}\int \mathrm{d}^3x e^{i\boldsymbol{k}\boldsymbol{x}}\hat{\psi}^\dagger_\sigma(\boldsymbol{x}), \tag{2.20}$$

which fulfill the corresponding commutation relations

$$\left\{\hat{a}_{\boldsymbol{k},\sigma},\hat{a}_{\boldsymbol{k}',\sigma'}\right\} = \left\{\hat{a}^\dagger_{\boldsymbol{k},\sigma},\hat{a}^\dagger_{\boldsymbol{k}',\sigma'}\right\} = 0, \tag{2.21}$$

$$\left\{\hat{a}_{\boldsymbol{k},\sigma},\hat{a}^\dagger_{\boldsymbol{k}',\sigma'}\right\} = \delta_{\sigma,\sigma'}\delta_{\boldsymbol{k},\boldsymbol{k}'}. \tag{2.22}$$

These new fermionic operators lead to the Hamilton operator

$$\hat{H}_{\mathrm{MF}} = \sum_{\boldsymbol{k}}\left\{\hat{a}^\dagger_{\boldsymbol{k},\sigma}\hat{a}_{\boldsymbol{k},\sigma}\left[\frac{\hbar^2\boldsymbol{k}^2}{2M}-\mu\right] + \Delta^*\hat{a}_{-\boldsymbol{k},\downarrow}\hat{a}_{\boldsymbol{k},\uparrow} + \Delta\hat{a}^\dagger_{\boldsymbol{k},\uparrow}\hat{a}^\dagger_{-\boldsymbol{k},\uparrow}\right\} - V\frac{|\Delta|^2}{g} \tag{2.23}$$

by using the relation

$$\frac{1}{V}\int \mathrm{d}^3x e^{i(\boldsymbol{k}-\boldsymbol{k'})\boldsymbol{x}} = \delta_{\boldsymbol{k},\boldsymbol{k'}}. \tag{2.24}$$

After transforming our Hamiltonian into Fourier space, we diagonalise the Hamilton operator finally with a Bogoliubov transformation

$$\hat{\alpha}_{\boldsymbol{k}} = u_{\boldsymbol{k}}\hat{a}_{\boldsymbol{k}\uparrow} - v_{\boldsymbol{k}}\hat{a}^{\dagger}_{-\boldsymbol{k}\downarrow}, \quad \hat{\alpha}^{\dagger}_{\boldsymbol{k}} = u^{*}_{\boldsymbol{k}}\hat{a}^{\dagger}_{\boldsymbol{k}\uparrow} - v^{*}_{\boldsymbol{k}}\hat{a}_{-\boldsymbol{k}\downarrow}, \tag{2.25}$$

$$\hat{\beta}_{\boldsymbol{k}} = u_{\boldsymbol{k}}\hat{a}_{-\boldsymbol{k}\downarrow} + v_{\boldsymbol{k}}\hat{a}^{\dagger}_{\boldsymbol{k}\downarrow}, \quad \hat{\beta}^{\dagger}_{\boldsymbol{k}} = u^{*}_{\boldsymbol{k}}\hat{a}^{\dagger}_{-\boldsymbol{k}\downarrow} + v^{*}_{\boldsymbol{k}}\hat{a}_{\boldsymbol{k}\uparrow} \tag{2.26}$$

by postulating the fermionic commutation relations for the new operators

$$\left\{\hat{\alpha}_{\boldsymbol{k}},\ \hat{\beta}_{\boldsymbol{k'}}\right\} = \left\{\hat{\alpha}^{\dagger}_{\boldsymbol{k}}, \hat{\beta}^{\dagger}_{\boldsymbol{k'}}\right\} = 0, \tag{2.27}$$

$$\left\{\hat{\alpha}^{\dagger}_{\boldsymbol{k}},\ \hat{\beta}_{\boldsymbol{k'}}\right\} = \left\{\hat{\alpha}_{\boldsymbol{k}}, \hat{\beta}^{\dagger}_{\boldsymbol{k'}}\right\} = 0, \tag{2.28}$$

$$\left\{\hat{\alpha}_{\boldsymbol{k}}, \hat{\alpha}^{\dagger}_{\boldsymbol{k'}}\right\} = \left\{\hat{\beta}_{\boldsymbol{k}}, \hat{\beta}^{\dagger}_{\boldsymbol{k'}}\right\} = \delta_{\boldsymbol{k},\boldsymbol{k'}}. \tag{2.29}$$

From (2.29) we deduce the condition

$$|u_{\boldsymbol{k}}|^2 + |v_{\boldsymbol{k}}|^2 = 1, \tag{2.30}$$

so that the transformation is canonical. This allows to invert (2.25), (2.26) and leads to the representation of our previous operators with the new Bogoliubov operators

$$\hat{a}_{\boldsymbol{k}\uparrow} = u^{*}_{\boldsymbol{k}}\hat{\alpha}_{\boldsymbol{k}} + v_{\boldsymbol{k}}\hat{\beta}^{\dagger}_{\boldsymbol{k}}, \qquad \hat{a}^{\dagger}_{\boldsymbol{k}\uparrow} = u_{\boldsymbol{k}}\hat{\alpha}^{\dagger}_{\boldsymbol{k}} + v^{*}_{\boldsymbol{k}}\hat{\beta}_{\boldsymbol{k}}, \tag{2.31}$$

$$\hat{a}^{\dagger}_{-\boldsymbol{k}\downarrow} = -v^{*}_{\boldsymbol{k}}\hat{\alpha}_{\boldsymbol{k}} + u_{\boldsymbol{k}}\hat{\beta}^{\dagger}_{\boldsymbol{k}}, \qquad \hat{a}_{-\boldsymbol{k}\downarrow} = -v_{\boldsymbol{k}}\hat{\alpha}^{\dagger}_{\boldsymbol{k}} + u^{*}_{\boldsymbol{k}}\hat{\beta}_{\boldsymbol{k}}. \tag{2.32}$$

Plugging this relation into (2.23), we derive a sufficient condition

$$2\epsilon\left(\boldsymbol{k}\right)u^{*}_{\boldsymbol{k}}v^{*}_{\boldsymbol{k}} - \Delta^{*}u^{*2}_{\boldsymbol{k}} + \Delta v^{*2}_{\boldsymbol{k}} = 0 \tag{2.33}$$

with the free dispersion $\epsilon\left(\boldsymbol{k}\right) \equiv \frac{\hbar^2\boldsymbol{k}^2}{2M} - \mu$, in order to achieve a diagonal shape of the Hamilton operator. Because of the U(1) symmetry in (2.33), it is sufficient to proceed with the absolute values of $u_{\boldsymbol{k}}$, $v_{\boldsymbol{k}}$ and Δ. Additionally, considering the two constraints (2.30) and (2.33), the amplitudes of the Bogoliubov transformation become fixed

$$u_{\boldsymbol{k}} = \sqrt{\frac{1}{2}\left(1 + \frac{\epsilon\left(\boldsymbol{k}\right)}{\sqrt{\epsilon\left(\boldsymbol{k}\right)^2 + \Delta^2}}\right)}, \tag{2.34}$$

$$v_{\boldsymbol{k}} = \sqrt{\frac{1}{2}\left(1 - \frac{\epsilon\left(\boldsymbol{k}\right)}{\sqrt{\epsilon\left(\boldsymbol{k}\right)^2 + \Delta^2}}\right)}. \tag{2.35}$$

From this, we derive a diagonalised Hamiltonian

$$\hat{H}_{\mathrm{MF}} = \sum_{\boldsymbol{k}} E\left(\boldsymbol{k}\right)\left\{\hat{\alpha}^{\dagger}_{\boldsymbol{k}}\hat{\alpha}_{\boldsymbol{k}} + \hat{\beta}^{\dagger}_{\boldsymbol{k}}\hat{\beta}_{\boldsymbol{k}}\right\} + E_0 \tag{2.36}$$

with the Bogoliubov dispersion

$$E(\boldsymbol{k}) = \sqrt{\epsilon(\boldsymbol{k})^2 + \Delta^2} \tag{2.37}$$

and the ground-state energy

$$E_0 = V\frac{\Delta^2}{g} - \sum_{\boldsymbol{k}}\left[E(\boldsymbol{k}) - \epsilon(\boldsymbol{k})\right]. \tag{2.38}$$

2.3. Self-Consistency Equations

Now we consider the statistical properties which can be derived from the mean-field partition function, with the aim to fix the order parameter and the chemical potential. Therefore, we start with our initial second-quantised mean-field Hamiltonian (2.6) and determine the particle number as a derivative of the free energy with respect to the chemical potential

$$N = -\frac{\partial F_{\mathrm{MF}}(\Delta, \Delta^*)}{\partial \mu}, \tag{2.39}$$

since we are dealing with the grand-canonical ensemble. Accordingly, this equation is referred to as the particle-number equation. A second condition is given by the principle of minimal sensitivity (2.14), which gives rise to another relation (2.16), known as the order-parameter equation. Consequently, we need to choose chemical potential μ and gap parameter Δ to fulfil both equations (2.16) and (2.39) at the same time.

Using the dependency between mean-field free energy and mean-field partition function (2.13), we calculate the partial derivative of the partition function

$$\frac{\partial Z_{\mathrm{MF}}}{\partial \mu} = -\beta \mathrm{Tr}\left\{ \frac{\partial \hat{H}_{\mathrm{MF}}}{\partial \mu} e^{-\beta \hat{H}_{\mathrm{MF}}} \right\} = -\beta \sum_{\sigma} \int \mathrm{d}^3 x \mathrm{Tr}\left\{ \hat{\psi}^\dagger_\sigma(\boldsymbol{x}) \hat{\psi}_\sigma(\boldsymbol{x}) e^{-\beta \hat{H}_{\mathrm{MF}}} \right\} \tag{2.40}$$

and obtain for the particle-number equation (2.39)

$$N = -\frac{\partial F_{\mathrm{MF}}}{\partial \mu} = \frac{1}{\beta} \frac{1}{Z_{\mathrm{MF}}} \frac{\partial Z_{\mathrm{MF}}}{\partial \mu} = \sum_{\sigma} \int \mathrm{d}^3 x \langle \hat{\psi}^\dagger_\sigma(\boldsymbol{x}) \hat{\psi}_\sigma(\boldsymbol{x}) \rangle_{\mathrm{MF}}. \tag{2.41}$$

Hence, the particle-number density is given by the pair-correlation function

$$n(\boldsymbol{x}) = \sum_{\sigma} \langle \hat{\psi}^\dagger_\sigma(\boldsymbol{x}) \hat{\psi}_\sigma(\boldsymbol{x}) \rangle_{\mathrm{MF}}. \tag{2.42}$$

Finally, the self-consistency equations are both represented in terms of pair-correlation functions. Since we have two equations (2.16) and (2.41) for two unknown quantities, this problem is well posed.

We can evaluate the pair-correlation functions (2.16) and (2.42) in the case of the fermionic Bogoliubov operators (2.25), (2.26). To calculate the mean-field expectation value of the pair-correlation functions, we have to introduce the trace for the Bogoliubov operators

$$\mathrm{Tr}\{\bullet\} = \prod_{\boldsymbol{k}_\alpha, \boldsymbol{k}_\beta} \sum_{n_{\boldsymbol{k}_\alpha}=0}^{1} \sum_{n_{\boldsymbol{k}_\beta}=0}^{1} \left(\prod_{\boldsymbol{k}_\alpha, \boldsymbol{k}_\beta} {}_{\boldsymbol{k}_\alpha, \boldsymbol{k}_\beta}\langle n_{\boldsymbol{k}_\alpha}, n_{\boldsymbol{k}_\beta}| \right) \bullet \left(\prod_{\boldsymbol{k}_\alpha, \boldsymbol{k}_\beta} |n_{\boldsymbol{k}_\alpha}, n_{\boldsymbol{k}_\beta}\rangle_{\boldsymbol{k}_\alpha, \boldsymbol{k}_\beta} \right). \tag{2.43}$$

In this definition $\hat{n}_{\boldsymbol{k}_\alpha} = \hat{\alpha}^\dagger_{\boldsymbol{k}} \hat{\alpha}_{\boldsymbol{k}}$ and $\hat{n}_{\boldsymbol{k}_\beta} = \hat{\beta}^\dagger_{\boldsymbol{k}} \hat{\beta}_{\boldsymbol{k}}$ denote the quasi-particle number operator of an individual state $\boldsymbol{k}_\alpha, \boldsymbol{k}_\beta$. The particle number for an individual state $n_{\boldsymbol{k}_\alpha}$, $n_{\boldsymbol{k}_\beta}$ can be either zero or one due to the Pauli principle for fermionic operators.
Additionally, we use the diagonalised mean-field Hamilton operator (2.36) to get the corresponding mean-field partition function

$$Z_{\mathrm{MF}} = e^{-\beta E_0} \mathrm{Tr}\left\{ e^{-\beta \sum_{\boldsymbol{k}} E(\boldsymbol{k}) (\hat{\alpha}^\dagger_{\boldsymbol{k}} \hat{\alpha}_{\boldsymbol{k}} + \hat{\beta}^\dagger_{\boldsymbol{k}} \hat{\beta}_{\boldsymbol{k}})} \right\} = e^{-\beta E_0} \prod_{\boldsymbol{k}} \left[1 + e^{-\beta E(\boldsymbol{k})} \right]^2. \tag{2.44}$$

Consequently, any mean-field expectation value can be evaluated in a similar way. Thus, we derive an expression for the order parameter (2.16) in terms of the amplitudes $u_{\boldsymbol{k}}$, $v_{\boldsymbol{k}}$ of the Bogoliubov transformation

$$\frac{\Delta}{g} = \sum_{\boldsymbol{k}} \left\{ \frac{u_{\boldsymbol{k}} v_{\boldsymbol{k}}^* \left(e^{-\beta \epsilon_{\boldsymbol{k}}} - 1 \right)}{1 + e^{-\beta \epsilon_{\boldsymbol{k}}}} \right\}. \tag{2.45}$$

and analogously for the particle-number density (2.42)

$$n = 2 \sum_{\boldsymbol{k}} \left\{ \frac{|v_{\boldsymbol{k}}|^2 + |u_{\boldsymbol{k}}|^2 e^{-\beta \epsilon_{\boldsymbol{k}}}}{1 + e^{-\beta \epsilon_{\boldsymbol{k}}}} \right\}. \tag{2.46}$$

Finally, we plug in the Bogoliubov amplitudes (2.34), as well as (2.35), and derive for the order-parameter equation

$$0 = \Delta \left[\frac{2}{g} + \frac{1}{V} \sum_{\boldsymbol{k}} \frac{\tanh\left(\frac{\beta}{2} E(\boldsymbol{k}) \right)}{E(\boldsymbol{k})} \right] \tag{2.47}$$

and analogously for the particle-number equation

$$n = \frac{1}{V} \sum_{\boldsymbol{k}} \left\{ 1 - \frac{\epsilon(\boldsymbol{k})}{E(\boldsymbol{k})} \tanh\left(\frac{\beta}{2} E(\boldsymbol{k}) \right) \right\}. \tag{2.48}$$

In the following, these two equations have to be calculated simultaneously to determine both the chemical potential and the order parameter.

3. Homogeneous Fermi Gas

The self-consistency equations (2.47) and (2.48), which we introduced in the previous chapter, determine the order parameter Δ and chemical potential μ, respectively. In the present chapter we solve these self-consistency equations for a homogeneous Fermi gas. In the following, we calculate at first the solution analytically for the special case $T \to 0$ and present then a detailed numerical solution at finite temperature.

3.1. Renormalisation of Contact Interaction

Since we are taking into account a large number of particles in an infinite volume, which is implied by the homogeneous Fermi gas, the simultaneous limits $N \to \infty$ and $V \to \infty$ are justified. Consequently, we are working in the thermodynamic limit, where the particle-number density is supposed to be finite

$$n = \frac{N}{V} < \infty. \tag{3.1}$$

Thus, the $\boldsymbol{k}$ summation is approximated by an integration [49] according to

$$\frac{1}{V}\sum_{\boldsymbol{k}} \to \int \frac{\mathrm{d}^3 k}{(2\pi)^3} \tag{3.2}$$

and the self-consistency equations (2.47) and (2.48) reduce in the non-vanishing case of the order parameter for the order parameter itself to

$$-\frac{2}{g} = \int \frac{\mathrm{d}^3 k}{(2\pi)^3} \frac{\tanh\left[\frac{\beta}{2} E\left(\boldsymbol{k}\right)\right]}{E\left(\boldsymbol{k}\right)} \tag{3.3}$$

and analogously for the chemical potential to

$$n = \int \frac{\mathrm{d}^3 k}{(2\pi)^3} \left\{1 - \frac{\epsilon\left(\boldsymbol{k}\right)}{E\left(\boldsymbol{k}\right)} \tanh\left[\frac{\beta}{2} E\left(\boldsymbol{k}\right)\right]\right\}. \tag{3.4}$$

Investigating the equation for the order parameter (3.3), we detect an UV-divergence. In order to treat this problem, the contact interaction with its bare interaction strength g needs to be renormalised. Considering scattering theory in the context of many-body physics, the renormalisation is given by [50, 51]

$$\frac{1}{g} = \frac{M}{4\pi\hbar^2 a_\mathrm{s}} - \int \frac{\mathrm{d}^3 k}{(2\pi)^3} \frac{M}{\hbar^2 \boldsymbol{k}^2}, \tag{3.5}$$

where a_s denotes the s-wave scattering length. Inserting (3.5) in (3.3), we obtain the renormalised gap equation

$$\frac{M}{2\pi\hbar^2 a_\mathrm{s}} = \int \frac{\mathrm{d}^3 k}{(2\pi)^3} \left\{\frac{2M}{\hbar^2 \boldsymbol{k}^2} - \frac{\tanh\left[\frac{\beta}{2} E\left(\boldsymbol{k}\right)\right]}{E\left(\boldsymbol{k}\right)}\right\}. \tag{3.6}$$

The substitution $\varepsilon = \hbar^2 \boldsymbol{k}^2/2M$ uses the symmetry of the integrand in order-parameter and particle-number equation, that allows us to treat the three-dimensional integral as a scalar energy integral for both self-consistency equations. The equation for the particle number becomes

$$n = \frac{2}{\sqrt{\pi}} \left(\frac{M}{2\pi\hbar^2}\right)^{\frac{3}{2}} \int_0^\infty \mathrm{d}\varepsilon \sqrt{\varepsilon} \left\{ 1 - \frac{\varepsilon - \mu}{\sqrt{(\varepsilon-\mu)^2 + \Delta^2}} \tanh\left(\frac{\beta}{2}\sqrt{(\varepsilon-\mu)^2+\Delta^2}\right)\right\} \tag{3.7}$$

and analogously in the case of the order parameter

$$\frac{M}{2\pi\hbar^2 a_\mathrm{s}} = \frac{2}{\sqrt{\pi}} \left(\frac{M}{2\pi\hbar^2}\right)^{\frac{3}{2}} \int_0^\infty \mathrm{d}\varepsilon \sqrt{\varepsilon} \left\{ \frac{1}{\varepsilon} - \frac{\tanh\left(\frac{\beta}{2}\sqrt{(\varepsilon-\mu)^2+\Delta^2}\right)}{\sqrt{(\varepsilon-\mu)^2+\Delta^2}}\right\}. \tag{3.8}$$

In the next section, we will evaluate both equations for the zero-temperature case analytically with appropriate approximations and moreover numerically.

3.2. Low-Temperature Limit

Analysing both self-consistency equations (3.7) and (3.8), we see that the temperature dependence occurs in the tanh-function and is contained in $\beta = 1/k_\mathrm{B}T$. The tanh-function can be represented by the exponential function

$$\tanh x = 1 - \frac{2}{e^{2x}+1}. \tag{3.9}$$

Thus, we can split the temperature-dependent part of the self-consistency equations from the temperature independent one. Accordingly, considering the low-temperature regime $T \to 0$ follows

$$\lim_{T\to 0} \tanh\left(\frac{\beta}{2}\sqrt{(\varepsilon-\mu)^2+\Delta^2}\right) = 1, \tag{3.10}$$

since the second term of (3.9) containing the exponential function vanishes.
Consequently, we plug in this relation into both self-consistency equations (3.7) and (3.8) to derive the zero-temperature limit. To simplify the numerical and analytical evaluation of the integrals, we introduce dimensionless quantities and scale our energies in units of the Fermi energy

$$\tilde{\varepsilon} = \frac{\varepsilon}{E_\mathrm{F}}, \quad \tilde{\Delta} = \frac{\Delta}{E_\mathrm{F}}, \quad \tilde{\mu} = \frac{\mu}{E_\mathrm{F}}. \tag{3.11}$$

Therefore the equation for the order parameter simplifies to the dimensionless form

$$\frac{1}{a_\mathrm{s} k_\mathrm{F}} = \frac{2}{\pi} \int_0^\infty \mathrm{d}\tilde{\varepsilon} \sqrt{\tilde{\varepsilon}} \left[\frac{1}{\tilde{\varepsilon}} - \frac{1}{\sqrt{(\tilde{\varepsilon}-\tilde{\mu})^2+\tilde{\Delta}^2}}\right], \tag{3.12}$$

likewise the equation for the particle-number

$$\frac{4}{3} = \int_0^\infty \mathrm{d}\tilde{\varepsilon} \sqrt{\tilde{\varepsilon}} \left[1 - \frac{\tilde{\varepsilon}-\tilde{\mu}}{\sqrt{(\tilde{\varepsilon}-\tilde{\mu})^2+\tilde{\Delta}^2}}\right]. \tag{3.13}$$

Since we are interested in an approximative analytical evaluation of the self-consistency equations in this limiting case, we perform several transformations in the following.

3.2.1. Transformations

The approach is based on the procedure in [52]. First of all, introducing the substitution

$$\tilde{\varepsilon} = x\sqrt{\tilde{\mu}^2 + \tilde{\Delta}^2} \tag{3.14}$$

follows for the order-parameter equation

$$\frac{1}{a_\mathrm{s}k_\mathrm{F}} = \frac{2}{\pi}\sqrt[4]{\tilde{\mu}^2 + \tilde{\Delta}^2}\int_0^\infty \mathrm{d}x \frac{1}{\sqrt{x}}\left[1 - \frac{x}{\sqrt{x^2 - 2xt + 1}}\right] \tag{3.15}$$

and for the particle-number equation

$$\frac{4}{3} = \sqrt[4]{\tilde{\Delta}^2 + \tilde{\mu}^2}^3 \int_0^\infty \mathrm{d}x\sqrt{x}\left[1 - \frac{x - t}{\sqrt{x^2 - 2xt + 1}}\right]. \tag{3.16}$$

Here we have introduced as an abbreviation the parameter

$$t = \frac{\tilde{\mu}}{\sqrt{\tilde{\mu}^2 + \tilde{\Delta}^2}}, \tag{3.17}$$

which fulfils the condition $|t| < 1$. In the following, it is necessary to establish a dependence between the parameter t and the s-wave scattering length a_s, which fixes the parameter for a given scattering length. Order parameter Δ and chemical potential μ will then both be represented as functions depending on this parameter t. Consequently, we are able to determine the order parameter Δ and the chemical potential μ for a given s-wave scattering length a_s.
In order to achieve this goal, we introduce the second substitution

$$x = \frac{1 - u^2}{2(t - u)}, \tag{3.18}$$

which follows for the equation of the order parameter

$$\frac{1}{a_\mathrm{s}k_\mathrm{F}} = \frac{\sqrt{2}}{\pi}\sqrt[4]{\tilde{\mu}^2 + \tilde{\Delta}^2}\int_1^\infty \mathrm{d}u \frac{1 - ut}{\sqrt{u^2 - 1}\sqrt{u - t}^3} \tag{3.19}$$

and similarly for the particle-number equation

$$\frac{4}{3} = \frac{1 - t^2}{\sqrt{2}}\sqrt[4]{\tilde{\mu}^2 + \tilde{\Delta}^2}^3 \int_1^\infty \mathrm{d}u \frac{\sqrt{u^2 - 1}}{\sqrt{u - t}^5}. \tag{3.20}$$

Performing subsequent a third substitution

$$v = \sqrt{u - 1} \tag{3.21}$$

yields the transformed order-parameter equation

$$\frac{1}{a_\mathrm{s}k_\mathrm{F}} = \frac{\sqrt{2}^3}{\pi}\sqrt[4]{\tilde{\mu}^2 + \tilde{\Delta}^2}\int_0^\infty \mathrm{d}v \frac{1}{\sqrt{v^2 + 1}}\left[\frac{1 - t^2}{\sqrt{v^2 + 1 - t}^3} - \frac{t}{\sqrt{v^2 + 1 - t}}\right], \tag{3.22}$$

as well as the particle-number equation

$$\frac{\sqrt{8}}{3} = \sqrt[4]{\tilde{\mu}^2 + \tilde{\Delta}^2}^3 \int_0^\infty \mathrm{d}v \frac{1 - t^2}{\sqrt{v^2 + 2}}\left[\frac{1}{\sqrt{v^2 + 1 - t}} - \frac{1 - t^2}{\sqrt{v^2 + 1 - t}^5} + \frac{2t}{\sqrt{v^2 + 1 - t}^3}\right]. \tag{3.23}$$

Finally, the fourth and last substitution

$$z = \frac{v^2}{v^2 + 1 - t} \tag{3.24}$$

yields for the equation of the order parameter

$$\frac{1}{a_\mathrm{s} k_\mathrm{F}} = \frac{2}{\pi} \sqrt[4]{\tilde{\mu}^2 + \tilde{\Delta}^2} \left[2\mathrm{E}\left(\sqrt{\frac{1+t}{2}} \right) - \mathrm{K}\left(\sqrt{\frac{1+t}{2}} \right) \right] \tag{3.25}$$

as well as for the particle-number equation

$$\frac{1}{\sqrt[4]{\tilde{\mu}^2 + \tilde{\Delta}^2}^3} = t\mathrm{E}\left(\sqrt{\frac{1+t}{2}} \right) + \frac{1-t}{2}\mathrm{K}\left(\sqrt{\frac{1+t}{2}} \right). \tag{3.26}$$

Here we substituted the elliptic integrals of first- and second-kind, which are introduced in detail in the appendix B.1.

3.2.2. General Theory with Elliptic Functions

Taking into account the representation of both self-consistency equations with elliptic integrals, we can combine the equation for the order-parameter (3.25) with the particle-number equation (3.26) and derive in this way the desired relation between the parameter t and the scattering length a_s

$$\frac{1}{a_\mathrm{s} k_\mathrm{F}} = \frac{2}{\pi} \frac{2\mathrm{E}\left(\sqrt{\frac{1+t}{2}} \right) - \mathrm{K}\left(\sqrt{\frac{1+t}{2}} \right)}{\left[t\mathrm{E}\left(\sqrt{\frac{1+t}{2}} \right) + \frac{1-t}{2}\mathrm{K}\left(\sqrt{\frac{1+t}{2}} \right) \right]^{\frac{1}{3}}}. \tag{3.27}$$

In the following, this relation is used to calculate numerically t for a given scattering length a_s. In the next step, we represent the chemical potential and the order parameter as function of t. Using the initial definition of the parameter t in (3.17) and the particle-number equation (3.26), we derive the desired relation for the chemical potential

$$\tilde{\mu}(t) = \frac{t}{\left[t\mathrm{E}\left(\sqrt{\frac{1+t}{2}} \right) + \frac{1-t}{2}\mathrm{K}\left(\sqrt{\frac{1+t}{2}} \right) \right]^{\frac{2}{3}}} \tag{3.28}$$

and also for the order parameter

$$\tilde{\Delta}(t) = \frac{\sqrt{1-t^2}}{\left[t\mathrm{E}\left(\sqrt{\frac{1+t}{2}} \right) + \frac{1-t}{2}\mathrm{K}\left(\sqrt{\frac{1+t}{2}} \right) \right]^{\frac{2}{3}}}. \tag{3.29}$$

Since the parameter t is fixed by the s-wave scattering length a_s due to (3.27), we are able to calculate chemical potential and order parameter as functions of the s-wave scattering length based on (3.28) and (3.29). This allows us to analyse the behaviour of these two quantities within the BCS regime of the crossover, which is characterised by $1/a_\mathrm{s} k_\mathrm{F} < 0$. Although the analytic representation by elliptic functions seems to be quite elegant at first glance, there is still the problem that these functions can only be evaluated numerically. Motivated by the limiting case $\Delta \to 0$, which is present especially in the deep BCS limit $1/a_\mathrm{s} k_\mathrm{F} < -1$, we can introduce a perturbation theory for small interactions.

3.2.3. Perturbation Theory for Small Interactions

Since we are looking for an analytic expression of order parameter and chemical potential depending on the scattering length a_s to highlight fundamental relations, we evaluate the equations, which we derived in the previous subsection, in terms of perturbation theory.

In the limit of small interactions, we have $\Delta \to 0$ which implies $t \to 1$ due to (3.17). In order to perturbatively evaluate the elliptic integrals, the introduction of the new parameter

$$\tau = 1 - t \tag{3.30}$$

leads to expansions for both the first- and the second-kind elliptic integrals, respectively,

$$\mathrm{E}\left(\sqrt{\frac{\tau}{2}}\right) = 1 + \frac{1}{8}\left(\ln 2 - \ln \tau - 1\right)\tau + \mathcal{O}(\tau^2), \tag{3.31}$$

$$\mathrm{K}\left(\sqrt{\frac{\tau}{2}}\right) = \frac{5}{2}\ln 2 - \frac{1}{2}\ln \tau + \frac{1}{16}\left(5\ln 2 - 2 - \ln \tau\right)\tau + \mathcal{O}(\tau^2), \tag{3.32}$$

as follows from the summation formulas shown in the appendix (B.7) and (B.8). These expansions are used to introduce a perturbative representation of the inverse s-wave scattering length (3.27) in powers of τ

$$\frac{1}{a_s k_F} \equiv f(\tau) = f_0(\tau) + \tau f_1(\tau) + \mathcal{O}(\tau^2), \tag{3.33}$$

where the zeroth-order term reads

$$f_0 = 2 - \frac{5}{2}\ln 2 + \frac{1}{2}\ln \tau \tag{3.34}$$

and the first-order term is given by

$$f_1 = \frac{1}{16}\left[3 + 5\ln 2\left(5\ln 2 - 4\right) + \ln \tau\left(4 - 10\ln 2 + \ln \tau\right)\right]. \tag{3.35}$$

This expansion yields a perturbative result for the parameter τ, which is plugged into the equation for the chemical potential (3.28) as well as for the order parameter (3.29) leading to a perturbative result after an additional expansion. For this purpose, we use (3.17) in order to write the order parameter in terms of the new parameter τ

$$\tilde{\Delta}(\tau) = \tilde{\mu}(\tau)\sqrt{2\tau}\frac{\sqrt{1 - \frac{\tau}{2}}}{1 - \tau} \tag{3.36}$$

and the chemical potential follows similarly from (3.28)

$$\tilde{\mu}(\tau) = \frac{1 - \tau}{\left[(1-\tau)E\left(\sqrt{\frac{\tau}{2}}\right) + \frac{\tau}{2}K\left(\sqrt{\frac{\tau}{2}}\right)\right]^{\frac{2}{3}}}. \tag{3.37}$$

First, we start with calculating the zeroth-order result for τ, which follows from (3.33) and (3.34)

$$\tau_0 = \frac{32}{e^4}\exp\left(\frac{\pi}{2a_s k_F}\right). \tag{3.38}$$

Expanding the chemical potential (3.37) yields

$$\tilde{\mu}_0 \equiv \tilde{\mu}(\tau_0) = 1 \tag{3.39}$$

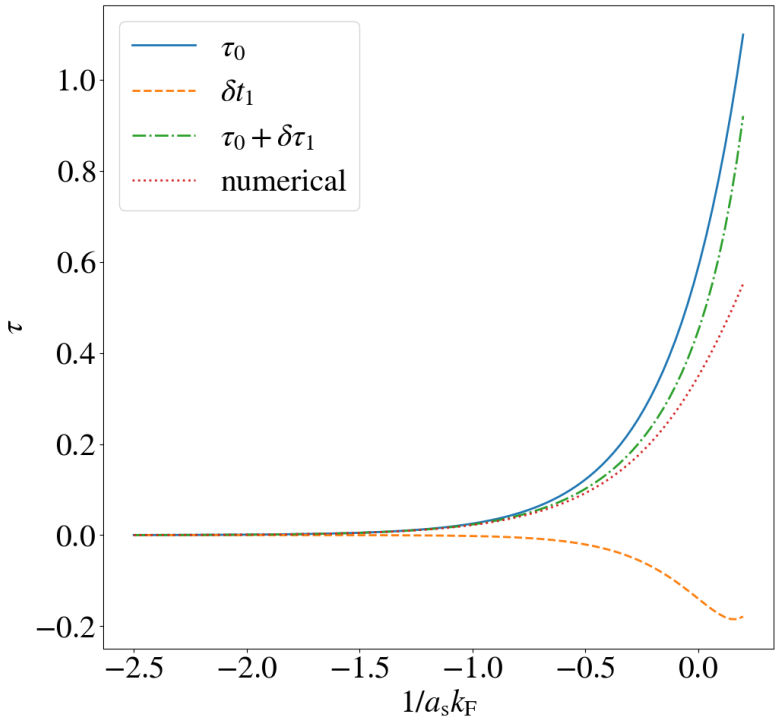

Figure 3.1.: Dependence of the parameter τ from $1/a_s k_F$. The perturbative results τ_0 in (3.38) and $\delta\tau_1$ in (3.42) are represented along with the numerical evaluation following from (3.27).

and for the order parameter (3.36) we obtain

$$\tilde{\Delta}_0 \equiv \tilde{\Delta}(\tau_0) = \frac{8}{e^2} \exp\left(\frac{\pi}{2 a_s k_F}\right). \tag{3.40}$$

The zeroth-order formula for the order parameter (3.40) was already derived in Ref. [53]. A first rough estimate about the quality of our perturbative result can be deduced from the fact that in standard BCS-theory for zero temperature [10], the chemical potential coincides with the Fermi energy, which is equivalent to the above result (3.39). To achieve an even better agreement with the full numerical evaluation, we can expand our perturbation theory up to first order. We now prepare the respective results from zeroth- and first-order perturbation theory graphically and compare them with the numerical evaluation.

For the first-order result, we start from our zeroth-order result of the parameter τ and consider a small correction $\delta\tau_1$. As the ln-function often appears in connection with the parameter τ, compare with (3.33)–(3.35), it is appropriate to introduce the Taylor series assuming $\delta\tau_1 \to 0$

$$\ln(\tau_0 + \delta\tau_1) = \ln\tau_0 + \frac{\delta\tau_1}{\tau_0} + \mathcal{O}\left[(\delta\tau)^2\right]. \tag{3.41}$$

With this, we derive from expanding (3.33)–(3.35) up to first order the previously motivated first-order correction

$$\delta\tau_1 = \frac{\frac{\pi}{2 a_s k_F} - 2 + \frac{5}{2}\ln 2 - \frac{1}{2}\ln\tau_0 - \frac{1}{16}\left[3 + \ln 2\,(\ln\tau_0 - 16 - 5\ln 2)\right]\tau_0}{\frac{1}{2\tau_0} + \frac{1}{16}\left[7 + 5\ln 2\,(5\ln 2 - 6 - 2\ln\tau_0) + \ln\tau_0\,(\ln\tau_0 + 6)\right]}. \tag{3.42}$$

Again we can plug in this correction into the chemical potential (3.37) and expand up to first order

$$\begin{aligned}\tilde{\mu}(\tau) =& 1 + \frac{1}{6}\left[\ln\tau_0 - 5\ln 2 - 2\right]\tau_0 \\ &+ \frac{1}{6}\left(\ln\tau_0 - 1 - 5\ln 2\right)\delta\tau_1 + \mathcal{O}\left[(\delta\tau_1)^2\right]\end{aligned} \tag{3.43}$$

and analogously for the order parameter (3.36)

$$\begin{aligned}\tilde{\Delta}(\tau) =& \sqrt{2\tau_0}\left[1 + \frac{\tau_0}{6}\left(\ln\tau_0 - 2 - 5\ln 2\right]\right)\left(1 + \frac{3}{4}\tau_0\right) \\ &+ \left\{2 + \frac{\tau_0}{6}\left(\ln\tau_0 - 2 - 5\ln 2\right)\left(\sqrt{2\tau_0} + \frac{1 + \frac{3}{4}\tau_0}{\sqrt{2\tau_0}}\right) + \frac{\sqrt{2\tau_0}}{6}\left(\ln\tau_0 - 1 - 5\ln 2\right)\left(1 + \frac{3}{4}\tau_0\right)\right\}\delta\tau_1.\end{aligned} \tag{3.44}$$

To determine the quality of the perturbation theory in zeroth- and first-order, we compare the results with the numerical evaluation. Therefore the parameter t is calculated numerically from (3.27) and is then plugged into the expression for chemical potential (3.28) and order parameter (3.29). Thereby, the occurring elliptic functions are also evaluated numerically.

Considering the evaluation of the parameter t in Figure 3.1, we see in the BCS-regime for $1/a_s k_F < -1$ that the perturbative solutions agree well with the exact numerical evaluation. Passing to the unitary regime, the perturbative solutions start to deviate from the numerical result. However, we see that the first order agrees better with the numerical result. Here, the deviation becomes obvious for the regime $1/a_s k_F < -0.5$. In the unitary regime, the perturbative results overestimate the exact numerical result. Hence, we expect a similar behaviour for the chemical potential and the order parameter.

In Figure 3.2, we see that a larger attractive interaction reduces the chemical potential. The zeroth-order perturbative result for the chemical potential agrees with the numerical evaluation only in the deep BCS regime for $1/a_s k_F < -2$. The first-order achieves a higher agreement up to $1/a_s k_F < -0.5$.

The order parameter is increased by a larger attractive interaction, as we see in Figure 3.3. The quality of the approximation behaves similar, the zeroth-order result shows agreement up to $1/a_s k_F < -1.5$, then it starts to overestimate the order parameter. Unfortunately, in this case the first-order result agrees not much better, it leads to an improvement up to $1/a_s k_F < -0.5$, but then it fails completely. In summary, considering our perturbative results, we have seen that the zeroth-order leads to an appropriate approximation in the deep BCS-regime, whereas the first-order allows us to treat the quantities up to $1/a_s k_F < -0.5$ perturbatively.

To get further insights of the physical meaning of the order parameter, we take into account the condensate fraction

$$n_0 = \frac{M^{\frac{3}{2}}}{8\pi\hbar^3}\Delta^{\frac{3}{2}}\sqrt{\frac{\mu}{\Delta} + \sqrt{1 + \frac{\mu^2}{\Delta^2}}}, \tag{3.45}$$

which has been calculated for the zero-temperature limit by Salasnich et al. in Ref. [54]. An increasing of the order parameter caused by stronger interactions leads to a higher condensate fraction, as it is depicted in Figure 3.4.

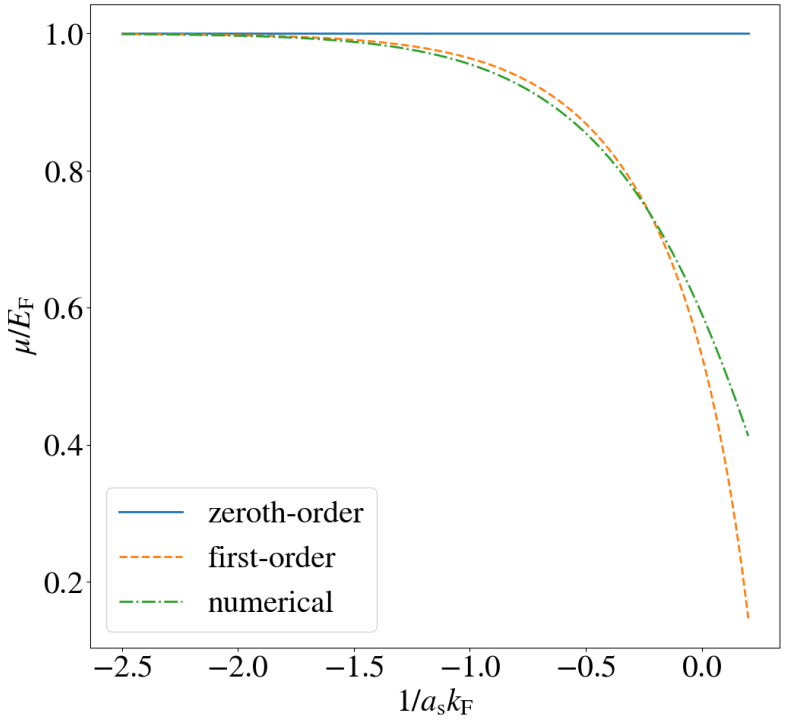

Figure 3.2.: Chemical potential in the zero-temperature limit as function of $1/a_s k_F$. We figured out the zeroth-order (3.39), the first-order (3.43) as well as the numerical result (3.28) where the parameter t follows from (3.27).

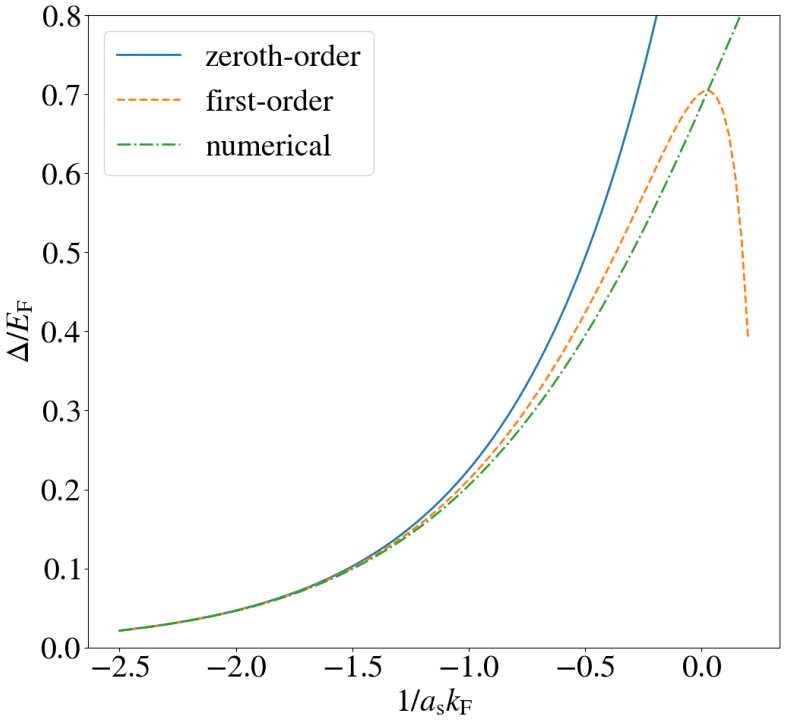

Figure 3.3.: Order parameter in the zero-temperature limit as function of $1/a_s k_F$. Again we show zeroth-order (3.40), first-order (3.44) and numerical evaluation (3.29) where t is fixed by (3.27).

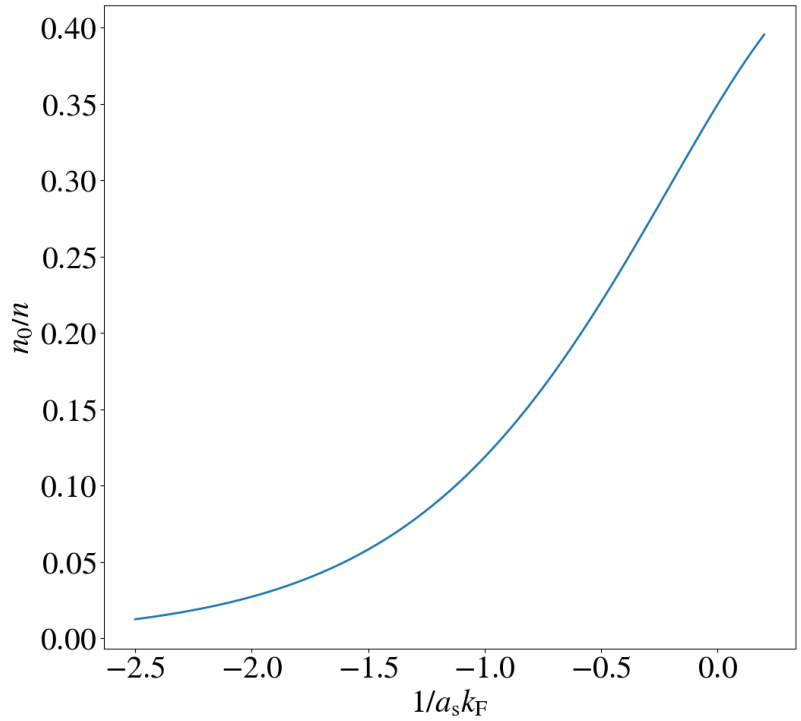

Figure 3.4.: Condensate fraction from (3.45) as function of $1/a_s k_F$. Similar to the behaviour of the order parameter, which is depicted in Figure 3.3, stronger interactions lead to a higher condensate fraction.

3.3. Temperature Dependence

After we have dealt in depth with the zero-temperatures limit, we focus now on the temperature dependent behaviour. Especially, we deal with the impact of the temperature in combination with the s-wave scattering length upon both the order parameter and the chemical potential. Again, we introduce dimensionless quantities in units of the Fermi energy (3.11) and extend them by the inverse thermal energy

$$\tilde{\beta} = \beta E_F, \tag{3.46}$$

which we also consider in units of the Fermi energy. Consequently, we derive for the particle-number equation (3.7)

$$\frac{4}{3} = \int_0^\infty \mathrm{d}\tilde{\varepsilon}\sqrt{\tilde{\varepsilon}}\left[1 - \frac{\tilde{\varepsilon}-\tilde{\mu}}{\sqrt{(\tilde{\epsilon}-\tilde{\mu})^2+\tilde{\Delta}^2}}\tanh\left(\sqrt{(\tilde{\varepsilon}-\tilde{\mu})^2+\tilde{\Delta}^2}\frac{\tilde{\beta}}{2}\right)\right] \tag{3.47}$$

as well as the order-parameter equation (3.8)

$$\frac{\pi}{a_s k_F} = \int_0^\infty \mathrm{d}\tilde{\varepsilon}\sqrt{\tilde{\varepsilon}}\left[\frac{1}{\tilde{\varepsilon}} - \frac{\tanh\left(\sqrt{(\tilde{\varepsilon}-\tilde{\mu})^2+\tilde{\Delta}^2}\frac{\tilde{\beta}}{2}\right)}{\sqrt{(\tilde{\varepsilon}-\tilde{\mu})^2+\tilde{\Delta}^2}}\right]. \tag{3.48}$$

Analysing both expression, we detect a divergent term for $\varepsilon \to \infty$ in the particle-number equation, as well as a divergent term for $\varepsilon \to 0$, which make a numerical treatment unfeasible at first glance. However, performing a partial integration allows us to get rid

of the divergences in both cases. This leads to the completely convergent form of the particle-number equation

$$2 = \int_0^\infty \mathrm{d}\varepsilon \sqrt{\frac{\tilde{\varepsilon}}{(\tilde{\epsilon}-\tilde{\mu})^2+\tilde{\Delta}^2}}^3 \left\{ \tilde{\Delta}^2 \tanh\left(\sqrt{(\tilde{\varepsilon}-\tilde{\mu})^2+\tilde{\Delta}^2}\frac{\tilde{\beta}}{2}\right) + \frac{\tilde{\beta}}{2}\frac{(\tilde{\epsilon}-\tilde{\mu})^2\sqrt{(\tilde{\epsilon}-\tilde{\mu})^2+\tilde{\Delta}^2}}{\cosh^2\left(\sqrt{(\tilde{\varepsilon}-\tilde{\mu})^2+\tilde{\Delta}^2}\frac{\tilde{\beta}}{2}\right)} \right\} \tag{3.49}$$

and likewise for the order-parameter equation

$$\frac{\pi}{2a_\mathrm{s}k_\mathrm{F}} = \int_0^\infty \mathrm{d}\tilde{\varepsilon}\frac{\sqrt{\tilde{\epsilon}}}{\sqrt{(\tilde{\epsilon}-\tilde{\mu})^2+\tilde{\Delta}^2}^3} \left\{ \left(\tilde{\mu}^2+\tilde{\Delta}^2-\tilde{\mu}\tilde{\varepsilon}\right)\tanh\left(\sqrt{(\tilde{\varepsilon}-\tilde{\mu})^2+\tilde{\Delta}^2}\frac{\tilde{\beta}}{2}\right) + \frac{\tilde{\beta}}{2}\frac{\tilde{\varepsilon}\,(\tilde{\varepsilon}-\tilde{\mu})\sqrt{(\tilde{\varepsilon}-\tilde{\mu})^2+\tilde{\Delta}^2}}{\cosh^2\left(\sqrt{(\tilde{\varepsilon}-\tilde{\mu})^2+\tilde{\Delta}^2}\frac{\tilde{\beta}}{2}\right)} \right\}. \tag{3.50}$$

Despite the introduction of dimensionless quantities, the fundamental problem remains unchanged: Order parameter Δ and chemical potential μ have to be chosen self-consistently to fulfil both equations at the same time. As we already did in the zero-temperature case, the idea is to perform an appropriate substitution, which deletes one quantity in one of the two-self consistency equations. Analogously to our procedure in the zero-temperature case, we want to eliminate the chemical potential in the order-parameter equation. For this purpose, we introduce an additional substitution

$$\xi = \frac{\tilde{\varepsilon}}{|\tilde{\mu}|}, \quad \zeta = \frac{\tilde{\Delta}}{|\tilde{\mu}|}, \quad b = \tilde{\beta}|\tilde{\mu}|. \tag{3.51}$$

As a result, we extract the $\mu-$dependency from both integrals. Depending on the sign of the chemical potential, we determine the sign within the integral. This is not associated with any major restrictions, since we have always a positive sign in the relevant BCS limit. Thus, we derive for the particle-number equation

$$\sqrt{\tilde{\mu}} = \left[\frac{1}{2}\int_0^\infty \mathrm{d}\xi \sqrt{\frac{\xi}{(\xi\mp 1)^2+\zeta^2}}^3 \left\{ \zeta^2 \tanh\left(\sqrt{(\xi\mp 1)^2+\zeta^2}\frac{b}{2}\right) + \frac{b}{2}\frac{(\xi-1)^2\sqrt{(\xi\mp 1)^2+\zeta^2}}{\cosh^2\left(\sqrt{(\xi\mp 1)^2+\zeta^2}\frac{b}{2}\right)} \right\}\right]^{-\frac{1}{3}} \tag{3.52}$$

and analogously for the order-parameter equation

$$\frac{\pi}{2a_\mathrm{s}k_\mathrm{F}} = \sqrt{|\tilde{\mu}|}\int_0^\infty \mathrm{d}\xi \frac{\sqrt{\xi}}{\sqrt{(\xi-1)^2+\zeta^2}^3} \left[\left(1+\zeta^2\mp\xi\right)\tanh\left(\sqrt{(\xi\mp 1)^2+\zeta^2}\frac{b}{2}\right) + \frac{b}{2}\frac{\xi(\xi\mp 1)\sqrt{(\xi\mp 1)^2+\zeta^2}}{\cosh^2\left(\sqrt{(\xi\mp 1)^2+\zeta^2}\frac{b}{2}\right)} \right]. \tag{3.53}$$

At this point, the advantage of the previous substitution becomes obvious:
We can plug in the chemical potential from the particle number equation (3.52) into the

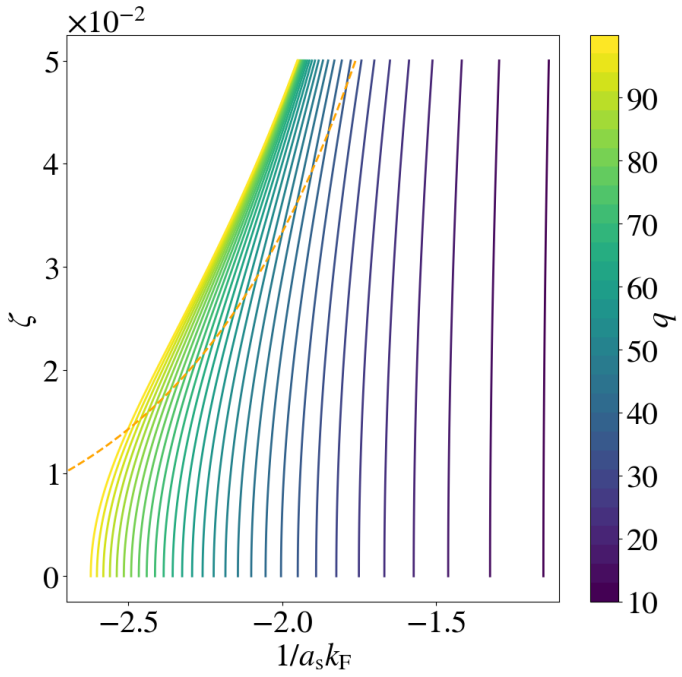

Figure 3.5.: Plot of order parameter ζ as function of dimensionless s-wave scattering length $1/a_s k_F$ for various b from (3.54), which contains the particle-number equation (3.52), represented in dimensionless quantities (3.51). The orange dotted line shows the perturbative behaviour according to to (3.40) in the zero-temperature limit.

equation for the order parameter (3.53)

$$\begin{aligned}\frac{\pi}{2a_s k_F} = \Bigg[\frac{1}{2}\int_0^\infty \mathrm{d}\xi \sqrt{\frac{\xi}{(\xi\mp 1)^2+\zeta^2}}^3 \Bigg\{\zeta^2 \tanh\left(\sqrt{(\xi\mp 1)^2+\zeta^2}\frac{b}{2}\right) \\ + \frac{b}{2}\frac{(\xi-1)^2\sqrt{(\xi\mp 1)^2+\zeta^2}}{\cosh^2\left(\sqrt{(\xi\mp 1)^2+\zeta^2}\frac{b}{2}\right)}\Bigg\}\Bigg]^{-\frac{1}{3}} \\ \cdot \int_0^\infty \mathrm{d}\xi \frac{\sqrt{\xi}}{\sqrt{(\xi-1)^2+\zeta^2}^3}\Bigg[\left(1+\zeta^2\mp\xi\right)\tanh\left(\sqrt{(\xi\mp 1)^2+\zeta^2}\frac{b}{2}\right) \\ + \frac{b}{2}\frac{\xi(\xi\mp 1)\sqrt{(\xi\mp 1)^2+\zeta^2}}{\cosh^2\left(\sqrt{(\xi\mp 1)^2+\zeta^2}\frac{b}{2}\right)}\Bigg].\end{aligned} \tag{3.54}$$

This allows us for a given b to calculate the corresponding ζ, as it is depicted in Figure 3.5. From the relation between b and the inverse thermal energy β (3.51), we are able to calculate the corresponding temperature T, since the particle-number equation (3.52) provides the chemical potential. As a result we obtain the temperature dependence of the order parameter in Figure 3.6, where we see that the order parameter decreases for larger temperatures and vanishes at the critical temperature. This can be physically interpreted as increasing the thermal energy causes the breaking up of Cooper pairs. Since the number of Cooper pairs and the order parameter are linked, as we have from the condensate fraction (3.45) and the corresponding Figure 3.4 in the zero-temperature limit, we can conclude that a decreasing of the condensate fraction lowers the order parameter.

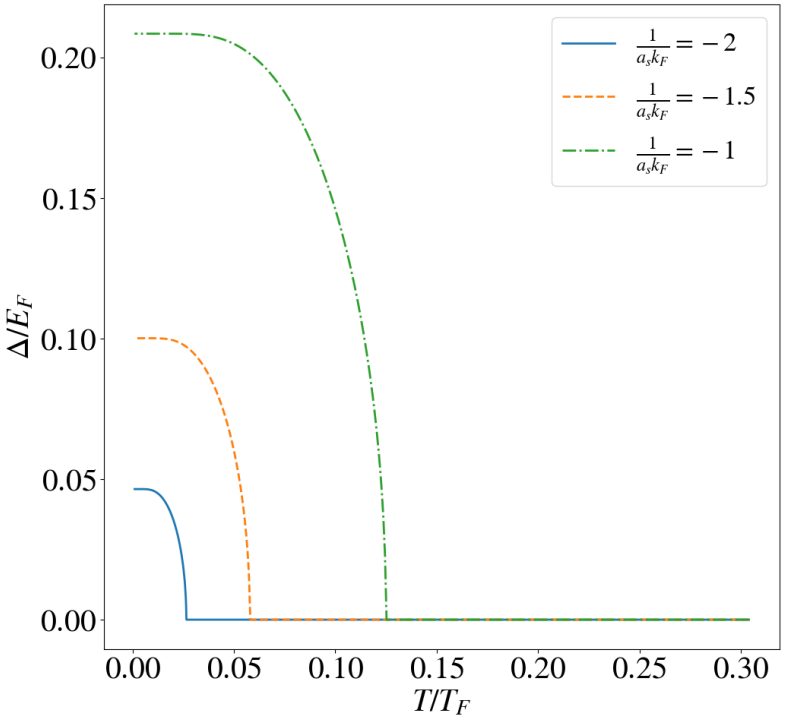

Figure 3.6.: Plot of the order parameter Δ following from the dimensionless quantities introduced in (3.51) under consideration of the two equations (3.52) and (3.54). The order parameter is shown in units of the Fermi energy for several s-wave scattering lengths, located in the BCS regime.

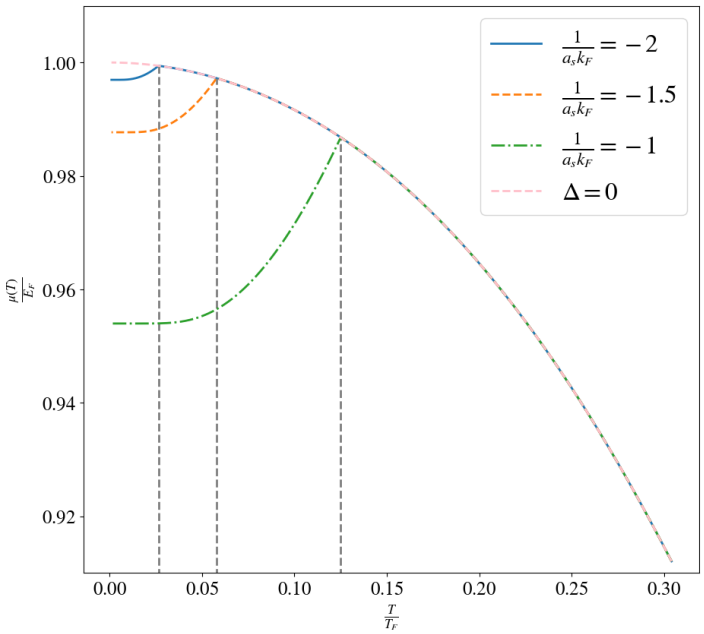

Figure 3.7.: Plot of chemical potential in units of the Fermi energy as function of temperature. Again the chemical potential is solved self-consistently from (3.52) and (3.54).

The temperature dependence of the chemical potential, which is represented in Figure 3.7, turns out to be more involved: Up to the corresponding critical temperature for a given s-wave scattering length a_s, the chemical potential increases. Since the breaking up of the Cooper pairs increases the internal energy in the system, the chemical potential increases also up to the critical temperature. This is based on the early observation of Cooper himself, that Cooper pairing is characterised by an energetic favourable state of two electrons [9]. Above the critical temperature, the superfluid phase vanishes and the Fermi gas behaves like an ideal Fermi gas. Consequently, the chemical potential decreases for higher temperatures.

In particular, we have seen in this chapter that the critical temperature is of central importance. Therefore, we determine its behaviour as a function of the parameter $1/a_s k_F$ in the next section.

3.4. Evaluation of Critical Temperature

In order to determine the temperature dependence of the order parameter and the chemical potential it is essential to know, in which temperature regime the order parameter vanishes, as we have seen in Figure 3.6 and 3.7. To calculate the critical temperature T_C, we deal with the order-parameter equation (3.8) and consider the limiting case of vanishing order parameter.

The order-parameter equation for temperatures above T_C is trivially solved by the case $\Delta = 0$. However, since the order-parameter equation has to be fulfilled also in the limiting case $T \to T_C$, setting $\Delta = 0$ in the order-parameter equation (3.54) yields the critical temperature

$$\frac{\pi}{2a_s k_F} = \left[\frac{b_C}{4}\int_0^\infty \mathrm{d}\xi \frac{\sqrt{\xi}^3}{\cosh^2\left(|\xi \mp 1|\frac{b_C}{2}\right)}\right]^{-\frac{1}{3}} \times \int_0^\infty \mathrm{d}\xi \frac{\sqrt{\xi}}{|\xi \mp 1|^3}\left[(1 \mp \xi)\tanh\left(|\xi \mp 1|\frac{b_C}{2}\right) + \frac{b_C}{2}\frac{|\xi \mp 1|\xi(\xi \mp 1)}{\cosh^2\left(|\xi - 1|\frac{b_C}{2}\right)}\right], \quad (3.55)$$

which includes the temperature dependence in the inverse thermal energy β, where the chemical potential follows again from (3.52) for $\zeta = 0$. Assuming the limiting case of low temperatures $T \to 0$, as well as

$$E_F >> k_B T_C \quad (3.56)$$

we obtain for the critical temperature an approximative result, as it is shown in the appendix B.2

$$T_C = \frac{8}{\pi}\frac{\gamma}{e^2} T_F \exp\left(\frac{\pi}{2a_s k_F}\right) \quad (3.57)$$

with $\gamma = e^C$, where C denotes Euler's constant, see also [35]. An improvement of this result, is the semi-numerical solution, which is solved self-consistently

$$T_C = \frac{8}{\pi}\frac{\gamma}{e^2}\frac{\mu(T_c)}{k_B} \exp\left(\frac{\hbar\pi}{2a_s\sqrt{2M\mu(T_c)}}\right), \quad (3.58)$$

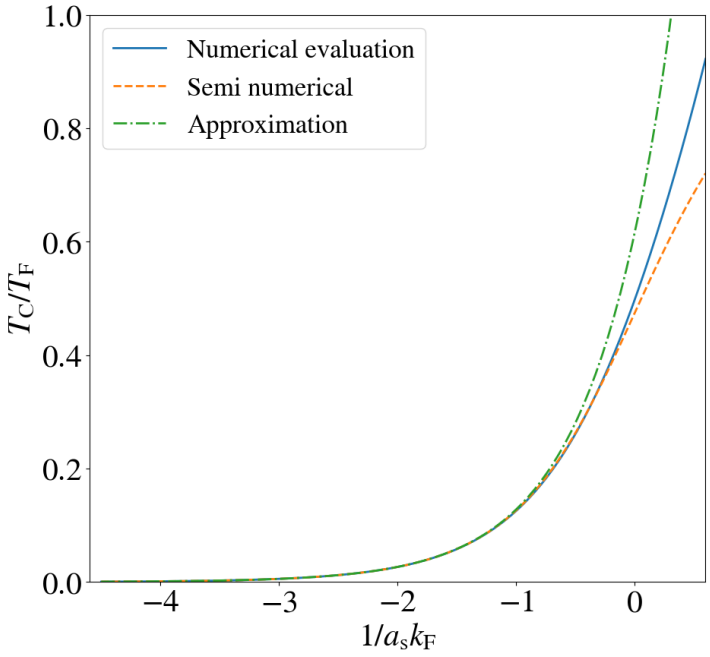

Figure 3.8.: Illustration of the critical temperature T_C. The numerical evaluation is evaluated from (3.55) and the semi-numerical result in (3.58), as well as the approximation from (3.57).

with the temperature-dependent chemical potential from (3.52) for the limiting case $\zeta \to 0$. To evaluate the quality of the approximation, we compare this result with the numerical evaluation of (3.55). Analysing the behaviour of the critical temperature in the deep BCS regime given by $1/a_s k_F < -1$ according to Figure 3.8, we observe that the approximation formulas agree with the numerical behaviour from (3.55) with high agreement. The semi-numerical approach shows a high agreement with the numerical result even further up to $1/a_s k_F = -0.5$. Additionally, considering the plot of the critical temperature by Sá de Melo et al. [37], which was shown in the introduction in Figure 1.3, we can conclude from our results that the curve shown therein, which diverges in the BEC limit, coincides to our numerical evaluation.

4. Harmonic Trapping Potential

As motivated in the introduction, we work out here the theory for a corresponding ^{6}Li experiment. Considering the experimental setup, the atoms are trapped in a harmonic trapping confinement. Consequently, we have to introduce a tri-axial harmonic trapping potential

$$V(\boldsymbol{x}) = \frac{M}{2} \sum_{i=1}^{3} \omega_i^2 x_i^2 \tag{4.1}$$

to our theory, where ω_i with $i = 1, 2, 3$ denote the respective trap frequencies.

According to the initial Hamilton operator (2.1), it would be possible to add the trapping potential (4.1) as a further term to the free fermionic part. However, this causes major difficulties, since the transformation into the reciprocal space, which is necessary for the diagonalisation of the Hamilton operator, is then no longer possible. Therefore, we are searching for the most elegant way to introduce the trapping potential at least approximately to the self-consistency equations. This leads us directly to the local-density approximation (LDA).

4.1. Local Density Approximation

The assumption of the local density approximation is a slowly varying trapping potential compared to a single-particle wave function, which allows us to approximate locally the density of states with the homogeneous case [55]. Consequently, the spatial-dependent chemical potential

$$\mu(\boldsymbol{x}) = \mu - V(\boldsymbol{x}) \tag{4.2}$$

is introduced to the above self-consistency equations for the homogeneous Fermi gas [56]. This rises the question, which condition has to be fulfilled to apply this approximation. In order to apply LDA, the relevant energies have to be small compared to the single-particle oscillator energies

$$\mu \ll \hbar\omega_i. \tag{4.3}$$

As we have already seen, the chemical potential is of the order of the Fermi energy. In the next chapter, we will check this condition explicitly for the ideal Fermi gas in the zero-temperature limit.

We will now adapt the procedure of the homogeneous Fermi gas to that of the harmonic confinement within LDA and investigate various limiting cases, as well as evaluate the entire self-consistency equations finally numerically.

4.2. BCS- and BEC-Limit at Zero Temperature

In the beginning, we motivated the BCS theory on the basis of the BCS-BEC crossover. This rises generally the question in which limiting case the cloud becomes larger. Therefore, we will set up an excursion on the BEC regime.

4.2.1. Zero-Temperature Limit for Ideal Fermi Gas

Considering the particle-number equation (3.4) for the limiting case $T \to 0$ and neglecting interactions, the order parameter vanishes and we describe an ideal Fermi gas. To this end, we introduce the Heaviside step function [57]

$$\begin{aligned} \Theta: \quad & \mathbb{R} \to \{0,1\} \\ & x \mapsto \begin{cases} 0: & x < 0 \\ 1: & x \geq 0 \end{cases} \end{aligned} \tag{4.4}$$

and obtain for the particle-number density

$$n(\boldsymbol{x}) = 2 \int \frac{\mathrm{d}^3 k}{(2\pi)^3} \, \Theta\left(\mu - \frac{\hbar^2 \boldsymbol{k}^2}{2M} - V(\boldsymbol{x})\right). \tag{4.5}$$

Here the prefactor two follows from the presence of spin up and down fermions, which are energetically degenerate. Dealing with a gas of fermions for which the Pauli exclusion principles applies, the energetic states in reciprocal space are filled up from $\boldsymbol{k} = \boldsymbol{0}$ up to the boundary wave vector $|\boldsymbol{k}| = k_\mathrm{F}$. The states lie within a sphere, which is called the Fermi sphere [51]. Consequently, the integration in the particle-number density (4.5) can be performed using this spherical symmetry. This yields

$$n(\boldsymbol{x}) = \frac{1}{3\pi^2} \int_0^{k_\mathrm{F}(\boldsymbol{x})} \mathrm{d}k \, k^2 = \frac{k_\mathrm{F}^3(\boldsymbol{x})}{3\pi^2} \tag{4.6}$$

with the corresponding Fermi momentum

$$k_\mathrm{F}(\boldsymbol{x}) = \sqrt{\frac{2M}{\hbar^2} \left[\mu - V(\boldsymbol{x})\right]}, \tag{4.7}$$

which becomes spatial dependent due to the local-density approximation. Especially, we can conclude that the Fermi momentum in the center of the trap is equal to the one of the homogeneous case. Analysing the equation for particle-number density (4.6) and the Fermi momentum (4.7), we see that the fermionic cloud is bounded, since the Fermi momentum vanishes for $\mu = V(\boldsymbol{x}_\mathrm{TF})$ with $r_{\mathrm{TF},i} = \boldsymbol{x}_\mathrm{TF} \boldsymbol{e}_i$, where $r_{\mathrm{TF},i}$ denotes the Thomas-Fermi radius. Consequently, we obtain an expression for the Thomas-Fermi radius in the zero-temperature limit

$$r_{\mathrm{TF},i} = \sqrt{\frac{2E_\mathrm{F}}{M\omega_i^2}}, \tag{4.8}$$

where the chemical potential μ is equal to the Fermi energy E_F, because of the zero-temperature limit and the index i denotes again the associated direction. The Fermi energy E_F is determined from the particle number N. Performing a spatial integration of the particle-number density (4.5)

$$N = \int \mathrm{d}^3 x \, n(\boldsymbol{x}) \tag{4.9}$$

fixes the Fermi energy

$$E_\mathrm{F} = \hbar\tilde{\omega}(3N)^{\frac{1}{3}} \tag{4.10}$$

with the geometric mean of the trapping frequencies

$$\tilde{\omega} = \sqrt[3]{\omega_x \omega_y \omega_z}. \tag{4.11}$$

Therefore, we obtain for the Thomas-Fermi radius (4.8) finally

$$r_{\mathrm{TF},i} = \sqrt{2}(3N)^{\frac{1}{6}} \frac{\tilde{\omega}}{\omega_i} l \tag{4.12}$$

with the oscillator length

$$l = \sqrt{\frac{\hbar}{M\tilde{\omega}}}. \tag{4.13}$$

Thus, the condition for applying LDA (4.3) can be checked: Regarding our system of harmonically trapped fermions in the zero-temperature limit, we identify μ with (4.10) and the condition (4.3) simplifies to

$$\frac{\omega_i}{\sqrt[3]{3N\omega_x\omega_y\omega_z}} \ll 1. \tag{4.14}$$

Consequently, we can see that for an aspect ratio of 7, like it is present in the corresponding experiment [44], and large particle numbers $10^5 - 10^7$, the application of LDA is justified, since $\frac{\omega_i}{\sqrt[3]{3N\omega_x\omega_y\omega_z}} < 0.07$.

4.2.2. Interacting Bose Gas at Zero Temperature

To investigate the behaviour in the bosonic regime, we have to make a digression: The description of the BEC is based on Gross-Pitaevskii equation [58]

$$i\hbar\frac{\partial}{\partial t}\psi(\boldsymbol{x},t) = \left[-\frac{\hbar^2}{2M_{\mathrm{B}}}\Delta + V(\boldsymbol{x})\right]\psi(\boldsymbol{x},t) + g_{\mathrm{B}}|\psi(\boldsymbol{x},t)|^2\psi(\boldsymbol{x},t), \tag{4.15}$$

which has the stationary solution

$$\psi(\boldsymbol{x},t) = \psi(\boldsymbol{x})e^{-\frac{i}{\hbar}\mu t} \tag{4.16}$$

leading to the time-independent Gross-Pitaevskii equation

$$\mu\psi(\boldsymbol{x}) = \left[-\frac{\hbar^2}{2M_{\mathrm{B}}}\Delta + V(\boldsymbol{x})\right]\psi(\boldsymbol{x}) + g_{\mathrm{B}}|\psi(\boldsymbol{x})|^2\psi(\boldsymbol{x}). \tag{4.17}$$

As the s-wave scattering length between the ^{6}Li-molecules of about 4000 a_0 is much larger than the s-wave scattering length of atomic BECs, which are of the order of 100 a_0, we have to apply the Thomas-Fermi approximation. Thus, we neglect the kinetic energy in comparison with the potential and the interacting energy in (4.17) and the differential equation simplifies to an algebraic equation:

$$|\psi_{\mathrm{TF}}(\boldsymbol{x})|^2 = n_{\mathrm{TF}}(\boldsymbol{x}) = \frac{\mu - V(\boldsymbol{x})}{g_{\mathrm{B}}} \tag{4.18}$$

The positivity of the density (4.18) implies the condition

$$\mu - V(\boldsymbol{x}) \geq 0. \tag{4.19}$$

This restricts the coordinates $\boldsymbol{x}$, where the condensate wave function is non-vanishing. Similar to the BCS limit, the chemical potential is fixed by the particle number and follows from

$$N_{\mathrm{B}} = \frac{1}{g_{\mathrm{B}}}\int \mathrm{d}^3x \left[\mu - \frac{M_{\mathrm{B}}}{2}\sum_{i=x,y,z}\omega_i^2 x_i^2\right]. \tag{4.20}$$

The density cloud describes also here an ellipsoid. To simplify our procedure, we perform a coordinate transformation from an ellipsoid to the unit sphere via

$$y_i = \sqrt{\frac{M_{\mathrm{B}}\omega_i^2}{2\mu}}x_i. \tag{4.21}$$

The condition (4.19) thus simplifies to the dimensionless form

$$\sum_{i=x,y,z} y_i^2 \geq 1, \tag{4.22}$$

which fixes the chemical potential

$$\mu = \frac{15^{\frac{2}{5}}}{2}\left(\frac{a_{\mathrm{s}}^{\mathrm{B}}N_{\mathrm{B}}}{l_{\mathrm{B}}}\right)^{\frac{2}{5}}\hbar\tilde{\omega}, \tag{4.23}$$

where $\tilde{\omega} = \sqrt[3]{\omega_x\omega_y\omega_z}$ denotes again the geometric mean of the trapping frequencies and l_{B} the oscillator length from (4.13) with the respective quantities in the bosonic case. Consequently, we obtain the Thomas-Fermi radius

$$r_{\mathrm{TF},i}^{\mathrm{BEC}} = 15^{\frac{1}{5}}\left(\frac{a_{\mathrm{s}}^{\mathrm{B}}N_{\mathrm{B}}}{l_{\mathrm{B}}}\right)^{\frac{1}{5}}\frac{\tilde{\omega}}{\omega_i}l_{\mathrm{B}}. \tag{4.24}$$

This allows us to compare the Thomas-Fermi radius in the BEC (4.24) with the corresponding one (4.12) in the BCS limit.

4.2.3. Comparison between Fermionic and Bosonic Limit

Generally, the question arises, which limiting case has the larger particle cloud. Considering cold atoms cooled down to quantum degeneracy in the fermionic limit, the Fermi pressure determines the size of the particle cloud, whereas in the bosonic limit the repulsive interaction between individual bosons defines the size of the cloud. Therefore, the Thomas-Fermi radius becomes a function of the interacting strength given by s-wave scattering length (4.24). For this purpose, we need to relate the quantities from the BEC to the corresponding quantities in the BCS limit. Since, the ^{6}Li atoms form molecules the particle number is halved $N_{\mathrm{B}} = N/2$ and accordingly the mass is doubled $M_{\mathrm{B}} = 2M$. Furthermore, the s-wave scattering length needs to be adjusted $a_{\mathrm{s}}^{\mathrm{B}} = 0.6a_{\mathrm{s}}$ [59]. Regarding positive s-wave scattering lengths in the BEC limit, we determine the ratio between the Thomas-Fermi radius in the bosonic limit and the BCS limit

$$\frac{r_{\mathrm{TF},i}^{\mathrm{BEC}}}{r_{\mathrm{TF},i}} = \left(\frac{3}{64}a_{\mathrm{s}}k_{\mathrm{F}}\right)^{\frac{1}{5}}, \tag{4.25}$$

which is spatially independent and is shown in Figure 4.1. In the unitary regime characterised by $a_{\mathrm{s}} \to \infty$ the cloud starts to become smaller than in the fermionic limit and finally in the deep BEC regime $a_s \downarrow 0$ the cloud is half as large than in the fermionic limit. Especially, the smaller cloud in the deep BEC regime compared to the BCS regime can already be observed in the experimental density plots shown in Figure 1.5 with the bare eye.

4.3. Interacting Fermi Gas in Low-Temperature Limit

In the limiting case $T \to 0$, where we introduced for the homogeneous Fermi gas the parameter t in (3.17), which was fixed by the s-wave scattering length a_{s} according to

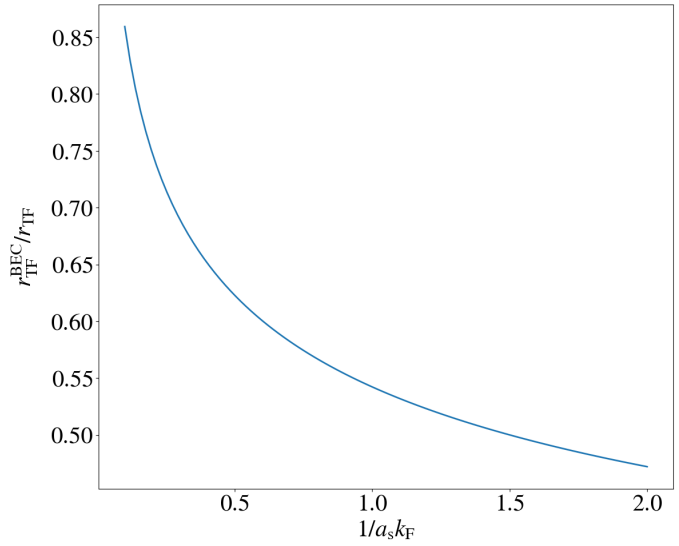

Figure 4.1.: Ratio between the Thomas-Fermi radius in the BEC limit as function of the s-wave scattering length (4.24) and the Thomas-Fermi radius in the BCS limit (4.12). The Thomas-Fermi radius decreases monotonically as function of the inverse scattering length. The trapping frequencies $\omega_x = 2\pi \times 195$ Hz, $\omega_y = 2\pi \times 22.6$ Hz and $\omega_z = 2\pi \times 129$ Hz are chosen according to the experimental setup. The particle number and the direction are redundant, since they are canceled by the ratio (4.25).

(3.27), we represented the chemical potential μ in (3.28) and the order parameter Δ in (3.29) as a function of this parameter. The introduction of LDA leads to a spatial dependent parameter $t(\boldsymbol{x})$, which is compensated by the spatial dependence of the Fermi momentum

$$\frac{1}{a_{\mathrm{s}} k_{\mathrm{F}}(\boldsymbol{x})} = \frac{2}{\pi} \frac{2\mathrm{E}\left(\sqrt{\frac{1+t(\boldsymbol{x})}{2}}\right) - \mathrm{K}\left(\sqrt{\frac{1+t(\boldsymbol{x})}{2}}\right)}{\left[t(\boldsymbol{x})\mathrm{E}\left(\sqrt{\frac{1+t(\boldsymbol{x})}{2}}\right) + \frac{1-t(\boldsymbol{x})}{2}\mathrm{K}\left(\sqrt{\frac{1+t(\boldsymbol{x})}{2}}\right)\right]^{\frac{1}{3}}}. \tag{4.26}$$

Using the definition of the parameter

$$t(\boldsymbol{x}) = \frac{\tilde{\mu}(\boldsymbol{x})}{\sqrt{\tilde{\mu}(\boldsymbol{x})^2 + \tilde{\Delta}(\boldsymbol{x})^2}} \tag{4.27}$$

leads to the spatial dependent order parameter

$$\tilde{\Delta}(\boldsymbol{x}) = \tilde{\mu}(\boldsymbol{x}) \sqrt{\frac{1}{t(\boldsymbol{x})^2} - 1}. \tag{4.28}$$

Thus, for a given chemical potential μ, the spatial behaviour of the order parameter can be calculated. The chemical potential can be determined by an additional approximation: Assuming small interactions, which is justified since we are investigating the BCS limit of the crossover, we can deal with the limiting case $\Delta \to 0$. To this end, the chemical potential is equal to the Fermi energy (4.10)

$$\mu_0 = \sqrt[3]{3N}\hbar\tilde{\omega}. \tag{4.29}$$

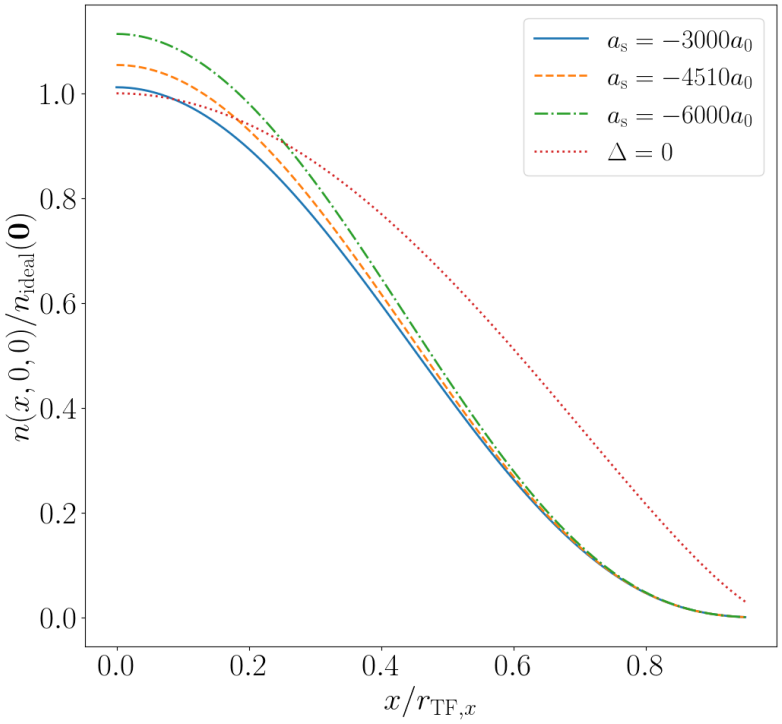

Figure 4.2.: Particle-number density (4.30) for different s-wave scattering lengths. The chemical potential follows from the estimation (4.29), which explains why the particle numbers vary for different scattering lengths. The red dotted line shows the behaviour of the ideal Fermi gas according to (4.6).

This result is equivalent to the zeroth-order perturbative result in the homogeneous case (3.39). The spatial-dependent particle-number density

$$n(\boldsymbol{x}) = \frac{k_{\mathrm{F}}(\mathbf{0})^3}{4\pi^2} \int_0^\infty \mathrm{d}\tilde{\epsilon}\, \sqrt{\tilde{\epsilon}} \left[1 - \frac{\tilde{\epsilon} - \tilde{\mu}_0(\boldsymbol{x})}{\sqrt{[\tilde{\epsilon} - \tilde{\mu}_0(\boldsymbol{x})]^2 + \tilde{\Delta}(\boldsymbol{x})^2}} \right] \tag{4.30}$$

can be determined with the spatial-dependent order parameter (4.28) and the scaled chemical potential

$$\tilde{\mu}_0(\boldsymbol{x}) = \frac{\mu_0 - V(\boldsymbol{x})}{E_F} \tag{4.31}$$

with above estimation of the homogeneous chemical potential (4.29). The influence of the order parameter on the particle-number density is studied in Figure 4.2. This leads to the conclusion that the presence of the order-parameter leads to a higher density in the center of the trap. Therefore the particle-number density decreases at the same time near the Thomas-Fermi radius, since the total particle number must be conserved. However, since the chemical potential is approximated by (4.29) and not calculated self-consistently with the order parameter, different scattering lengths lead to different particle numbers in Figure 4.2.

Also for the case of a harmonically-trapped interacting Fermi gas, an approximation for the order parameter similar to the one for the homogeneous case (3.40) can be introduced. Considering LDA, the spatial dependent zeroth-order approximation of the gap parameter

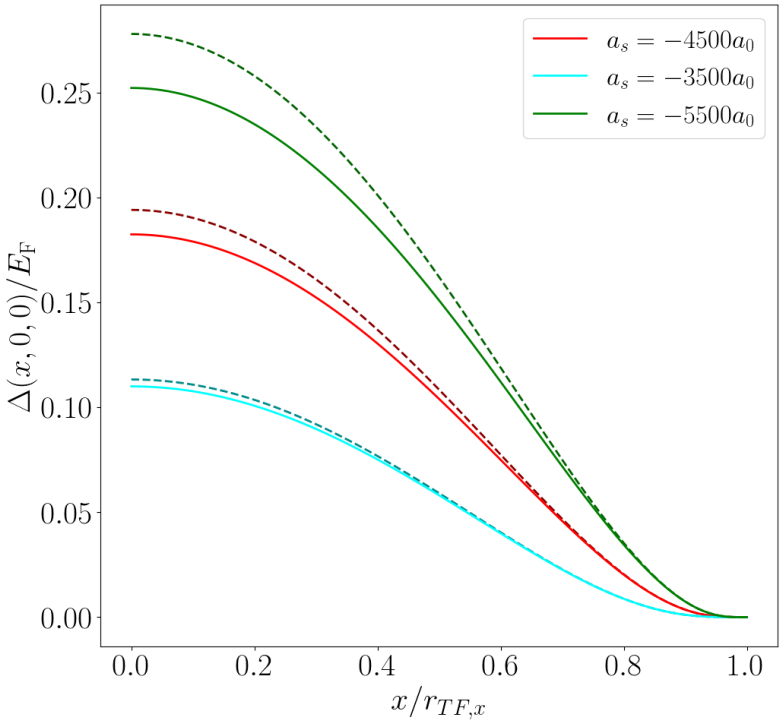

Figure 4.3.: Spatial dependence of the zero-temperature limit for the order parameter. The dashed lines show the approximation based on (4.32), whereas the solid lines show the numerical evaluation according to (4.28). The chemical potential is approximated by the Fermi energy (4.29) in combination with LDA.

becomes

$$\Delta_0(\boldsymbol{x}) = \frac{8}{e^2}\left[\mu_0 - V(\boldsymbol{x})\right] \exp\left(\frac{\pi}{2a_s k_F(\boldsymbol{x})}\right). \tag{4.32}$$

From this expression it can be followed that the zeroth-order perturbative expression for the order parameter vanishes at the Thomas-Fermi radius, as well as the particle-number density. The resulting behaviour of the order parameter is shown in Figure 4.3. The approximation (4.32) has higher agreement with the numerical behaviour for larger radii. In the center of the trap the LDA result is equivalent to the homogeneous case. Consequently, we can see that for larger negative s-wave scattering lengths, the assumption of small interactions is less justified, so we observe a larger deviation between this approximation and the numerical evaluation based on (4.28). Comparing the spatial behaviour of the particle number density in Figure 4.2 with the order parameter in Figure 4.3, we can observe that both quantities decrease up to the Thomas-Fermi radius, where both quantities vanish in the zero-temperature limit.

After we studied the impact of interactions for a Fermi gas at zero temperature, we consider the temperature dependence of the ideal Fermi gas. For this purpose we take into account temperatures above the critical temperature, where the order parameter vanishes to describe the temperature dependence of the experimentally measurable particle-number density.

4.4. Ideal Fermi Gas in a Trap for Finite Temperatures

For temperatures T above the critical temperature T_C, the order parameter vanishes. Consequently, the order-parameter equation (2.45) is solved by the trivial case $\Delta = 0$. Thus, we need to solve only the particle-number equation (3.7), where we set $\Delta = 0$ and introduce the harmonic trapping potential due to LDA (4.2)

$$n(\boldsymbol{x}) = \frac{2}{\sqrt{\pi}} \left(\frac{M}{2\pi\hbar^2}\right)^{\frac{3}{2}} \int_0^\infty \mathrm{d}\epsilon \sqrt{\epsilon} \left\{1 - \tanh\left(\frac{\beta}{2}\left[\epsilon - \mu(\boldsymbol{x})\right]\right)\right\}. \tag{4.33}$$

Performing a partial integration in the ϵ-integral, we convert the spatial-dependent particle-number density (4.33) to

$$n(\boldsymbol{x}) = \frac{\sqrt{2}\beta}{6\pi^2} \left(\frac{\sqrt{M}}{\hbar}\right)^3 \int_0^\infty \mathrm{d}\epsilon \frac{\sqrt{\epsilon}^3}{\cosh^2\left(\frac{\beta}{2}\left[\epsilon - \mu(\boldsymbol{x})\right]\right)}. \tag{4.34}$$

Carrying out a spatial integration of this particle-number density follows the particle number. Since we are dealing with a fixed particle number in the grand-canonical ensemble, this fixes the chemical potential

$$N = \frac{\sqrt{2}\beta}{6\pi^2} \left(\frac{\sqrt{M}}{\hbar}\right)^3 \int_{-\infty}^\infty \mathrm{d}x \int_{-\infty}^\infty \mathrm{d}y \int_{-\infty}^\infty \mathrm{d}z \int_0^\infty \mathrm{d}\epsilon \frac{\sqrt{\epsilon}^3}{\cosh^2\left(\frac{\beta}{2}\left[\epsilon - \mu(\boldsymbol{x})\right]\right)}. \tag{4.35}$$

In order to perform the spatial integration, we transform the integral to isotropic coordinates

$$X = \sqrt{\frac{M}{2}}\omega_x x, \quad Y = \sqrt{\frac{M}{2}}\omega_y y, \quad Z = \sqrt{\frac{M}{2}}\omega_z z, \tag{4.36}$$

which allows us to introduce spherical coordinates

$$r = \sqrt{X^2 + Y^2 + Z^2} \tag{4.37}$$

using the symmetry properties of the integrand. At this point, it has to be kept in mind that r does not denote the radius, since it has the physical dimension of a square root of an energy. By introducing isotropic quantities X, Y and Z, we transform the particle cloud from an ellipsoid in usual coordinates to a sphere. Therefore, we plug in spherical coordinates denoted by above r, which leads to the explanation for the naming. Using these new coordinates will prove to be extremely valuable, since the spatial-dependence of the self-consistency equations will be described completely by r. In particular, there is no need to consider any angular-dependent part, since the integrand contains only the radial component and yields

$$N = \frac{2\beta}{3(\hbar\tilde{\omega})^3\pi^2} \int_0^\infty \mathrm{d}r \int_0^\infty \mathrm{d}\epsilon \frac{\sqrt{\epsilon}^3 r^2}{\cosh^2\left(\frac{\beta}{2}\left[\epsilon - \mu + r^2\right]\right)}. \tag{4.38}$$

To simplify the numerical evaluation further, we perform a last substitution

$$\bar{\epsilon} = \frac{\beta}{2}\epsilon, \quad \bar{\mu} = \frac{\beta}{2}\mu, \quad \bar{r} = \sqrt{\frac{\beta}{2}}r \tag{4.39}$$

leading to the integral

$$N = \frac{128}{3\pi\left(\hbar\bar{\omega}\right)^3} \int_0^\infty \mathrm{d}\bar{r} \int_0^\infty \mathrm{d}\bar{\epsilon} \frac{\sqrt{\bar{\epsilon}}^3 \bar{r}^2}{\cosh^2\left(\bar{\epsilon} - \bar{\mu} + \bar{r}^2\right)} \tag{4.40}$$

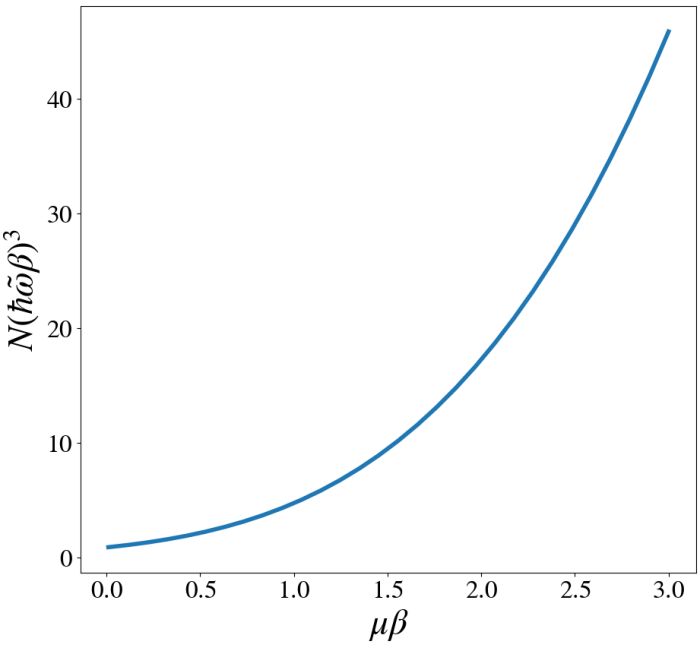

Figure 4.4.: Illustration of the particle-number equation (4.43), which shows the polylogarithmic function of third order.

for the particle number. This allows us to calculate the corresponding chemical potential for a given temperature T and particle number N numerically. The integral in (4.40) can be represented via polylogarithmic functions, which are introduced in the appendix (C.1): Writing the cosh in terms of the exponential function

$$\frac{1}{\cosh^2 x} = \frac{1}{(e^x + e^{-x})^2} = \frac{e^{-2x}}{(1 + e^{-2x})^2} \tag{4.41}$$

and introducing the geometric series

$$\frac{e^{-z}}{(1 + e^{-z})^2} = \frac{\partial}{\partial z} \frac{1}{1 + e^{-z}} = \sum_{k=1}^{\infty} (-1)^k (-k) e^{-zk} \tag{4.42}$$

follows the representation of the remaining sum by a polylogarithmic function immediately. Indeed, the remaining integrals are Gaussian and can be calculated straight-forward

$$N = -\frac{2}{(\hbar\bar{\omega}\beta)^3} \sum_{k=1}^{\infty} \frac{(-1)^k}{k^3} e^{2k\bar{\mu}} = -2 \frac{\mathrm{Li}_3\left(-e^{2\bar{\mu}}\right)}{(\hbar\tilde{\omega}\beta)^3}. \tag{4.43}$$

To get a first overview of the course of the polylogarithmic function of third order, we investigate its behaviour in Figure 4.4. From this, deductions can be made for later numerical determinations of the chemical potential.

In order to compare our theoretical results to experimentally measurable quantities, we derive the two-dimensional column density. To this end, we start again from the particle-number density (4.34) and perform only a single spatial integration over the z-direction

$$n(x, y) = \int_{-\infty}^{\infty} \mathrm{d}z \, n(\boldsymbol{x}). \tag{4.44}$$

Again, we use the representation of the cosh-function with the exponential function (4.41) together with the series (4.42) and perform the Gaussian integrals yielding

$$n(x,y) = -\frac{M}{\omega_z \beta^2 \pi \hbar^3} \mathrm{Li}_2\left(-e^{2\left[\bar{\mu}-\frac{\beta M}{4}\left(\omega_x^2 x^2+\omega_y^2 y^2\right)\right]}\right) \tag{4.45}$$

with the polylogarithmic function of order two. Performing a further integration in y-

$$n(x) = -\frac{\sqrt{2M}}{\sqrt{\pi}\hbar^3 \omega_y \omega_z \sqrt{\beta}^5} \mathrm{Li}_{\frac{5}{2}}\left(-e^{2\left[\bar{\mu}-\frac{\beta M}{4}\omega_x^2 x^2\right]}\right) \tag{4.46}$$

or x-direction

$$n(y) = -\frac{\sqrt{2M}}{\sqrt{\pi}\hbar^3 \omega_x \omega_z \sqrt{\beta}^5} \mathrm{Li}_{\frac{5}{2}}\left(-e^{2\left[\bar{\mu}-\frac{\beta M}{4}\omega_y^2 y^2\right]}\right) \tag{4.47}$$

leads to the respective one-dimensional line density, which contains this time the polylogarithmic function of order $5/2$.

After we studied the ideal Fermi gas, the question comes up, in which temperature regime the Fermi gas is described by an ideal Fermi gas. For this purpose we calculate the critical temperature in the harmonic trap.

4.5. Critical Temperature

Regarding the numerical evaluation of the critical temperature in the homogeneous case from the previous section (3.55), we have to introduce LDA (4.2) to calculate the critical temperature in a harmonic trapping confinement

$$\begin{aligned}\frac{\pi}{2a_s k_F(\boldsymbol{x})} = &\left[\frac{b_C(\boldsymbol{x})}{4}\int_0^\infty \mathrm{d}\xi \frac{\sqrt{\xi}^3}{\cosh^2\left(|\xi\mp 1|\frac{b_C(\boldsymbol{x})}{2}\right)}\right]^{-\frac{1}{3}} \\ &\times \int_0^\infty \mathrm{d}\xi \frac{\sqrt{\xi}}{|\xi\mp 1|^3}\left[(1\mp\xi)\tanh\left(|\xi\mp 1|\frac{b_C(\boldsymbol{x})}{2}\right)+\frac{b_C(\boldsymbol{x})}{2}\frac{|\xi\mp 1|\xi(\xi\mp 1)}{\cosh^2\left(|\xi-1|\frac{b_C(\boldsymbol{x})}{2}\right)}\right].\end{aligned} \tag{4.48}$$

Similar to the case of the order parameter (4.32), we introduce LDA also to the approximative formula (3.57), which yields

$$T_C(\boldsymbol{x}) = \frac{8}{\pi} e^{C-2}\frac{\mu_0 - V(\boldsymbol{x})}{k_B}\exp\left(\frac{\hbar\pi}{2a_s\sqrt{2M[\mu_0 - V(\boldsymbol{x})]}}\right), \tag{4.49}$$

as well as for the semi-numerical result (3.58)

$$T_C(\boldsymbol{x}) = \frac{8}{\pi} e^{C-2}\left[\mu(T_C) - V(\boldsymbol{x})\right]\exp\left(\frac{\hbar\pi}{2a_s\sqrt{2M[\mu(T_C) - V(\boldsymbol{x})]}}\right), \tag{4.50}$$

which contains as extension the temperature dependence of the chemical potential, which is calculated numerically from (4.40). Accordingly, the critical temperature has to be calculated self-consistently in the semi-numerical case, since the chemical potential depends on the temperature as well. In the following, we evaluate the critical temperature for the center of the trap $\boldsymbol{x} = \boldsymbol{0}$, where the critical temperature for superfluidity has its maximum, since we are particularly interested to see at which temperature superfluidity starts. How-

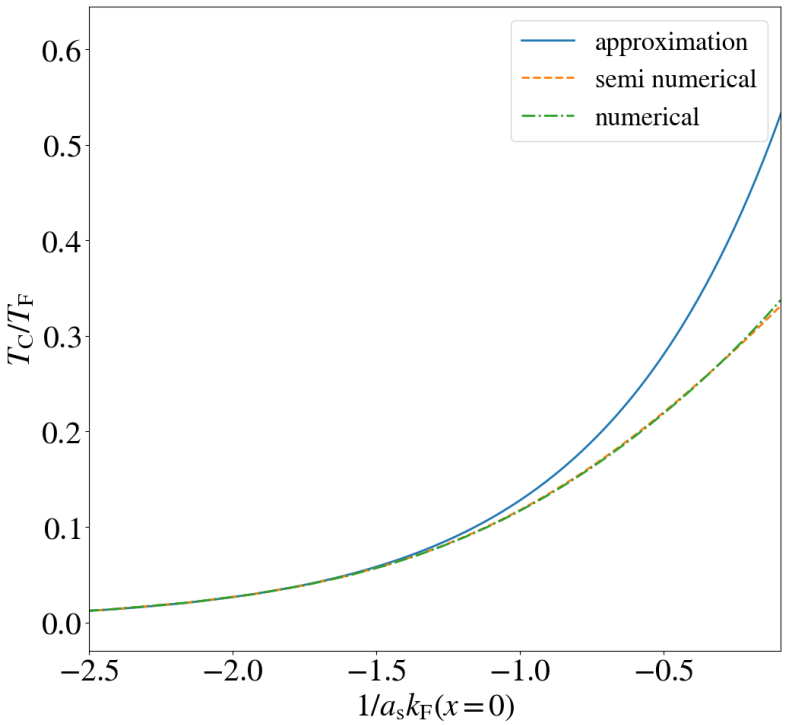

Figure 4.5.: Numerically evaluated critical temperature from (4.48), semi-numerical result (4.49) and the approximation (4.50). Analogous to the homogeneous case in Figure 3.8, we see the exponential increase of the critical temperature for larger negative s-wave scattering lengths. We focus on the center of the trap $\boldsymbol{x} = \mathbf{0}$, since the critical temperature reaches its maximum value there and we are looking for the highest temperature, where superfluidity starts to occur.

ever, the semi-numerical approximation (4.50) gives us a better estimate about the impact of the s-wave scattering length, as it is shown in Figure 4.5. Here we can see especially that the behaviour from the two approximations matches the numerical result in the BCS limit. Approaching the unitary point, the semi-numerical result (4.50) agrees quite well with the numerical evaluation (4.48). From this we can read off the improvement of the semi-numerical result (4.50) compared to the approximation (4.49).

After we calculated the critical temperature in the case of a harmonic trapping potential, the question comes up, how the Fermi gas behaves in the superfluid case, i.e. in the temperature range $0 < T < T_C$. In this case, we have to evaluate both self-consistency equations in combination with LDA to determine both chemical potential and order parameter as functions of space and temperature.

4.6. Finite Temperature and Interacting Fermi Gas

Taking into account temperatures below the critical temperature, we have to evaluate both equations for order parameter and particle number self-consistently like in the homogeneous case in Figure 3.6 and 3.7. Thus, we investigate the order parameter as well as the particle-number density as a function of temperature and space. This allows us to calculate density profiles, which we can compare with the experimental column density and line density as has already been achieved for the BEC limit [45].

For this purpose, we start from both the particle-number equation (3.7) and the order-parameter equation (3.8) and introduce the harmonic trapping potential via LDA (4.2), which leads to

$$\frac{M}{2\pi a_s \hbar^2} = \frac{2}{\sqrt{\pi}} \left(\frac{M}{2\pi\hbar^2}\right)^{\frac{3}{2}} \int_0^\infty \mathrm{d}\epsilon \sqrt{\epsilon} \left[\frac{1}{\epsilon} - \frac{\tanh\left(\sqrt{(\epsilon-\mu(\boldsymbol{x},T))^2+\Delta(\boldsymbol{x},T)^2}\frac{\beta}{2}\right)}{\sqrt{(\epsilon-\mu(\boldsymbol{x},T))^2+\Delta(\boldsymbol{x},T)^2}}\right], \quad (4.51)$$

for the order-parameter equation as well as

$$n(\boldsymbol{x},T) = \frac{2}{\sqrt{\pi}} \left(\frac{M}{2\pi\hbar^2}\right)^{\frac{3}{2}} \int_0^\infty \mathrm{d}\epsilon \sqrt{\epsilon} \left[1 - \frac{(\epsilon-\mu(\boldsymbol{x},T)) \tanh\left(\sqrt{(\epsilon-\mu(\boldsymbol{x},T))^2+\Delta(\boldsymbol{x},T)^2}\frac{\beta}{2}\right)}{\sqrt{(\epsilon-\mu(\boldsymbol{x},T))^2+\Delta(\boldsymbol{x},T)^2}}\right] \quad (4.52)$$

for the particle-number equation. The spatial dependence of the order parameter is caused by the LDA as follows. The spatial dependence of the chemical potential in (4.51) needs to be compensated by the order parameter, since the remaining terms are spatially invariant.

4.6.1. Preparation of Self-Consistency Equations

In the following, we follow the procedure of the homogeneous case: Both expressions (4.51) and (4.52) are partially integrated to get rid of diverging terms, which cause difficulties for the numerical evaluation. In addition, we introduce dimensionless quantities, which are expressed in units of the Fermi energy in a harmonic trapping confinement (4.10). This

leads to the scaled quantities

$$\tilde{\epsilon} = \frac{\epsilon}{E_\mathrm{F}} \tag{4.53}$$

$$\tilde{\mu}(\boldsymbol{x}, T) = \frac{\mu(\boldsymbol{x}, T)}{E_\mathrm{F}} \tag{4.54}$$

$$\tilde{\Delta}(\boldsymbol{x}, T) = \frac{\Delta(\boldsymbol{x}, T)}{E_\mathrm{F}} \tag{4.55}$$

$$\tilde{\beta} = \beta E_\mathrm{F}. \tag{4.56}$$

Finally, our self-consistency equations for the numerical evaluation are given by

$$\begin{aligned}\frac{\pi}{2a_\mathrm{s}k_\mathrm{F}} = \int_0^\infty \mathrm{d}\tilde{\epsilon} \frac{\sqrt{\tilde{\epsilon}}}{\sqrt{[\tilde{\epsilon} - \tilde{\mu}(\boldsymbol{x}, T)]^2 + \tilde{\Delta}(\boldsymbol{x}, T)^2}^3} \\ \times \left[\left\{ \tilde{\mu}(\boldsymbol{x}, T)^2 + \tilde{\Delta}(\boldsymbol{x}, T)^2 - \tilde{\mu}(\boldsymbol{x}, T)\tilde{\epsilon} \right\} \tanh\left(\sqrt{[\tilde{\epsilon} - \tilde{\mu}(\boldsymbol{x}, T)]^2 + \tilde{\Delta}(\boldsymbol{x}, T)^2} \frac{\tilde{\beta}}{2} \right) \right. \\ \left. + \frac{\tilde{\beta}}{2} \frac{\sqrt{[\tilde{\epsilon}^\mathrm{T} - \tilde{\mu}(\boldsymbol{x}, T)]^2 + \tilde{\Delta}(\boldsymbol{x}, T)^2}\tilde{\epsilon}[\tilde{\epsilon} - \tilde{\mu}(\boldsymbol{x}, T)]}{\cosh^2\left(\sqrt{[\tilde{\epsilon} - \tilde{\mu}(\boldsymbol{x}, T)]^2 + \tilde{\Delta}(\boldsymbol{x}, T)^2} \frac{\tilde{\beta}}{2} \right)} \right]\end{aligned} \tag{4.57}$$

for the order parameter and

$$\begin{aligned}n(\boldsymbol{x}, T) = \frac{n_0}{2} \int_0^\infty \mathrm{d}\tilde{\epsilon} \sqrt{\frac{\tilde{\epsilon}}{[\tilde{\epsilon} - \tilde{\mu}(\boldsymbol{x}, T)]^2 + \tilde{\Delta}(\boldsymbol{x}, T)^2}}^3 \\ \times \left[\tilde{\Delta}(\boldsymbol{x}, T)^2 \tanh\left(\frac{\tilde{\beta}}{2} \sqrt{[\tilde{\epsilon} - \tilde{\mu}(\boldsymbol{x}, T)]^2 + \tilde{\Delta}(\boldsymbol{x}, T)^2} \right) \right. \\ \left. + \frac{\tilde{\beta}}{2} \frac{\sqrt{[\tilde{\epsilon} - \tilde{\mu}(\boldsymbol{x}, T)]^2 + \tilde{\Delta}(\boldsymbol{x}, T)^2}[\tilde{\epsilon} - \tilde{\mu}(\boldsymbol{x}, T)]^2}{\cosh^2\left(\frac{\tilde{\beta}}{2} \sqrt{[\tilde{\epsilon} - \tilde{\mu}(\boldsymbol{x}, T)]^2 + \tilde{\Delta}(\boldsymbol{x}, T)^2} \right)} \right]\end{aligned} \tag{4.58}$$

for the particle-number density. Note that we used the substitution according to the particle-number density in the zero-temperature limit (4.6)

$$n_0 = \frac{k_\mathrm{F}^3(\boldsymbol{x} = 0)}{3\pi^2} \tag{4.59}$$

where $k_\mathrm{F} = \sqrt{2ME_\mathrm{F}}/\hbar$.

4.6.2. Numerical Evaluation of Order Parameter and Particle Number

Since, we have to solve (4.57) and (4.58) self-consistently, we take into account a fixed particle number according to the grand-canonical ensemble. For this purpose, we have to perform a spatial integration of the particle-number density (4.58). To simplify the evaluation we transform the Cartesian coordinates to spherical coordinates in two steps:

For the beginning, we introduce again isotropic coordinates (4.36), which allow us to use once more the radial symmetry and proceed with the desired spherical coordinates (4.37) leading to the equation for the particle number

$$N(\tilde{\mu}(T), T) = \sqrt{\frac{2}{M}}^3 \frac{4\pi}{\tilde{\omega}^3} \int_0^\infty \mathrm{d}r\, r^2 n(r, \tilde{\mu}(T), T) \tag{4.60}$$

with the radial particle-number density

$$n(r,\tilde{\mu}(T),T) = \frac{n_0}{2}\int_0^\infty \mathrm{d}\tilde{\epsilon}\sqrt{\frac{\tilde{\epsilon}}{[\tilde{\epsilon}-\tilde{\mu}(T)+r^2]^2+\tilde{\Delta}(r,T)^2}}^3 \times\left[\tilde{\Delta}(r,T)^2\tanh\left(\frac{\tilde{\beta}}{2}\sqrt{[\tilde{\epsilon}-\tilde{\mu}(T)+r^2]^2+\tilde{\Delta}(r,T)^2}\right)+\frac{\tilde{\beta}}{2}\frac{\sqrt{[\tilde{\epsilon}-\tilde{\mu}(T)+r^2]^2+\tilde{\Delta}(r,T)^2}[\tilde{\epsilon}-\tilde{\mu}(T)+r^2]^2}{\cosh^2\left(\frac{\tilde{\beta}}{2}\sqrt{[\tilde{\epsilon}-\tilde{\mu}(T)+r^2]^2+\tilde{\Delta}(r,T)^2}\right)}\right] \tag{4.61}$$

as function of the temperature T and the chemical potential $\tilde{\mu}(T)$. As a consequence of the spherical symmetry due to above coordinate transformation the order parameter becomes a function of the square root of the energy r, too.

The procedure to solve the self-consistency equations is the following: Choosing a chemical potential allows us to solve the equation for the order parameter (4.57) and derive the spatial dependent order parameter for a given temperature. Thus, we can calculate the corresponding particle number from (4.60). If the desired number of particles does not follow from the chosen chemical potential, we adjust the choice of chemical potential in the next step so that the number of particles comes closer to the desired one. Iteratively, we repeat this procedure until we determine the requested particle number.
Finally, this procedure allows us to calculate the experimentally relevant column density

$$n(x,y,T) = \int_{-\infty}^{\infty}\mathrm{d}z\, n(\boldsymbol{x},T) \tag{4.62}$$

and the line density in x-direction

$$n(x,T) = \int_{-\infty}^{\infty}\mathrm{d}y\int_{-\infty}^{\infty}\mathrm{d}z\, n(\boldsymbol{x},T) \tag{4.63}$$

as well as in y-direction

$$n(y,T) = \int_{-\infty}^{\infty}\mathrm{d}x\int_{-\infty}^{\infty}\mathrm{d}z\, n(\boldsymbol{x},T) \tag{4.64}$$

for a given temperature numerically.

Due to the numerical evaluation of the self-consistency, we can show the behaviour of the order parameter as function of space and temperature in Figure 4.6. In the center of the trap, we see the expected behaviour from the homogeneous case, which has already been illustrated in Figure 3.7: For higher temperatures the order parameter decreases. Additionally, we conclude that the radius where the order parameter vanishes, decreases for higher temperatures, whereas in the zero-temperature limit, the radius, where the order parameter vanishes, is equal to the Thomas-Fermi radius, as we have already seen in Figure 4.3.

As it has been motivated in the introduction of the order parameter, it has a descriptive meaning: The case $\Delta = 0$ is equal to the ideal Fermi gas, whereas $\Delta \neq 0$ denotes the superfluid case. Consequently for temperatures $T < T_\mathrm{C}$, the superfluid regime can only be found at the center of the density cloud, while the peripheral areas behave like an ideal Fermi gas. Since the superfluidity is caused by the presence of Cooper pairs, we can conclude that they are concentrated in the inner part of the trap.

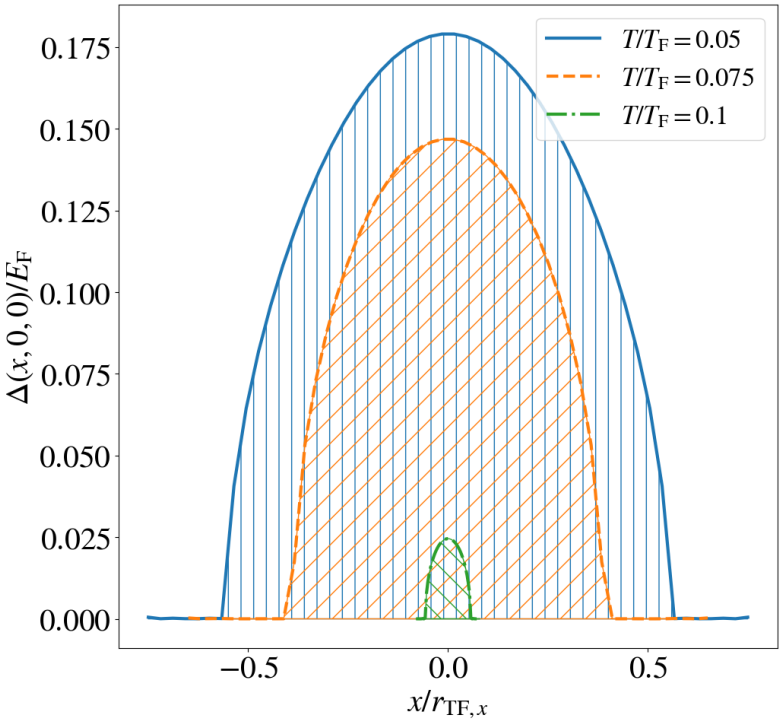

Figure 4.6.: Illustration of the order parameter as function of temperature and space from the self-consistency equations (4.57) and (4.58). Similar to the homogeneous case shown in Figure 3.6, we see the decreasing of the order parameter for higher temperatures. Additionally, the radius, where the order parameter vanishes, decreases for higher temperatures.

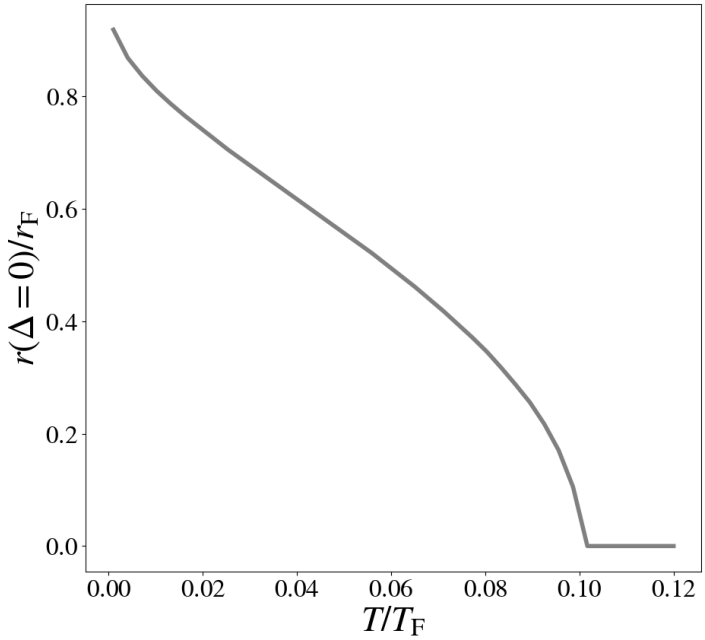

Figure 4.7.: Numerical evaluation of the radius, where the order parameter vanishes as function of the temperature. For $T > T_C$ the order parameter vanishes completely.

5. Comparison Theory with Experiment

We motivated our previous theoretical investigations on the basis of the corresponding ^{6}Li experiment. Considering the BCS regime of the experiment, which is characterised by small negative s-wave scattering lengths $a_s < 0$. The mean-field approach is valid for $1/a_s k_F < -0.5$, as we have seen in Figure 1.3. Therefore, we compare the theoretically expected behaviour versus the experimental data by restricting us to this regime.

5.1. Experimental Data

In the experiment, the particle-number density is measured due to destructive absorption imaging [60]. This leads to a particle-number density, which is integrated in z-direction, and is denoted as column density. Performing another spatial integration in either x- or y-direction leads to a corresponding line density. Both quantities are shown in Figure 5.1. The data is taken from ten runs of the experiment with a corresponding Gaussian fit.

Especially, in this chapter we focus on experimental data for the s-wave scattering length of $a_s = -4510\ a_0$, where a_0 describes the Bohr radius. The choice was made because of two issues: On one hand, the critical temperature needs to be as high as possible in order to reach superfluidity, but on the other hand large s-wave scattering lengths lead to stronger interactions, where our theory breaks down. In order to justify our choice, Figure 5.2 shows $1/a_s k_F$ as function of particle number and s-wave scattering length. There we can see that the s-wave scattering length of $a_s = -4510\ a_0$ leads to $1/a_s k_F < -0.5$ for the experimentally relevant particle numbers between $N = 10^5$ and $N = 10^6$. According to the explanations above, we can apply our theory for this s-wave scattering length.

In view of the possible occurrence of superfluidity, it is important to determine the temperature from the experimental data. In our theoretical investigation, the interaction strength is characterised by the dimensionless quantity $1/a_s k_F$ and the critical temperature is calculated in units of the Fermi temperature. This leads directly to another important quantity namely the particle number. Experimentally, the measurement of the particle number by destructive absorption imaging is quite difficult. Therefore, our theory should provide clues how to determine temperature and particle number as the two key quantities.

Dealing with the particle number and trapping frequencies from the experimental measurement shown in Figure 5.1, the relevant parameters are the particle number $N = 982998$ with the trapping frequencies $\omega_x = 2\pi\times498$ Hz, $\omega_x = 2\pi\times25$ Hz and $\omega_x = 2\pi\times340$ Hz. The s-wave scattering length $a_s = -4510\ a_0$ yields the dimensionless parameter $1/a_s k_F = -0.8$. For all these values, we obtain for the critical temperature at the center of the trap according to (3.55) the value $T_C = 0.18 T_F$. These parameters will be used in the following for our theoretical investigations.

A key point of our theoretical approach for modelling the experiment was the introduction of LDA. In the following, we prove at first empirically the validity of LDA from the experimental data.

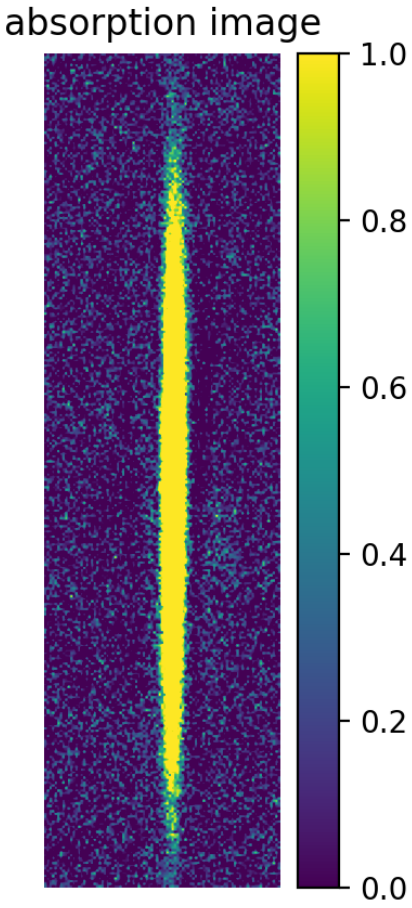

(a) 2D column density.

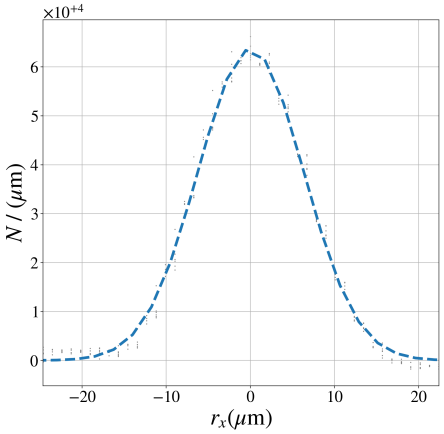

(b) 1D line density in x-direction.

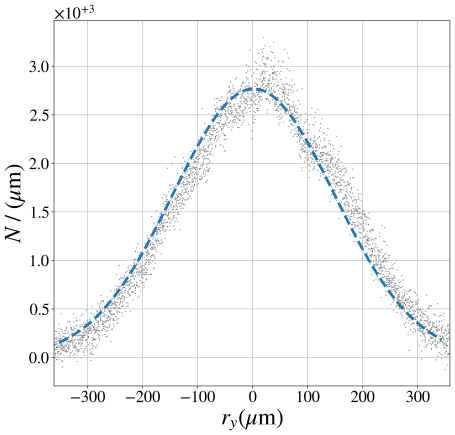

(c) 1D line density in y-direction.

Figure 5.1.: Experimental results for power $P = 100$ mW corresponding to $N = 982998 \pm 32420$ ^{6}Li atoms, magnetic field $B = 977.4$ G leads to s-wave scattering length $a_s = -4510\ a_0$, trapping frequencies are $\omega_x = 2\pi \times 498$ Hz, $\omega_y = 2\pi \times 25$ Hz and $\omega_z = 2\pi \times 340$ Hz. Panel **(a)** shows the column density scaled in units of the maximum. An additional integration of the line density leads directly to the line density in x-direction **(b)** and y-direction **(c)**. The blue curve shows the Gaussian fit of the experimental data.

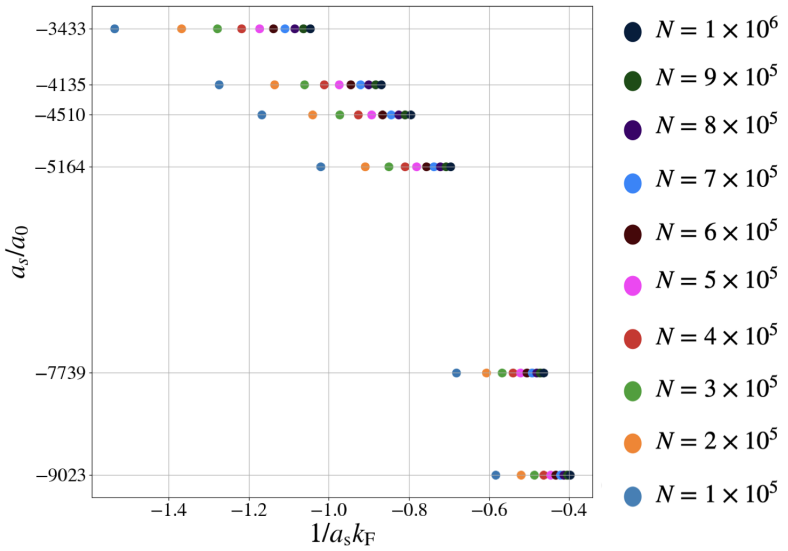

Figure 5.2.: Experimentally accessible s-wave scattering lengths a_s as function of the dimensionless parameter $1/a_s k_F$. The range of particle numbers between 10^5 and 10^6 is chosen so that it corresponds to typical values of the experiment.

5.2. Check of LDA

Regarding above column density from the experiment shown in Figure 5.1, the width of the particle cloud is a directly accessible quantity. According to the local-density approximation, the ratio between x- and y-direction depends only on the trapping frequencies. This will be derived analytically for the ideal Fermi gas.
Generally, the width of the column-density is described by the second moment of the distribution [61]. For the ideal Fermi gas, we start with the particle-number density (4.34) and derive the second moment by performing two spatial integrations. To this end, we start with the line density in x-direction (4.46) and y-direction (4.47) both represented by the appropriate polylogarithmic function (C.1). Proceeding with another spatial integration over the left direction, we obtain finally for the second moment

$$\langle x^2 \rangle = \int_{-\infty}^{\infty} \mathrm{d}x\, x^2 n(x) = -\frac{2}{M\beta^4(\tilde{\omega}\hbar)^3\omega_x^2}\mathrm{Li}_4\left(-e^{\beta\mu}\right), \tag{5.1}$$

$$\langle y^2 \rangle = \int_{-\infty}^{\infty} \mathrm{d}x\, y^2 n(y) = -\frac{2}{M\beta^4(\tilde{\omega}\hbar)^3\omega_y^2}\mathrm{Li}_4\left(-e^{\beta\mu}\right). \tag{5.2}$$

Thus, the ratio between the individual directions is given by

$$\sqrt{\frac{\langle x^2 \rangle}{\langle y^2 \rangle}} = \frac{\omega_y}{\omega_x}. \tag{5.3}$$

The second moments of the experimental results arise in an analogous way from the line density, which have been represented in Figure 5.1 next to the column density.
Therefore, comparing the theoretical results (5.3) with the experimental ones, gives a first impression about the validity of our theory. From Figure 5.3, it follows that the expected relationship between the widths of the particle-number density is also experimentally observable. This can be concluded from the maximum deviation given by 19.7 %. The average deviation amounts to 11.6 %.
Even if here for the theoretical approach in first approximation the ideal Fermi gas is assumed to motivate the ratio between the moments in x- and y-direction, this can be

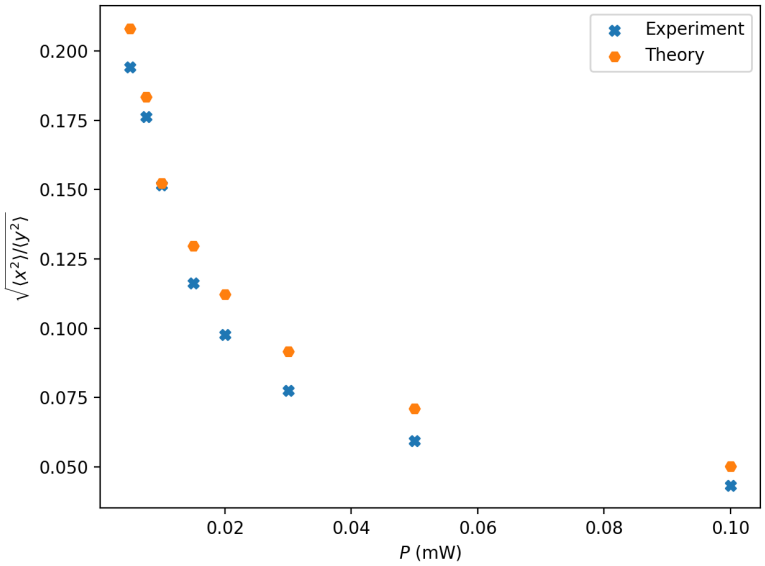

Figure 5.3.: Ratio between second moments. Theoretically we expect that this is equal to the inverse of the ratio of the trapping frequencies according to (5.3).

generalised to the superfluid Fermi gas. Regarding the symmetry considerations of the previous chapter for the particle-number density, where we mapped the ellipsoidal particle cloud in Cartesian coordinates to spherical coordinates, the ratio between the individual directions is also given by the trapping frequencies.

Since we have confirmed empirically the correctness of using LDA now, we proceed and calculate the theoretical results according to the experimental parameters.
To this end, we start with the ideal Fermi gas, to get a first feeling for the influence of the temperature, since the temperature is generally unknown. Thus, we are not sure at all if we are even close to the superfluid regime.

5.3. Ideal Fermi Gas

In the previous chapter, we introduced polylogarithmic functions to represent both the column (4.45) and the line densities (4.46)–(4.47) of the ideal Fermi gas. To determine both quantities, the chemical potential needs to be calculated from the corresponding particle-number equation (4.43).
Concerning the relation to the experiment, we can analyse theoretically the impact of the particle number for a fixed temperature as well as the influence of the temperature for a fixed particle number. Therefore, we start with a fixed particle number given by the experimental measurement and investigate the resulting temperature dependence.

5.3.1. Temperature Dependence

To get a general overview, we choose arbitrarily two temperatures, namely $T = 0.05\ T_\mathrm{F}$ and $T = 0.2\ T_\mathrm{F}$. These two values lead to the observation that higher temperatures flatten the curve, as we see in Figure 5.4. The maximum value in the center of the trapping decreases, whereas further out, both the column density and line densities increase. Consequently, the Thomas-Fermi radius increases. This behaviour can be seen in the 2D column density, as well as in the 1D line density.

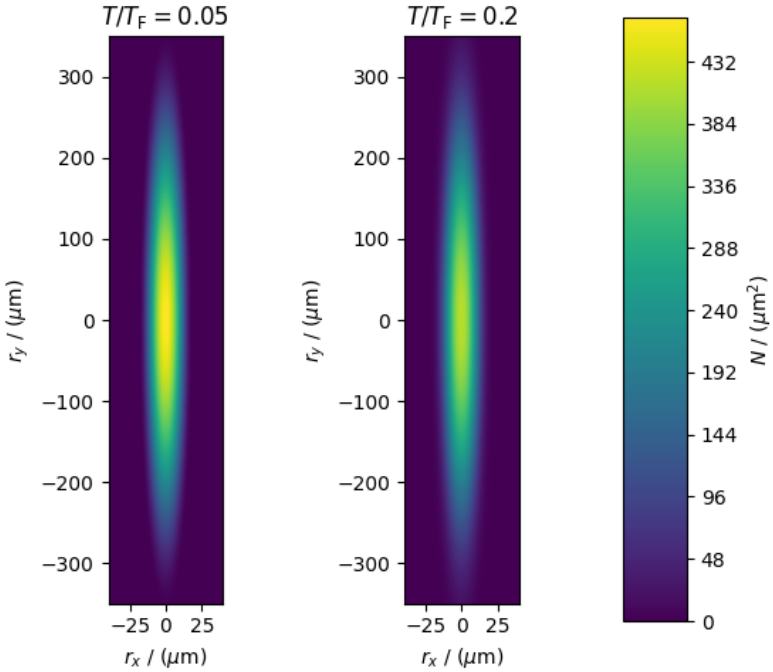

(a) 2D column density.

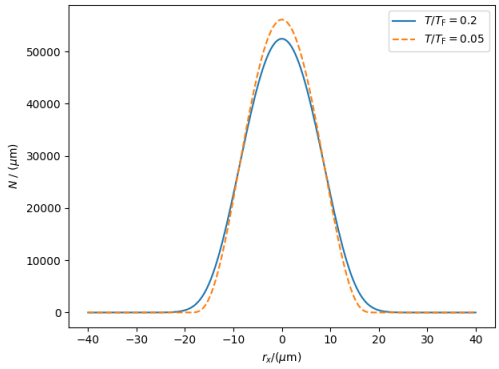

(b) 1D line density in x-direction.

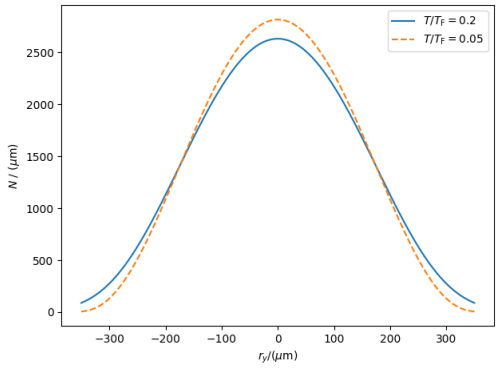

(c) 1D line density in y-direction.

Figure 5.4.: Plot of the ideal Fermi gas determined by a particle number of $N = 982998$, trapping frequencies $\omega_x = 2\pi \times 498$ Hz, $\omega_y = 2\pi \times 25$ Hz and $\omega_z = 2\pi \times 340$ Hz. Panel **(a)** shows the single-integrated column density. An additional integration leads again to the line-density in x-direction **(b)** and y-direction **(c)**. To get a first impression for the impact of the temperature, we choose two exemplary values.

After we analysed the impact of the temperature on the column density and the line density, we consider the influence of the particle number.

5.3.2. Particle-Number Dependence

We proceed similar to the previous subsection. However, this time, we consider a fixed temperature $T = 0.2\ T_\mathrm{F}$, which is slightly above the critical temperature $T_\mathrm{C} = 0.18 T_\mathrm{F}$ for the chosen parameters, and analyse a variation of the particle number within the standard deviation

$$N = 982998 \pm 32429 \tag{5.4}$$

following from the experimental data in Figure 5.1. In Figure 5.5, we conclude that increasing the particle number primarily affects the center of the trap, because here the corresponding densities increase noticeably due to higher particle numbers.

Since we have seen the general impact of temperature and particle number regarding the ideal Fermi gas, the question arises how these results agree with the experimental data. In addition, we determine the order parameter in the superfluid regime to discuss its influence on the particle-number densities. Comparing these results with the ideal Fermi gas and the experimental data gives rise to a first qualitative discussion.

5.4. Superfluid Fermi Gas

After we investigated the ideal Fermi gas, we discuss now the impact of superfluidity. Regarding temperatures below the critical temperature (4.48), we have to solve both equations for the order parameter (4.57) and the particle number (4.60) self-consistently, as it has been described in the previous chapter. The difference between superfluid and ideal Fermi gas becomes obvious in Figure 5.6 in y- and in Figure 5.7 in x-direction: For temperatures below T_C, the line density is compressed in the superfluid case. Thus, the maximum value in the center of the trap increases, whereas the width becomes narrower. Furthermore, we can benchmark our numerics for solving the self-consistency equations (4.57), (4.60) here. In the limiting case $T \to T_\mathrm{C}$ both the plot of the ideal Fermi gas and the superfluid Fermi gas overlap.

Concerning a quantitative comparison to the experiment, two problems arise. First, the data for the experimental line density scatter strongly. Therefore the small differences between the theoretical results for various temperatures cannot be explicitly read off. Additionally the measured line density is shifted visibly to the right due to an experimental misalignment. This means that the maximum value is not reached in the center of the trap, which becomes especially obvious in the y-direction. Due to those reasons, the temperature cannot be specified concretely.
Furthermore, there is a large deviation between the experimental data and our theoretical results in x-direction shown in Figure 5.7 for all temperatures. This gives rise to the assumption that the particle number may not correspond to the experimentally measured one.

To set up a quantitative comparison regarding the deviation between experimental data and our theoretical approach, further measurements are necessary. However, the Figures 5.6 and 5.7 show that our theoretical results agree at least qualitatively with the experimental results.

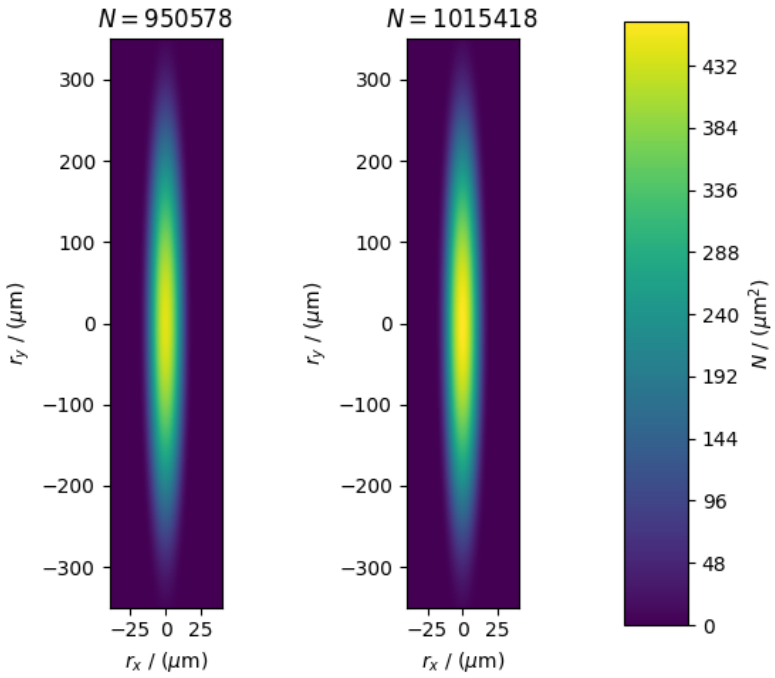

(a) 2D column density.

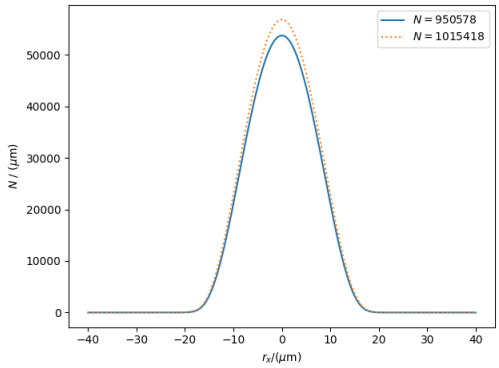

(b) 1D line density in x-direction.

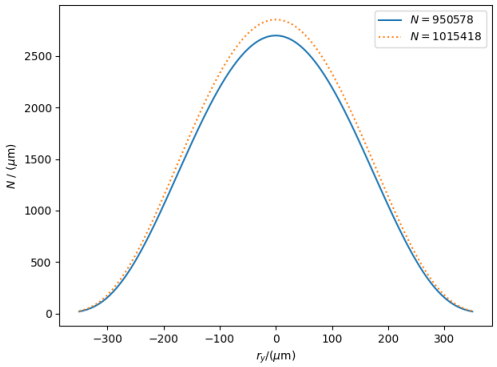

(c) 1D line density in y-direction.

Figure 5.5.: Behaviour of the ideal Fermi gas for the trapping frequencies $\omega_x = 2\pi \times 498$ Hz, $\omega_y = 2\pi \times 25$ Hz and $\omega_z = 2\pi \times 340$ Hz. Panel **(a)** shows the single-integrated column density. An additional integration leads to the line-density in x-direction **(b)** and y-direction **(c)**. The variation of the particle number leads primarily to an increase of the density in the trapping center. The temperature is $T = 0.2T_\mathrm{F}$ and thus above the critical temperature $T_\mathrm{C} = 0.18\ T_\mathrm{F}$.

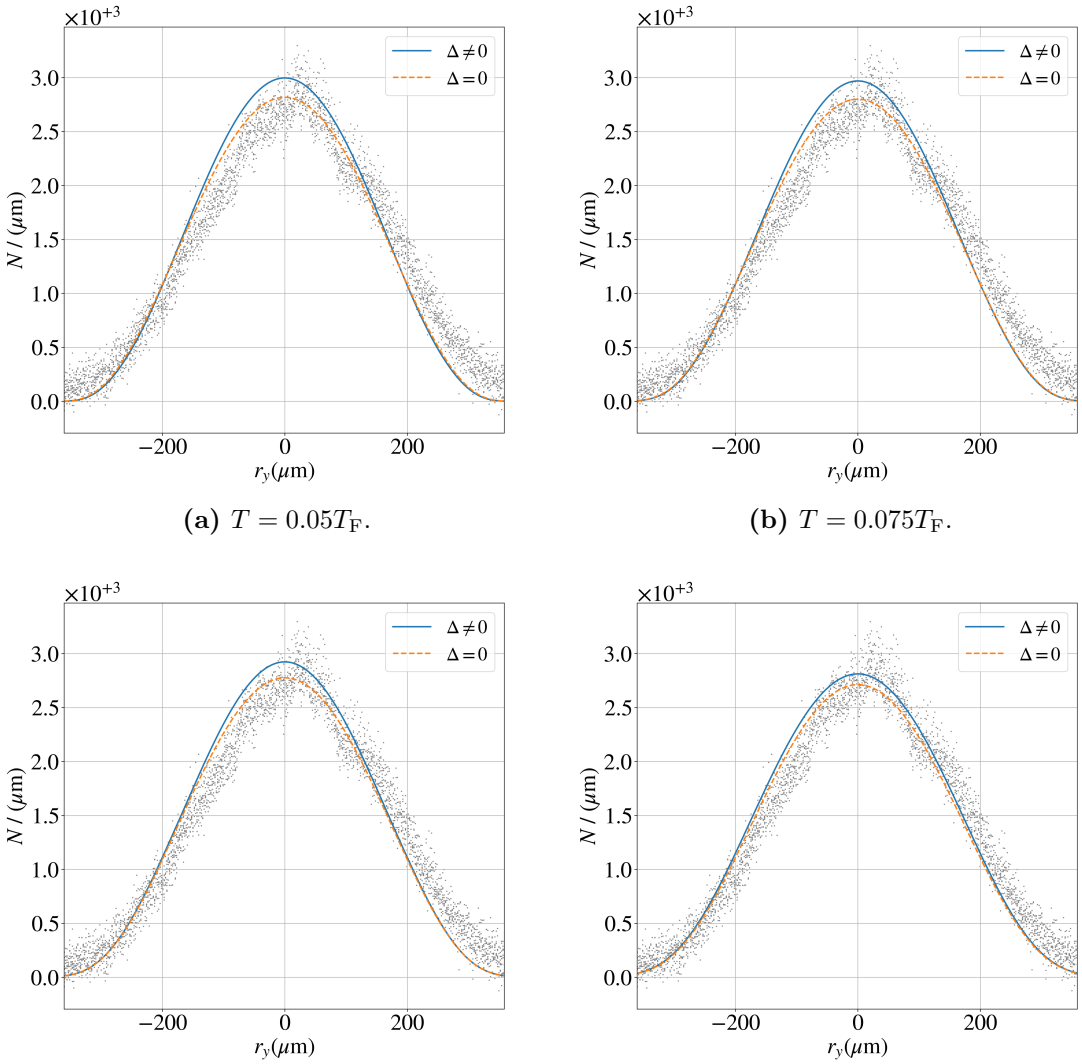

(a) $T = 0.05T_{\mathrm{F}}$.

(b) $T = 0.075T_{\mathrm{F}}$.

(c) $T = 0.1T_{\mathrm{F}}$.

(d) $T = 0.18T_{\mathrm{F}}$.

Figure 5.6.: Comparison between superfluid and ideal Fermi gas with the experimental data in y-direction. The parameters for the theoretical approaches are given by $N = 982998$, trapping frequencies $\omega_x = 2\pi \times 498$ Hz, $\omega_y = 2\pi \times 25$ Hz and $\omega_z = 2\pi \times 340$ Hz. Panel **(a)**, **(b)** and **(c)** show the behaviour in the superfluid regime. **(d)** shows the behaviour in the limiting case $T \to T_{\mathrm{C}} = 0.18\ T_{\mathrm{F}}$.

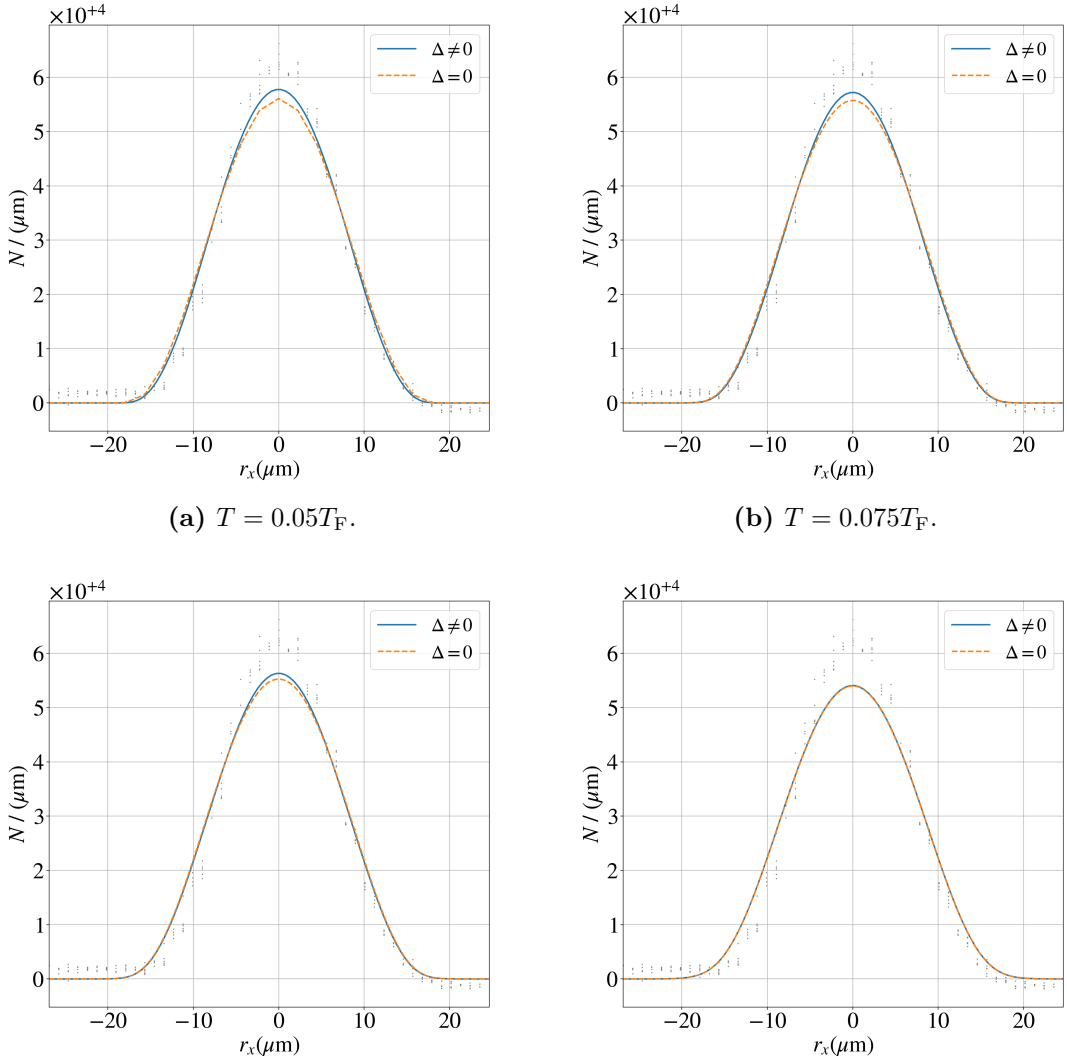

(a) $T = 0.05T_{\mathrm{F}}$.

(b) $T = 0.075T_{\mathrm{F}}$.

(c) $T = 0.1T_{\mathrm{F}}$.

(d) $T = 0.15T_{\mathrm{F}}$.

Figure 5.7.: Comparison between superfluid and ideal Fermi gas with the experimental data in x-direction. The parameters for the theoretical approaches are given by $N = 982998$, trapping frequencies $\omega_x = 2\pi \times 498$ Hz, $\omega_y = 2\pi \times 25$ Hz and $\omega_z = 2\pi \times 340$ Hz. Panel **(a)**, **(b)** and **(c)** show the behaviour in the superfluid regime. **(d)** shows the behaviour in the limiting case $T \to T_{\mathrm{C}} = 0.18\ T_{\mathrm{F}}$.

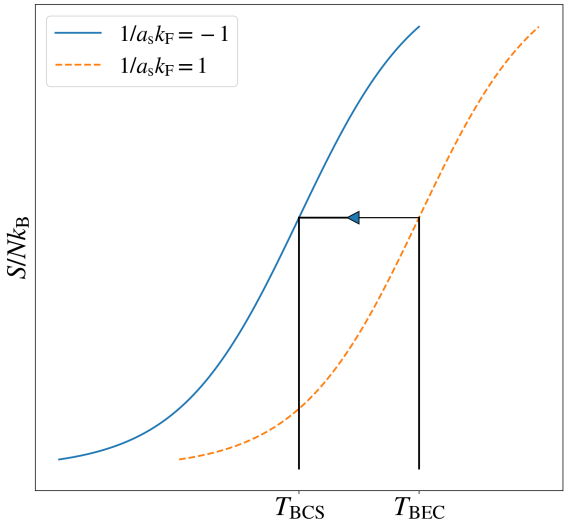

Figure 5.8.: Schematic representation of adiabatic ramping. To this end, the entropy per atom is shown as function of temperature for two different values of $1/a_s k_F$, where $1/a_s k_F = -1$ is in the BCS regime and $1/a_s k_F = 1$ is located in the BEC limit.

5.5. Adiabatic Sweeps

Above we have suggested a direct thermometry in the BCS-limit, which is based on measuring the column density and comparing the obtained data with our mean-field theory. In contrast to that in the literature a temperature measurement has so far been suggested in an indirect way in form of an adiabatic sweep thermometry [62, 63]. The underlying procedure is motivated in Figure 5.8, where the theoretical result for the entropy per atom is schematically shown for two values of the parameter $1/a_s k_F$, one in the BCS and one in the BEC regime. The underlying idea is to change the s-wave scattering length via a Feshbach resonance with an isentropic sweep from the BCS to the BEC regime. Measuring the shape of the profile of the trapped cloud at the BEC regime then allows to determine its temperature T_{BCS}. In the deep BEC limit, $^6Li_2$ molecules behave like an ideal Bose, for which the temperature can be determined theoretically. However, this limiting case is difficult to reach experimentally, therefore the temperature dependence of an interacting Bose gas based on a Hartee-Fock approach can be taken into account [64]. Afterwards, Figure 5.8 allows to reconstruct from the known entropy the corresponding temperature T_{BCS}.

The success of the adiabatic sweep thermometry relies on two major requirements. On the one hand, it is necessary that the dependence of the entropy from temperature and interaction strength is known theoretically for the whole BEC-BCS crossover. Only then one could obtain the entropy gauge curves from Figure 5.8, which are at the heart of this indirect thermometry method. Furthermore, by performing a control sweep back from the BEC- to the BCS-limit it is important to control experimentally that the cloud properties were only changed in a reversible way. Otherwise the basic assumption for using the theoretical gauge curves from Figure 5.8 would break down.

6. Conclusion

Inspired by the BCS-BEC crossover experiment at TU Kaiserslautern [30], we searched for a thermometer in the BCS limit. The temperature is an important quantity to study reliably the superfluidity of the Fermi gas. Up to now the only possibility to measure the temperature is given by ramping adiabatically into the BEC limit [62, 63]. Another difficulty is the determination of the particle number [60]. For this purpose, we set up a theory that allows us to study the behaviour of the Fermi gas in the BCS limit, where we investigate the impact of temperature and particle number. To this end, we simulate both experimental parameters in our theoretical considerations.

Starting with a many-body Hamilton operator for the description of the interacting ^{6}Li atoms (2.1), we take into account only the Bogoliubov channel to derive a mean-field Hamilton operator (2.6) in order to solve approximately the initial problem. Considering this mean-field approach, the order parameter for superfluidity is introduced in (2.7). This allows the determination between the superfluid phase of the Fermi gas for $\Delta \neq 0$ and the ideal Fermi gas for $\Delta = 0$. The perturbative expansion of the free energy up to the mean-field level in combination with the principle of minimal sensitivity leads directly to the equation for the order parameter (2.47). Additionally, since we are dealing with the grand-canonical ensemble, we obtain a second equation for the particle number (2.46). These two equations represent the two self-consistency equations in accordance with [17], which we analyse during this thesis.

First, we consider the homogeneous Fermi gas in the limiting case $T \to 0$ and derive analytic expressions for the order parameter (3.36) and the chemical potential (3.37), which has already been shown in [52, 53]. However, since we are interested in a thermometer for ^{6}Li, the impact of temperature is studied numerically for the order parameter in Figure 3.6 and for the chemical potential in Figure 3.7. In particular, these two figures highlight the importance of the critical temperature. In the zero-temperature limit an analytical expression for the critical temperature is obtained in (3.57), which we compare with the numerical result in Figure 3.8. Generally, we see an exponential increasing of the critical temperature as function of the scattering length.

In order to set up a theory for the experiment, the harmonic trapping potential needs to be considered in our theoretical considerations. Therefore, we take into account the local-density approximation (LDA) and introduce the spatially dependent chemical potential (4.2). Starting with the limiting case of an ideal Fermi gas for temperatures above the critical temperature, the particle number is fixed by the chemical potential and we obtain expressions for the column (4.45) and line densities (4.46)–(4.47), which are both represented by polylogarithmic functions (C.1) depending on chemical potential and temperature, as it has been derived by [65]. Regarding the superfluid regime, both self-consistency equations are solved numerically. Consequently, the spatial dependence of the order parameter is shown in Figure 4.6.

The theoretical considerations of the previous chapter allow us finally to compare our theory with the experimental data. First, we point out empirically that the experimental results follow the expectations according to the local-density approximation. Studying

the impact of temperature and particle number on the ideal Fermi gas theoretically, we show the column density and line densities in Figure 5.4 for different temperatures and in Figure 5.5 for a variation of the particle number. At last, we compare the theoretical behaviour with the experimentally measured line densities in y-direction in Figure 5.6 and in x-direction in Figure 5.7 and conclude that our theoretical results agree with the experimental data qualitatively. Thus, we obtain a direct thermometer for the temperature measurement in the BCS limit. However, the experimental data cannot be evaluated quantitatively. The fluctuations within a series of measurements, as well as difficulties in determining the particle number make it impossible to specify the temperature. Nevertheless, the theoretical results provide the possibility, based on the known adiabatic sweeping [62, 63], to determine the temperature in the BCS limit due to the corresponding temperature in the BEC limit. Applying this temperature to our theory allows a comparison between the theoretical result and the measured column density, thus providing further certainty regarding the estimation of the particle number. Furthermore, this gives further certainty regarding the estimation of the particle number.

7. Outlook

Based on the mean-field approach in chapter 2, we briefly point out open questions that provide grounds for further theoretical investigations

7.1. Higher-Order Corrections

Considering the initial Figure 1.3, we have seen that the pink curve corresponds to the numerical results of our mean-field theory for the critical temperature, which we calculated in chapter 3 in (3.55). In the BEC limit, the mean-field critical temperature diverges. We are looking for a theoretical approach to describe the complete BCS-BEC crossover. Considering Gaussian fluctuations, the total BCS-BEC crossover has been analysed theoretically, as we can see by the example of the blue curve in the above mentioned Figure [35, 36, 66].

Regarding the expansion of the partition function (A.33), we expect that higher-order corrections lead to the Gaussian fluctuations in the cumulant expansion of the free energy (A.42). Thus, we anticipate that the considerations of this thesis can be generalised to the whole BCS-BEC crossover. Since the complete crossover is already experimentally realised [30], this extension of our theory provides further insights for the interpretation of the experimental data. In particular, for obtaining the entropy gauge curve in Figure 5.8 in the adiabatic sweep thermometry it is indispensable to have the theoretical access to the full BCS-BEC crossover.

7.2. Superfluidity

In the introduction, we motivated the BCS-BEC crossover based on the occurring superfluidity. In this context, we can determine the superfluidity in the BCS regime by adding a boost term to our initial mean-field Hamiltonian (2.6)

$$\hat{H}_{\mathrm{Boost}} = \hat{H}_{\mathrm{MF}} + \sum_{\sigma} \int \mathrm{d}^3 x \hat{\psi}_{\sigma}^{\dagger}(\boldsymbol{x}) \frac{\hbar}{i} \nabla \hat{\psi}_{\sigma}(\boldsymbol{x}) \boldsymbol{u} \tag{7.1}$$

with the corresponding boost velocity $\boldsymbol{u}$ and the first quantised momentum $\frac{\hbar}{i}\nabla$ [67]. The meaning of the boost term can be interpreted physically: If we boost the superfluid Fermi gas with a velocity $\boldsymbol{u}$, only the normal fluid proportion of the Fermi gas will be dragged along. However, the superfluid part remains in its initial position. This allows us to calculate the superfluid density. The partial derivative with respect to the boost velocity $\boldsymbol{u}$ of the mean-field free energy for the boosted Hamiltonian (7.1) yields the proportion of particles, which are dragged along by the boost. Consequently, these are the fermions that are in the normal fluid state. Considering the normal fluid particles per volume, we obtain the normal fluid density. The superfluid density follows directly, since the total particle-number density consists only of these two parts.

Furthermore, based on this consideration Landau's critical velocity v_{c} for superfluidity can be determined along the BCS-BEC crossover [68].

7.3. Dirty Fermion Problem

In 1959 P. Anderson suggested localisation effects in superconductors [69], which are caused by impurities or defects in the lattice. In the ultracold regime this followed the idea of Bose and Anderson glasses, which was proposed in 2003 by the use of laser speckle potentials [70]. In this context Anderson localisation occurs for non-interacting bosons and Bose glasses for interacting bosons. The improvement of experimental techniques allowed finally J. Billy et al. and G. Roati et al. to realise Anderson localisation of matter waves in ultracold atoms [71–73].

Based on the dirty boson problem [74,75], the effect of disorder was studied experimentally and theoretically on the BEC side of the crossover in the corresponding ^{6}Li experiment [45]. For this purpose, the impact of a laser speckle potential on the column density was investigated. This consideration can also be studied in the BCS side of the crossover. Therefore, we need to add the corresponding disorder potential to our mean-field Hamiltonian (2.6). From this, the disordered column density on the BCS side can be obtained. In this context, we expect based on Anderson's theorem [69] that the order parameter for superfluidity is less influenced by the disorder potential in the BCS regime compared to the BEC limit, where the theorem no longer applies and thus the order parameter for superfluidity is reduced by disorder [53].

A. Beyond Mean-Field Theory

In order to go beyond the mean-field result of the free energy (2.13), we introduce the interaction picture, which is also known as the Dirac picture. The main idea of this approach is to split the system in the Hamilton operator in the Schrödinger picture into two parts

$$\hat{H} = \hat{H}_{\mathrm{MF}} + \left(\hat{H} - \hat{H}_{\mathrm{MF}}\right), \tag{A.1}$$

where the first part denotes the mean-field result, whose solution has already been calculated in chapter 2 and the second part is the higher-order correction, generally denoted in the interaction picture as the perturbation. To simplify the notation and emphasize its character as a perturbation, we perform the substitution

$$\hat{V} \equiv \hat{H} - \hat{H}_{\mathrm{MF}}. \tag{A.2}$$

For our case, this consideration is justified, since we assumed that $\hat{H} - \hat{H}_{\mathrm{MF}}$ denotes a small perturbation of the mean-field Hamilton operator. In the following, we elaborate the connections between the Schrödinger and the Dirac picture to benefit from these properties for the evaluation of the partition function, which will guide us directly to the free energy.

A.1. Dirac Picture

Let $|\psi_S(t)\rangle$ be the solution of the Schrödinger equation

$$i\hbar\frac{\partial}{\partial t}|\psi_S(t)\rangle = \hat{H}|\psi_S(t)\rangle \tag{A.3}$$

in the Schrödinger picture. For our investigations we benefit from the Wick rotation $t \to -i\tau$ of the Schrödinger equation [50] and thus obtain

$$-\hbar\frac{\partial}{\partial \tau}|\psi_S(\tau)\rangle = \hat{H}|\psi_S(\tau)\rangle. \tag{A.4}$$

The time-evolution operator $\hat{U}(\tau, \tau')$ for the Wick rotated frame connects states at different times τ and τ'

$$|\psi_S(\tau)\rangle = \hat{U}(\tau, \tau')|\psi_S(\tau')\rangle \tag{A.5}$$

and is given by

$$\hat{U}(\tau, \tau') = e^{-(\tau-\tau')\hat{H}/\hbar}. \tag{A.6}$$

The inverse is given by swapping τ and τ'

$$\hat{U}^{-1}(\tau, \tau') = e^{(\tau-\tau')\hat{H}/\hbar} = \hat{U}(\tau', \tau). \tag{A.7}$$

The substantial idea of the interaction picture is that the time evolution is performed perturbatively. To this end we can relate a state in the Schrödinger picture with the corresponding one in the Dirac picture by

$$|\psi_D(\tau)\rangle = e^{\hat{H}_{\mathrm{MF}}t/\hbar}|\psi_S(\tau)\rangle \quad \Leftrightarrow \quad |\psi_S(\tau)\rangle = e^{-\hat{H}_{\mathrm{MF}}t/\hbar}|\psi_D(\tau)\rangle. \tag{A.8}$$

Consequently, taking into account an arbitrary operator $\hat{O}_D(\tau)$ in the Dirac picture, the following relation to an operator in the Schrödinger picture has to be fulfilled

$$\langle\psi_D(\tau)|\hat{O}_D(\tau)|\psi_D(\tau)\rangle = \langle\psi_S(\tau)|\hat{O}_S|\psi_S(\tau)\rangle. \tag{A.9}$$

It states that the expectation value of any observable must be independent from the choice of the picture. Thus, the relation (A.8) leads to the determination of the operator in the Dirac picture for the Wick rotated frame

$$\hat{O}_D(\tau) = e^{\hat{H}_{\mathrm{MF}}\tau/\hbar}\hat{O}_S e^{-\hat{H}_{\mathrm{MF}}\tau/\hbar}. \tag{A.10}$$

Starting from the equation of motion of the state vector in the Schrödinger picture following from (A.1), (A.2) and (A.4)

$$-\hbar\frac{\partial}{\partial\tau}|\psi_S(\tau)\rangle = \left(\hat{H}_{\mathrm{MF}} + \hat{V}\right)|\psi_S(\tau)\rangle, \tag{A.11}$$

we use once more (A.8) to derive the equation of motion in the Dirac picture

$$-\hbar\frac{\partial}{\partial\tau}|\psi_D(\tau)\rangle = e^{\hat{H}_{\mathrm{MF}}\tau/\hbar}\left[-\hbar\frac{\partial}{\partial\tau}|\psi_S(\tau)\rangle + \hat{H}_{\mathrm{MF}}|\psi_S(\tau)\rangle\right] = e^{\hat{H}_{\mathrm{MF}}\tau/\hbar}\hat{V}|\psi_S(\tau)\rangle. \tag{A.12}$$

Inserting (A.12) in (A.8) thus leads finally to the Tomonaga-Schwinger equation [50]

$$-\hbar\frac{\partial}{\partial\tau}|\psi_D(\tau)\rangle = \hat{V}_D(\tau)|\psi_D(\tau)\rangle \tag{A.13}$$

with the interaction part of the Hamiltonian in the Dirac picture

$$\hat{V}_D(\tau) = e^{\hat{H}_{\mathrm{MF}}\tau/\hbar}\hat{V}e^{-\hat{H}_{\mathrm{MF}}\tau/\hbar}. \tag{A.14}$$

Similarly, we transform the time-evolution operator (A.6) into the interaction picture according to (A.8)

$$\hat{U}_D(\tau,\tau') = e^{-\hat{H}_{\mathrm{MF}}\tau}e^{\hat{H}(\tau-\tau')}e^{\hat{H}_{\mathrm{MF}}\tau'}. \tag{A.15}$$

In the next step, we investigate the time-dependence of this time-evolution operator. Differentiating (A.15) with respect to τ yields due to (A.10):

$$-\hbar\frac{\partial}{\partial\tau}\hat{U}_D(\tau,\tau_0) = \hat{V}_D(\tau)\hat{U}_D(\tau,\tau_0). \tag{A.16}$$

Since this is a partial differential equation of first order, it can formally be solved by a simple integration

$$\hat{U}_D(\tau,\tau_0) = 1 + \frac{-1}{\hbar}\int_{\tau_0}^{\tau}\mathrm{d}\tau_1\hat{V}_D(\tau_1)\hat{U}_D(\tau_1,\tau_0) \tag{A.17}$$

under the assumption of the initial value $\hat{U}_D(\tau_0,\tau_0) = 1$. This procedure has to be repeated iteratively, which leads to an infinite sum

$$\begin{aligned}\hat{U}_D(\tau,\tau_0) = 1 &+ \frac{-1}{\hbar}\int_{\tau_0}^{\tau}\mathrm{d}\tau_1\hat{V}_D(\tau_1) + \left(\frac{-1}{\hbar}\right)^2\int_{\tau_0}^{\tau}\mathrm{d}\tau_1\int_{\tau_0}^{\tau_1}\mathrm{d}\tau_2\hat{V}_D(\tau_1)\hat{V}_D(\tau_2) + \dots \\ &+ \left(\frac{-1}{\hbar}\right)^n\int_{\tau_0}^{\tau}\mathrm{d}\tau_1\int_{\tau_0}^{\tau_1}\mathrm{d}\tau_2\cdots\int_{\tau_0}^{\tau_{n-1}}\mathrm{d}\tau_n\hat{V}_D(\tau_1)\hat{V}_D(\tau_2)\dots\hat{V}_D(\tau_n) + \dots\end{aligned} \tag{A.18}$$

that is generally known as Dyson series. Truncating the Dyson series after a finite number of terms leads to perturbative results.
For a general operator in the Dirac picture $\hat{O}_D(\tau)$, we obtain due to (A.10) the equation of motion in the Dirac picture

$$-\hbar\frac{\partial}{\partial\tau}\hat{O}_D(\tau) = \left[\hat{O}_D(\tau), \hat{H}_{\mathrm{MF}}\right]_- . \tag{A.19}$$

From this, we can conclude that the dynamics of an operator in the Dirac picture is determined by the free part of the Hamilton operator, whereas the dynamics of the state vector follows from the perturbative part of the Hamiltonian (A.13).

Next, we will investigate the behaviour of the Bogoliubov transformed operators in the interaction picture, which have already been introduced for the diagonalisation of the mean-field Hamiltonian (2.25)–(2.26).

A.2. Fermionic Operators

For the derivation of the perturbative expansion of the free energy, we consider the fermionic field operators in the Schrödinger picture, which were introduced in chapter 2 by a Bogoliubov transformation $\hat{\alpha}_{\boldsymbol{k}}$, $\hat{\alpha}^\dagger_{\boldsymbol{k}}$, $\hat{\beta}_{\boldsymbol{k}}$ and $\hat{\beta}^\dagger_{\boldsymbol{k}}$. Since they are represented in the Schrödinger picture, they are time-independent. On the basis of the interaction picture (A.8), we can introduce new time-dependent Bogoliubov operators $\hat{\alpha}_D(\boldsymbol{k},\tau)$, $\hat{\alpha}^\dagger_D(\boldsymbol{k},\tau)$, $\hat{\beta}_D(\boldsymbol{k},\tau)$, $\hat{\beta}^\dagger_D(\boldsymbol{k},\tau)$. Their time dependence is determined by the equation of motion (A.19)

$$-\hbar\frac{\partial}{\partial\tau}\hat{\alpha}_D(\boldsymbol{k},\tau) = \left[\hat{\alpha}_D(\boldsymbol{k},\tau), \hat{H}_{\mathrm{MF}}\right]_- = E(\boldsymbol{k})\hat{\alpha}_D(\boldsymbol{k},\tau), \tag{A.20}$$

$$-\hbar\frac{\partial}{\partial\tau}\hat{\alpha}^\dagger_D(\boldsymbol{k},\tau) = \left[\hat{\alpha}^\dagger_D(\boldsymbol{k},\tau), \hat{H}_{\mathrm{MF}}\right]_- = -E(\boldsymbol{k})\hat{\alpha}^\dagger_D(\boldsymbol{k},\tau), \tag{A.21}$$

$$-\hbar\frac{\partial}{\partial\tau}\hat{\beta}_D(\boldsymbol{k},\tau) = \left[\hat{\beta}_D(\boldsymbol{k},\tau), \hat{H}_{\mathrm{MF}}\right]_- = E(\boldsymbol{k})\hat{\beta}_D(\boldsymbol{k},\tau), \tag{A.22}$$

$$-\hbar\frac{\partial}{\partial\tau}\hat{\beta}^\dagger_D(\boldsymbol{k},\tau) = \left[\hat{\beta}^\dagger_D(\boldsymbol{k},\tau), \hat{H}_{\mathrm{MF}}\right]_- = -E(\boldsymbol{k})\hat{\beta}^\dagger_D(\boldsymbol{k},\tau). \tag{A.23}$$

Here $E(\boldsymbol{k})$ denotes the Bogoliubov dispersion (2.37). The commutators in these equations of motion can be evaluated with the help of

$$\left[\hat{A}, \hat{B}\hat{C}\right] = \left\{\hat{A}, \hat{B}\right\}\hat{C} - \hat{B}\left\{\hat{A}, \hat{C}\right\} \tag{A.24}$$

for arbitrary operators $\hat{A}$, $\hat{B}$ and $\hat{C}$, which enables us to calculate the commutators with the known anti-commutator relations of the Bogoliubov operators (2.27)–(2.29). Solving these simple first-order differential equations (A.20)–(A.23) with the initial condition that the initial value is equal to the corresponding time-independent operator in the Schrödinger picture, we obtain

$$\hat{\alpha}_D(\boldsymbol{k},\tau) = e^{-E(\boldsymbol{k})\tau/\hbar}\hat{\alpha}_{\boldsymbol{k}}, \quad \hat{\beta}_D(\boldsymbol{k},\tau) = e^{-E(\boldsymbol{k})\tau/\hbar}\hat{\beta}_{\boldsymbol{k}} \tag{A.25}$$

$$\hat{\alpha}^\dagger_D(\boldsymbol{k},\tau) = e^{E(\boldsymbol{k})\tau/\hbar}\hat{\alpha}^\dagger_{\boldsymbol{k}}, \quad \hat{\beta}^\dagger_D(\boldsymbol{k},\tau) = e^{E(\boldsymbol{k})\tau/\hbar}\hat{\beta}^\dagger_{\boldsymbol{k}} \tag{A.26}$$

for the Bogoliubov rotated operators in the Dirac picture. In particular, it follows directly that the equal-time anti-commutator relations in the Dirac picture coincide with those in

the Schrödinger picture (2.27)–(2.29):

$$\left\{\hat{\alpha}_D(\boldsymbol{k},\tau),\hat{\beta}_D^\dagger(\boldsymbol{k}',\tau)\right\} = \left\{\hat{\alpha}_D^\dagger(\boldsymbol{k},\tau),\hat{\beta}_D(\boldsymbol{k}',\tau)\right\} = 0, \tag{A.27}$$

$$\left\{\hat{\alpha}_D(\boldsymbol{k},\tau),\hat{\beta}_D(\boldsymbol{k}',\tau)\right\} = \left\{\hat{\alpha}_D^\dagger(\boldsymbol{k},\tau),\hat{\beta}_D^\dagger(\boldsymbol{k}',\tau)\right\} = 0, \tag{A.28}$$

$$\left\{\hat{\alpha}_D(\boldsymbol{k},\tau),\hat{\alpha}_D^\dagger(\boldsymbol{k}',\tau)\right\} = \left\{\hat{\beta}_D(\boldsymbol{k},\tau),\hat{\beta}_D^\dagger(\boldsymbol{k}',\tau)\right\} = \delta_{\boldsymbol{k}\boldsymbol{k}'}. \tag{A.29}$$

Consequently, at a specific time τ the fermionic operators in momentum space $\hat{\alpha}_D(\boldsymbol{k},\tau)$, $\hat{\beta}_D(\boldsymbol{k},\tau)$, $\hat{\alpha}_D^\dagger(\boldsymbol{k},\tau)$ and $\hat{\beta}_D^\dagger(\boldsymbol{k},\tau)$ annihilate and create a Bogoliubov quasi particle with momentum $\boldsymbol{k}$.

A.3. Partition Function

This allows us to consider the partition function (2.9)

$$Z = \mathrm{Tr}\left\{e^{-\beta\hat{H}}\right\} = \mathrm{Tr}\left\{e^{-\beta(\hat{H}_{\mathrm{MF}}+\hat{H}-\hat{H}_{\mathrm{MF}})}\right\}, \tag{A.30}$$

where we introduced the solvable mean-field Hamiltonian (2.6). A simple rewriting of the partition function (A.30) yields

$$Z = \mathrm{Tr}\left\{e^{-\beta\hat{H}_{\mathrm{MF}}}e^{\hbar\beta\hat{H}_{\mathrm{MF}}/\hbar}e^{-(\hbar\beta-0)\hat{H}/\hbar}\right\}. \tag{A.31}$$

Comparing this result with the time-evolution operator in the interaction picture (A.15), we obtain finally

$$Z = \mathrm{Tr}\left\{e^{-\beta\hat{H}_{\mathrm{MF}}}\hat{U}_D(\hbar\beta,0)\right\}. \tag{A.32}$$

Thus, we can plug in the Dyson-Series (A.18) into the partition function (A.32)

$$Z = \mathrm{Tr}\left\{e^{-\beta\hat{H}_{\mathrm{MF}}}\left[1+\frac{-1}{\hbar}\int_0^{\hbar\beta}\mathrm{d}\tau\hat{V}_D(\tau)+\left(\frac{-1}{\hbar}\right)^2\int_0^{\hbar\beta}\mathrm{d}\tau_1\int_0^{\tau_1}\mathrm{d}\tau_2\hat{V}_D(\tau_1)\hat{V}_D(\tau_2)+\ldots\right]\right\}. \tag{A.33}$$

In zeroth order truncation of the Dyson series, we obtain the mean-field approximation

$$Z_{\mathrm{MF}} = \mathrm{Tr}\left\{e^{-\beta\hat{H}_{\mathrm{MF}}}\right\}. \tag{A.34}$$

The difference between the original Hamilton operator (2.1) and the mean-field Hamilton operator (2.6) reads

$$\hat{V} = \hat{H}-\hat{H}_{\mathrm{MF}} = \int\mathrm{d}^3x\Big\{g\,\hat{\psi}_\uparrow^\dagger(\boldsymbol{x})\hat{\psi}_\downarrow^\dagger(\boldsymbol{x})\hat{\psi}_\downarrow(\boldsymbol{x})\hat{\psi}_\uparrow(\boldsymbol{x}) - \Delta^*\hat{\psi}_\downarrow(\boldsymbol{x})\hat{\psi}_\uparrow(\boldsymbol{x}) - \Delta\hat{\psi}_\uparrow^\dagger(\boldsymbol{x})\hat{\psi}_\downarrow^\dagger(\boldsymbol{x})+\frac{\Delta^*\Delta}{g}\Big\} \tag{A.35}$$

leading to

$$\hat{V}_D(\tau) = \int\mathrm{d}^3x\Big\{g\,\hat{\psi}_\uparrow^\dagger(\boldsymbol{x},\tau)\hat{\psi}_\downarrow^\dagger(\boldsymbol{x},\tau)\hat{\psi}_\downarrow(\boldsymbol{x},\tau)\hat{\psi}_\uparrow(\boldsymbol{x},\tau) - \Delta^*\hat{\psi}_\downarrow(\boldsymbol{x},\tau)\hat{\psi}_\uparrow(\boldsymbol{x},\tau) - \Delta\hat{\psi}_\uparrow^\dagger(\boldsymbol{x},\tau)\hat{\psi}_\downarrow^\dagger(\boldsymbol{x},\tau)+\frac{\Delta^*\Delta}{g}\Big\} \tag{A.36}$$

in the interaction picture. The second quantised operators in real space occurring here are directly linked with above operators (A.25),(A.26) in the interaction picture: Performing a Fourier transformation of the operators in interaction picture analogous to (2.19), (2.20)

$$\hat{\psi}_\sigma(\boldsymbol{x},\tau) = \frac{1}{\sqrt{V}}\sum_{\boldsymbol{k}} e^{i\boldsymbol{k}\boldsymbol{x}}\hat{a}_{\boldsymbol{k},\sigma}(\tau), \quad \hat{a}_{\boldsymbol{k},\sigma}(\tau) = \frac{1}{\sqrt{V}}\int \mathrm{d}^3x e^{-i\boldsymbol{k}\boldsymbol{x}}\hat{\psi}_\sigma(\boldsymbol{x},\tau) \tag{A.37}$$

$$\hat{\psi}^\dagger_\sigma(\boldsymbol{x},\tau) = \frac{1}{\sqrt{V}}\sum_{\boldsymbol{k}} e^{-i\boldsymbol{k}\boldsymbol{x}}\hat{a}^\dagger_{\boldsymbol{k},\sigma}(\tau), \quad \hat{a}^\dagger_{\boldsymbol{k},\sigma}(\tau) = \frac{1}{\sqrt{V}}\int \mathrm{d}^3x e^{i\boldsymbol{k}\boldsymbol{x}}\hat{\psi}^\dagger_\sigma(\boldsymbol{x},\tau), \tag{A.38}$$

followed by a Bogoliubov transformation according to (2.25),(2.26)

$$\hat{\alpha}_{\boldsymbol{k}}(\tau) = u_{\boldsymbol{k}}(\tau)\hat{a}_{\boldsymbol{k}\uparrow}(\tau) - v_{\boldsymbol{k}}(\tau)\hat{a}^\dagger_{-\boldsymbol{k}\downarrow}(\tau), \quad \hat{\alpha}^\dagger_{\boldsymbol{k}}(\tau) = u^*_{\boldsymbol{k}}(\tau)\hat{a}^\dagger_{\boldsymbol{k}\uparrow}(\tau) - v^*_{\boldsymbol{k}}(\tau)\hat{a}_{-\boldsymbol{k}\downarrow}(\tau), \tag{A.39}$$

$$\hat{\beta}_{\boldsymbol{k}}(\tau) = u_{\boldsymbol{k}}(\tau)\hat{a}_{-\boldsymbol{k}\downarrow}(\tau) + v_{\boldsymbol{k}}(\tau)\hat{a}^\dagger_{\boldsymbol{k}\downarrow}(\tau), \quad \hat{\beta}^\dagger_{\boldsymbol{k}}(\tau) = u^*_{\boldsymbol{k}}(\tau)\hat{a}^\dagger_{-\boldsymbol{k}\downarrow}(\tau) + v^*_{\boldsymbol{k}}(\tau)\hat{a}_{\boldsymbol{k}\uparrow}(\tau) \tag{A.40}$$

represent the perturbation $\hat{V}$ in the interaction picture $\hat{V}_D(\tau)$. Therefore, higher-order corrections of the partition function can be calculated on the basis of (A.33) using the equal-time commutation relations (A.27)–(A.29).

The free energy follows directly from the partition function

$$F = -\frac{1}{\beta}\ln Z. \tag{A.41}$$

Higher-order corrections to the mean-field free energy

$$F = F_{\mathrm{MF}} + \langle \hat{H} - \hat{H}_{\mathrm{MF}}\rangle_{\mathrm{MF}} - \frac{\beta}{2}\left[\langle\left(\hat{H} - \hat{H}_{\mathrm{MF}}\right)^2\rangle_{\mathrm{MF}} - \left(\langle \hat{H} - \hat{H}_{\mathrm{MF}}\rangle_{\mathrm{MF}}\right)^2\right] + \cdots \tag{A.42}$$

follow from the perturbative results of the partition function (A.33)

$$F_{\mathrm{MF}} = -\frac{1}{\beta}\ln Z_{\mathrm{MF}}. \tag{A.43}$$

According to Figure 1.3 the mean-field free energy (A.43) leads to the pink curve, which represents the mean-field critical temperature as it is shown in chapter 3. The second-order correction of the free energy (A.42) corresponds to the Gaussian fluctuations treated in the literature, which lead to the blue curve of the critical temperature in Figure 1.3.

B. Supplements for Homogeneous Fermi Gas

In this chapter, we represent additional material to the evaluation of the homogeneous Fermi gas in the third chapter. For the zero-temperature limit, we considered elliptic functions, whose properties will be analysed here in more detail. Additionally, we show the derivation of the approximation for the critical temperature T_C in (3.57).

B.1. Elliptic Functions

Generally elliptic integrals owe their name the descriptive meaning that they occur in the calculation of the circumference of ellipses, as well as the surface area of ellipsoids [76]. The elliptic integrals can be divided into three different types

$$\int \frac{\mathrm{d}t}{\sqrt{(1-t^2)(1-k^2t^2)}}, \quad \int \mathrm{d}t \frac{\sqrt{1-k^2t^2}}{\sqrt{1-t^2}}, \quad \int \frac{\mathrm{d}t}{(1-nt^2)\sqrt{(1-x^2)(1-k^2x^2)}} \tag{B.1}$$

denoted as first-, second- and third-kind, which are represented in the Legendre normal form [77]. These three integrals can be transferred to the normal trigonometric forms

$$\int \frac{\mathrm{d}\theta}{\sqrt{1-k^2\sin^2\theta}}, \quad \int \mathrm{d}\theta \sqrt{1-k^2\sin^2\theta}, \quad \int \frac{\mathrm{d}\theta}{(1-n\sin^2\theta)\sqrt{1-k^2\sin^2\theta}} \tag{B.2}$$

with the substitution $t = \sin\theta$. In the following, we focus on the first- and second-kind of elliptic integrals, since we benefit from their properties in the course of this thesis.

The elliptic functions are called incomplete for a range of integration from 0 to y, where $0 < y < 1$. The case $y = 1$ denotes complete ellitptic integrals. Incomplete elliptic integral of first kind is given by

$$F(\phi, k) = \int_0^\phi \frac{\mathrm{d}\theta}{\sqrt{1-k^2\sin^2\theta}} = \int_0^x \frac{\mathrm{d}t}{\sqrt{(1-t^2)(1-k^2t^2)}}. \tag{B.3}$$

The incomplete elliptic integral of second kind is represented by

$$E(\phi, k) = \int_0^\phi \mathrm{d}\theta \sqrt{1-k^2\sin\theta} = \int_0^x \mathrm{d}t \frac{\sqrt{1-k^2t^2}}{\sqrt{1-t^2}} \tag{B.4}$$

For our investigations the complete case of the elliptic integral of first

$$K(k) = \int_0^{\frac{\pi}{2}} \frac{\mathrm{d}\theta}{\sqrt{1-k^2\sin^2\theta}} = \int_0^1 \frac{\mathrm{d}t}{\sqrt{(1-t^2)(1-k^2t^2)}}, \tag{B.5}$$

and second kind

$$E(k) = \int_0^{\frac{\pi}{2}} \mathrm{d}\theta \sqrt{1-k^2\sin\theta} = \int_0^1 \mathrm{d}t \frac{\sqrt{1-k^2t^2}}{\sqrt{1-t^2}} \tag{B.6}$$

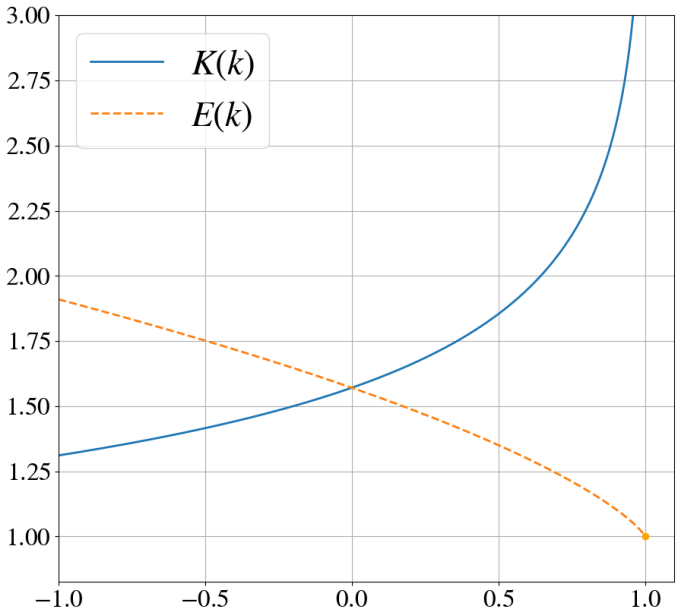

Figure B.1.: Plots of the complete elliptic integrals of first- (B.5) and second-kind (B.6).

is of major interest. The two complete elliptic integrals can be expressed both in terms of a power series, which are given by

$$K(k) = \frac{\pi}{2} \sum_{n=0}^{\infty} \left(\frac{(2n)!}{2^{2n}(n!)^2} \right)^2 k^{2n} \tag{B.7}$$

for the first kind, as well as

$$E(k) = \frac{\pi}{2} \sum_{n=0}^{\infty} \left(\frac{(2n)!}{2^{2n}(n!)^2} \right)^2 \frac{k^{2n}}{1-2n} \tag{B.8}$$

for the second kind. In view of a numerical evaluation, the power series are significantly inferior to the integrals. However, considering limiting cases, the series expansion can be taken into account up to a reasonable order and thus provides a perturbative approach. In addition to the complete elliptic integrals, complementary elliptic integrals

$$\mathrm{K}(k) \equiv \mathrm{K}'(k') \tag{B.9}$$

and

$$\mathrm{E}(k) \equiv \mathrm{E}'(k') \tag{B.10}$$

depending on the complementary parameter

$$k' = \sqrt{1-k^2}. \tag{B.11}$$

Exemplary to get a rough feeling for the shape of the complete elliptic integrals of first and second kind, they are plotted on the interval from -1 to 1 in Fig. B.1. Especially, we detect for the first-kind elliptic integral a pole for $\lim_{k\to 1} K(k)$.

B.2. Derivation of Critical Temperature Approximation

In the third chapter, we discussed the impact of the temperature on the Fermi gas. In this context, the critical temperature was proven to be of major interest. Below the critical temperature T_C, the superfluid Fermi gas occurs in the BCS-BEC crossover. Since, we consider the BCS mean-field theory, we are able to determine superfluidity at the BCS side of the crossover. The derivation of an approximative formula is quite technical, which is shown in this section. We start with the equation for the order parameter (3.6) and set the order parameter $\Delta = 0$. In the limiting case $\Delta \to 0$, the temperature T converges to the critical temperature T_C. Consequently, this equation

$$\frac{M}{2\pi\hbar^2 a_\mathrm{s}} = \int \frac{\mathrm{d}^3k}{(2\pi)^3}\left[\frac{1}{E(\boldsymbol{k})} - \frac{\tanh\left(\frac{E(\boldsymbol{k})-E_\mathrm{F}}{2k_\mathrm{B}T_\mathrm{C}}\right)}{E(\boldsymbol{k})-E_\mathrm{F}}\right] \tag{B.12}$$

has to be fulfilled. Analogously, to the beginning of the third chapter (3.8), we transform the $\boldsymbol{k}$-integral to an energy integral

$$\frac{M}{2\pi\hbar^2 a_\mathrm{s}} = \frac{2}{\sqrt{\pi}}\left(\frac{M}{2\pi\hbar^2}\right)^{\frac{3}{2}}\int_0^\infty \mathrm{d}\varepsilon\sqrt{\varepsilon}\left[\frac{1}{\varepsilon} - \frac{\tanh\left(\frac{\varepsilon-E_\mathrm{F}}{2k_\mathrm{B}T_\mathrm{C}}\right)}{\varepsilon-E_\mathrm{F}}\right]. \tag{B.13}$$

Since we start to investigate the integral quite detailed, we manipulate the energy integral as follows

$$\begin{aligned} I &\equiv \int_0^\infty \mathrm{d}\varepsilon\sqrt{\varepsilon}\left[\frac{1}{\varepsilon} - \frac{\tanh\left(\frac{\varepsilon-E_\mathrm{F}}{2k_\mathrm{B}T_\mathrm{C}}\right)}{\varepsilon-E_\mathrm{F}}\right] \\ &= \int_0^\infty \mathrm{d}\varepsilon\sqrt{\varepsilon}\left[\frac{1}{\varepsilon} - \frac{1}{\varepsilon}\tanh\left(\frac{\varepsilon-E_\mathrm{F}}{2k_\mathrm{B}T_\mathrm{C}}\right) + \frac{1}{\varepsilon}\tanh\left(\frac{\varepsilon-E_\mathrm{F}}{2k_\mathrm{B}T_\mathrm{C}}\right) - \frac{1}{\varepsilon-E_\mathrm{F}}\tanh\left(\frac{\varepsilon-E_\mathrm{F}}{2k_\mathrm{B}T_\mathrm{C}}\right)\right]. \end{aligned} \tag{B.14}$$

Performing a partial integration leads to

$$I = \int_0^\infty \mathrm{d}\varepsilon \frac{1}{4k_\mathrm{B}T_\mathrm{C}} \frac{1}{\cosh^2\left(\frac{\varepsilon-E_\mathrm{F}}{2k_\mathrm{B}T_\mathrm{C}}\right)}\left[4\sqrt{\varepsilon} - 2\sqrt{E_\mathrm{F}}\ln\left|\frac{\sqrt{\varepsilon}+\sqrt{E_\mathrm{F}}}{\sqrt{\varepsilon}-\sqrt{E_\mathrm{F}}}\right|\right]. \tag{B.15}$$

The evaluation of this expression has to be performed in several steps. First of all, we consider the Dirac delta function as the following limiting case for very low temperatures

$$\lim_{T_\mathrm{C}\downarrow 0} \frac{1}{4k_\mathrm{B}T_\mathrm{C}} \frac{1}{\cosh^2\left(\frac{\varepsilon-E_\mathrm{F}}{2k_\mathrm{B}T_\mathrm{C}}\right)} = \delta(\varepsilon - E_\mathrm{F}). \tag{B.16}$$

This follows from the integral

$$\int_{-\infty}^\infty \mathrm{d}x\left\{\lim_{\epsilon\to 0}\left[\frac{1}{2\epsilon}\frac{1}{\cosh\left(\frac{x}{\epsilon}\right)}\right]\right\} = 1 \tag{B.17}$$

and the limiting case

$$\lim_{\epsilon\to 0}\left[\frac{1}{2\epsilon}\frac{1}{\cosh^2\left(\frac{x}{\epsilon}\right)}\right] = \begin{cases}\infty, & x = 0\\ 0, & x \neq 0\end{cases}, \tag{B.18}$$

since this agrees with the definition of the Dirac-delta function. Thus, the energy integral yields

$$\frac{\pi}{2a_\mathrm{s}k_\mathrm{F}} = 2 - \int_0^\infty \mathrm{d}\varepsilon \frac{1}{4k_\mathrm{B}T_\mathrm{C}} \frac{1}{\cosh^2\left(\frac{\varepsilon-E_\mathrm{F}}{2k_\mathrm{B}T_\mathrm{C}}\right)} \ln\left|\frac{\sqrt{\varepsilon}+\sqrt{E_\mathrm{F}}}{\sqrt{\varepsilon}-\sqrt{E_\mathrm{F}}}\right|. \tag{B.19}$$

Analysing the remaining logarithmic function

$$\frac{\sqrt{\varepsilon}+\sqrt{E_\mathrm{F}}}{\sqrt{\varepsilon}-\sqrt{E_\mathrm{F}}} = \frac{(\sqrt{\varepsilon}+\sqrt{E_\mathrm{F}})^2}{\varepsilon - E_\mathrm{F}} = \frac{\left(\sqrt{\frac{\varepsilon}{2k_\mathrm{B}T_\mathrm{C}}}+\sqrt{\frac{E_\mathrm{F}}{2k_\mathrm{B}T_\mathrm{C}}}\right)^2}{\frac{\varepsilon}{2k_\mathrm{B}T_\mathrm{C}}-\frac{E_\mathrm{F}}{2k_\mathrm{B}T_\mathrm{C}}} \tag{B.20}$$

yields a convergent term in the numerator, while the denominator requires a deeper investigation due to the singularity for $\varepsilon \to E_\mathrm{F}$. However, we can split the fraction in the logarithm and evaluate the numerator separately by taking into account (B.16)

$$\begin{aligned}\int_0^\infty \mathrm{d}\varepsilon \frac{1}{4k_\mathrm{B}T_\mathrm{C}} \frac{1}{\cosh^2\left(\frac{\varepsilon-E_\mathrm{F}}{2k_\mathrm{B}T_\mathrm{C}}\right)} \ln\frac{\left(\sqrt{\varepsilon}+\sqrt{E_\mathrm{F}}\right)^2}{2k_\mathrm{B}T_\mathrm{C}} &\approx \int_0^\infty \mathrm{d}\varepsilon\, \delta(\varepsilon - E_\mathrm{F}) \ln\frac{\left(\sqrt{\varepsilon}+\sqrt{E_\mathrm{F}}\right)^2}{2k_\mathrm{B}T_\mathrm{C}} \\ &= \ln\frac{4E_\mathrm{F}}{2k_\mathrm{B}T_\mathrm{C}}. \end{aligned} \tag{B.21}$$

Thus, we obtain from (B.19)

$$\frac{\pi}{2a_\mathrm{s}k_\mathrm{F}} = 2 - \ln\frac{4E_\mathrm{F}}{2k_\mathrm{B}T_\mathrm{C}} + \int_0^\infty \mathrm{d}\varepsilon \frac{1}{4k_\mathrm{B}T_\mathrm{C}} \frac{1}{\cosh^2\left(\frac{\varepsilon-E_\mathrm{F}}{2k_\mathrm{B}T_\mathrm{C}}\right)} \ln\frac{|\varepsilon - E_\mathrm{F}|}{2k_\mathrm{B}T_\mathrm{C}}. \tag{B.22}$$

In the last step, we investigate the remaining integral for the present special case

$$E_F >> k_\mathrm{B}T_\mathrm{C} \tag{B.23}$$

and derive finally the desired analytic expression for the critical temperature

$$T_\mathrm{C} = \frac{8}{\pi}\frac{\gamma}{e^2} T_\mathrm{F} \exp\left(\frac{\pi}{2a_\mathrm{s}k_\mathrm{F}}\right) \tag{B.24}$$

with $\gamma = e^C$ where C denotes Euler's constant, which has been also calculated in [35].

C. Polylogarithmic Function

To investigate an ideal Fermi gas in a harmonic trapping potential, we introduced polylogarithmic functions. Therefore a more detailed look at those polylogarithmic function is appropriate. A general definition is given by the power series [78]

$$\mathrm{Li}_s(z) = \sum_{k=1}^{\infty} \frac{z^k}{k^s} \tag{C.1}$$

for $|z| < 1$. Considering the cases $s = 0$ and $s = 1$, we can represent them by analytic expressions

$$\mathrm{Li}_0(z) = \frac{z}{1-z}, \tag{C.2}$$

$$\mathrm{Li}_1(z) = -\log(1-z). \tag{C.3}$$

C.1. Analytic Continuation

Taking into account the case $n \in \mathbb{N}_0$, the recursive relation

$$\mathrm{Li}_n(z) = \int_0^z \frac{\mathrm{Li}_{n-1}(t)}{t} \mathrm{d}t \tag{C.4}$$

can be introduced. Comparing (C.3) and (C.4), we can expand our relation to the case $|z| > 1$ for $n \in \mathbb{N}$, if we assume $z < 0$.

The assumption $z < 0$ is fulfilled in the fermionic case, as we have already seen in the particle-number equation for the ideal Fermi gas (4.43). For comparative purposes we investigated the behavior of the polylogarithmic function for different n in Figure C.1.

C.2. Numerical Evaluation

For numerical purposes it is of interest to keep the calculation effort as low as possible. Consequently, it is important to use the most simple representation of the polylogarithmic function. A generalisation of the polylogarithmic function is known by the generalized Nielsen polylogarithmic function [79]

$$S_{n,p}(z) = \frac{(-1)^{n+p-1}}{(n-1)!p!} \int_0^1 \log^{n-1}(t) \frac{\log^p(1-zt)}{t} \mathrm{d}t, \tag{C.5}$$

which has the special case

$$\mathrm{Li}_n(z) = S_{n-1,1}(z) \tag{C.6}$$

and consequently, we can use the integral representation above for the numerical evaluation of the polylogarithmic function.

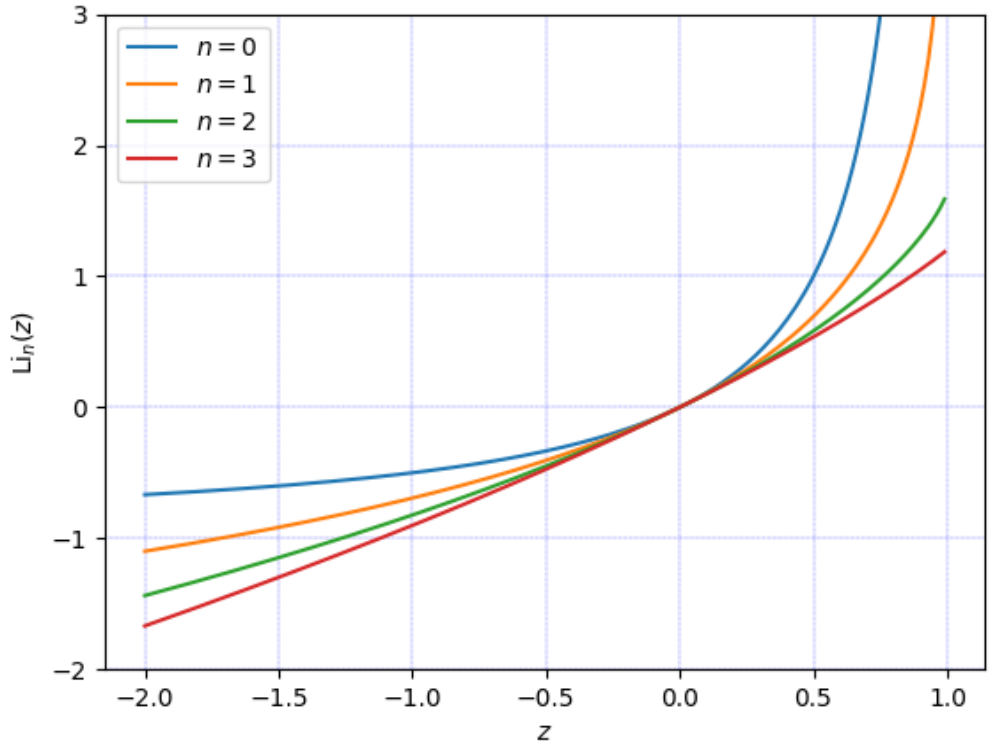

Figure C.1.: Illustration of the polylogarithmic function (C.3) continued by the recursion relation (C.4) for $n > 1$. We can see the analytic continuation for $z < -1$.

Bibliography

[1] D. Lee. *The extraordinary phases of liquid 3He. Rev. Mod. Phys.*, **69**, 645 (1997).

[2] R. Laughlin. *Nobel lecture: Fractional quantization. Rev. Mod. Phys.*, **71**, 863 (1999).

[3] W. Ketterle. *Nobel Lecture: When atoms behave as waves: Bose-Einstein condensation and the atom laser. Rev. Mod. Phys.*, **3**, 736 (2002).

[4] A. Abrikosov. *Nobel Lecture: Type-II superconductors and the vortex lattice. Rev. Mod. Phys.*, **76**, 975 (2004).

[5] P. Grünberg. *Nobel lecture: From spin waves to giant magnetoresistance and beyond. Rev. Mod. Phys.*, **80**, 1531 (2008).

[6] F. Haldane. *Nobel lecture: Topological quantum matter. Rev. Mod. Phys.*, **89**, 1 (2017).

[7] K. Kopitzki and P. Herzog. *Einführung in die Festkörperphysik*. Springer, Berlin, 7th edition (2015).

[8] W. Meissner and R. Ochsenfeld. *Ein neuer Effekt bei Eintritt der Supraleitfähigkeit. Die Naturwissenschaften*, **21**, 787 (1933).

[9] L. N. Cooper. *Bound electron pairs in a degenerate Fermi gas. Phys. Rev.*, **104**, 1189 (1956).

[10] J. Bardeen, L. Cooper, and J. Schrieffer. *Microscopic Theory of Superconductivity. Phys. Rev.*, **106**, 162 (1957).

[11] J. Schrieffer. *Macroscopic quantum phenomena from pairing in superconductors. Phys. Tod.*, **26**, 23 (1973).

[12] A. Einstein. *Plancks Gesetz und Lichtquantenhypothese. Zeitschrift für Physik*, **26**, 178 (1924).

[13] A. Einstein. *Quantentheorie des einatomigen idealen Gases - Zweite Abhandlung. Sitzungsberichte der Preussischen Akademie der Wissenschaften*, pages 3–10 (1925).

[14] J. Allen and A. Misener. *Flow Phenomena in Liquid Helium II. Nature*, **142**, 411 (1938).

[15] P. Kapitsa. *Viscosity of liquid helium below the lambda-point. Nature*, **141**, 74 (1938).

[16] F. London. *The lambda-Phenomenon of Liquid Helium and the Bose-Einstein Degeneracy. Nature*, **141**, 643 (1938).

[17] L. Pitaevskii and S. Stringari. *Bose-Einstein Condensation and Superfluidity (International Series of Monographs on Physics)*. Oxford Science Publications, Oxford, 2nd edition (2015).

[18] L. Landau and E. Lifshitz. *Lehrbuch der theoretischen Physik V, Statistische Mechanik*. Akademie Verlag, Berlin, 4th edition (1975).

[19] D. Osheroff, R. Richardson, and D. Lee. *Evidence for a New Phase of Solid 3He. Phys. Rev. Lett.*, **28**, 885 (1972).

[20] W. Pauli. *Über den Zusammenhang des Abschlusses der Elektronengruppen im Atom mit der Komplexstruktur der Spektren. Zeitschrift für Physik*, **31**, 765 (1925).

[21] W. Phillips. *Laser cooling and trapping of neutral atoms. Rev. Mod. Phys.*, **70**, 721 (1998).

[22] C. Pethick and H. Smith. *Bose-Einstein Condensation in Dilute Gases.* Cambridge University Press, Cambridge, 2nd edition (2008).

[23] R. P. Feynman. *Simulating Physics with Computers. Int. J. Theor. Phys.*, **21**, 467 (1982).

[24] I. Bloch, J. Dalibard, and S. Nascimbène. *Quantum simulations with ultracold quantum gases. Nature*, **8**, 267 (2012).

[25] M. Greiner, C. A. Regal, and D. S. Jin. *Emergence of a molecular Bose-Einstein condensate from a Fermi gas. Nature*, **426**, 537 (2003).

[26] M. W. Zwierlein, C. A. Stan, C. H. Schunck, S. M. Raupach, S. Gupta, Z. Hadzibabic, and W. Ketterle. *Observation of Bose-Einstein condensation of molecules. Phys. Rev. Lett.*, **91**, 1 (2003).

[27] T. Bourdel, L. Khaykovich, J. Cubizolles, J. Zhang, F. Chevy, M. Teichmann, L. Tarruell, S. J. J. M. F. Kokkelmans, and C. Salomon. *Experimental study of the BEC-BCS crossover region in lithium 6. Phys. Rev. Lett.*, **93**, 050401 (2004).

[28] J. Dalibard. *Collisional dynamics of ultra-cold atomic gases.* In M. Inguscio, S. Stringari, and C. Wieman, editors, *Proceedings of the International School of Physics - Enrico Fermi*, pages 321–349 (1999).

[29] M. E. Gehm. *Preparation of an Optically-Trapped Degenerate Fermi Gas of 6Li.* Ph.D. thesis, Duke University (2003).

[30] B. Gänger, J. Phieler, B. Nagler, and A. Widera. *A versatile apparatus for fermionic lithium quantum gases based on an interference-filter laser system. Rev. Sci. Instrum.*, **89**, 093105 (2018).

[31] D. M. Eagles. *Possible Pairing without Superconductivity at Low Carrier Concentrations in Bulk and Thin-Film Superconducting Semiconductors. Phys. Rev.*, **186**, 456 (1969).

[32] A. J. Leggett. *Diatomic molecules and Cooper pairs.* In A. Pkekalski and J. A. Przystawa, editors, *Modern Trends in the Theory of Condensed Matter*, pages 13–27. Springer, Berlin, Heidelberg (1980).

[33] W. Zwerger. *The BCS-BEC Crossover and the Unitary Fermi Gas*, volume 861. Springer, Berlin (2013).

[34] P. Nozières and S. Schmitt-Rink. *Bose condensation in an attractive fermion gas: From weak to strong coupling superconductivity. J. Low Temp. Phys.*, **59**, 195 (1985).

[35] C. A. Sá De Melo, M. Randeria, and J. R. Engelbrecht. *Crossover from BCS to Bose superconductivity: Transition temperature and time-dependent Ginzburg-Landau theory. Phys. Rev. Lett.*, **71**, 3202 (1993).

[36] J. R. Engelbrecht, M. Randeria, and C. A. R. Sáde Melo. *BCS to Bose crossover: Broken-symmetry state. Phys. Rev. B*, **55**, 15153 (1997).

[37] C. A. Sá De Melo. *When fermions become bosons: Pairing in ultracold gases. Phys. Today*, **61**, 45 (2008).

[38] M. W. Zwierlein, J. R. Abo-Shaeer, A. Schirotzek, C. H. Schunck, and W. Ketterle. *Vortices and superfluidity in a strongly interacting Fermi gas. Nature*, **435**, 1047 (2005).

[39] L. Onsager. *Statistical Hydrodynamics. II Nuovo Cimento*, **6**, 279 (1949).

[40] A. Görlitz, J. M. Vogels, A. E. Leanhardt, C. Raman, T. L. Gustavson, J. R. Abo-Shaeer, A. P. Chikkatur, S. Gupta, S. Inouye, T. Rosenband, and W. Ketterle. *Realization of Bose-Einstein Condensates in Lower Dimensions. Phys. Rev. Lett.*, **87**, 130402 (2001).

[41] J. M. Kosterlitz and D. J. Thouless. *Ordering, metastability and phase transitions in two-dimensional systems Related content Long range order and metastability in two dimensional solids and superfluids. J. Phys. C: Solid State Phys.*, **6**, 1181 (1973).

[42] I. Bloch, J. Dalibard, and W. Zwerger. *Many-body physics with ultracold gases. Rev. Mod. Phys.*, **80**, 885 (2008).

[43] L. Bayha, M. Holten, R. Klemt, K. Subramanian, J. Bjerlin, S. M. Reimann, G. M. Bruun, P. M. Preiss, and S. Jochim. *Observing the emergence of a quantum phase transition shell by shell. Nature*, **587**, 583 (2020).

[44] B. Nagler, K. Jägering, A. Sheikhan, S. Barbosa, J. Koch, S. Eggert, I. Schneider, and A. Widera. *Dipole oscillations of fermionic quantum gases along the BEC-BCS crossover in disordered potentials. Phys. Rev. A*, **101**, 53633 (2020).

[45] B. Nagler, M. Radonjić, S. Barbosa, J. Koch, A. Pelster, and A. Widera. *Cloud shape of a molecular Bose-Einstein condensate in a disordered trap: a case study of the dirty boson problem. New J. Phys*, **22**, 033021 (2020).

[46] P. Ring and P. Schuck. *The Nuclear Many-Body Problem.* Springer, Berlin (1980).

[47] P. M. Stevenson. *Optimized perturbation theory. Phys. Rev. D*, **23**, 2916 (1981).

[48] H. Kleinert. *Pfadintegrale in Quantenmechanik, Statistik und Polymerphysik.* Wissenschaftsverlag, Mannheim, Leipzig, Wien, Zürich (1990).

[49] W. Nolting. *Grundkurs Theoretische Physik 6.* Springer, Berlin, 7th edition (2013).

[50] H. Kleinert. *Particles and Quantum Fields.* World Scientific, Singapore (2016).

[51] A. Fetter and J. Walecka. *Quantum Theory of Many-Particle Systems.* Dover Publication Inc., Mineola (2003).

[52] W. Ronalter. *Molekularfeldtheorie von Molekülkondensaten.* Diploma thesis, Universität Duisburg-Essen (2005).

[53] G. Orso. *BCS-BEC crossover in a random external potential. Phys. Rev. Lett.*, **99**, 250402 (2007).

[54] L. Salasnich, N. Manini, and A. Parola. *Condensate fraction of a Fermi gas in the BCS-BEC crossover. Phys. Rev. A*, **72**, 023621 (2005).

[55] H. T. Stoof, D. B. M. Dickerscheid, and K. Gubbels. *Ultracold Quantum Fields*. Springer, Berlin (2009).

[56] S. Giorgini, L. P. Pitaevskii, and S. Stringari. *Theory of ultracold atomic Fermi gases. Rev. of Mod. Phys.*, **80**, 1215 (2008).

[57] H. Korsch. *Mathematische Ergänzungen zur Einführung in die Physik*. Binomi Verlag, Barsinghausen, 4th edition (2007).

[58] A. Pelster. *Bose-Einstein-Kondensation*. Universität Duisburg-Essen (2004).

[59] D. S. Petrov, C. Salomon, and G. V. Shlyapnikov. *Weakly Bound Dimers of Fermionic Atoms. Phys. Rev. Lett.*, **93**, 090404 (2004).

[60] B. Nagler. *Bose-Einstein condensates and degenerate Fermi gases in static and dynamic disorder potentials*. Ph.D. thesis, Technische Universität Kaiserslautern (2020).

[61] F. Schwabl. *Statistische Mechanik*. Springer, Berlin, 3rd edition (2006).

[62] L. D. Carr, G. V. Shlyapnikov, and Y. Castin. *Achieving a BCS transition in an atomic fermi gas. Phys. Rev. Lett.*, **92**, 150404 (2004).

[63] Q. Chen, J. Stajic, and K. Levin. *Thermodynamics of interacting fermions in atomic traps. Phys. Rev. Lett.*, **95**, 260405 (2005).

[64] S. Giorgini, L. P. Pitaevskii, and S. Stringari. *Condensate fraction and critical temperature of a trapped interacting Bose gas. Phys. Rev. A*, **54**, 4633 (1996).

[65] J. Kinast. *Thermodynamics and Superfluidity of a Strongly Interacting Fermi Gas*. Ph.D. thesis, Duke University (2006).

[66] P. Pieri and G. C. Strinati. *Strong-coupling limit in the evolution from BCS superconductivity to Bose-Einstein condensation. Phys. Rev. B*, **61**, 15370 (2000).

[67] M. Ueda. *Fundamentals and New Frontiers of Bose-Einstein Condensation*. World Scientific, Singapore (2010).

[68] W. Weimer, K. Morgener, V. P. Singh, J. Siegl, K. Hueck, N. Luick, L. Mathey, and H. Moritz. *Critical velocity in the BEC-BCS crossover. Phys. Rev. Lett.*, **114**, 095301 (2015).

[69] P. W. Anderson. *Theory of dirty superconductors. Journal of Physics and Chemistry of Solids*, **11**, 26 (1959).

[70] B. Damski, J. Zakrzewski, L. Santos, P. Zoller, and M. Lewenstein. *Atomic Bose and Anderson Glasses in Optical Lattices. Phys. Rev. Lett.*, **91**, 80403 (2003).

[71] J. Billy, V. Josse, Z. Zuo, A. Bernard, B. Hambrecht, P. Lugan, D. Clément, L. Sanchez-Palencia, P. Bouyer, and A. Aspect. *Direct observation of Anderson localization of matter waves in a controlled disorder. Nature*, **453**, 891 (2008).

[72] G. Roati, C. D'Errico, L. Fallani, M. Fattori, C. Fort, M. Zaccanti, G. Modugno, M. Modugno, and M. Inguscio. *Anderson localization of a non-interacting Bose-Einstein condensate. Nature*, **453**, 895 (2008).

[73] A. Aspect and M. Inguscio. *Anderson localization of ultracold atoms. Phys. Today*, **62**, 30 (2009).

[74] M. H. Chan, K. I. Blum, S. Q. Murphy, G. K. Wong, and J. D. Reppy. *Disorder and the superfluid transition in liquid ^{4}He. Phys. Rev. Lett.*, **61**, 1950 (1988).

[75] G. K. Wong, P. A. Crowell, H. A. Cho, and J. D. Reppy. *Superfluid critical behavior in ^{4}He filled porous media. Phys. Rev. Lett.*, **65**, 2410 (1990).

[76] H. Hancock. *Elliptic Integrals.* Dover Publications, Mineola (1958).

[77] I. Gradshteyn and I. Ryzhik. *Table of integrals, series and products.* Academic Press, Cambridge, 4th edition (1985).

[78] E. W. Weisstein. *Polylogarithm.* MathWorld `https://mathworld.wolfram.com/Polylogarithm.html`.

[79] E. W. Weisstein. *Nielsen Generalized Polylogarithms.* MathWorld `https://mathworld.wolfram.com/NielsenGeneralizedPolylogarithm.html`.

Danksagung

Am Ende dieser Arbeit möchte ich nun die Gelegenheit nutzen, um denjenigen zu danken, die mir dabei geholfen haben, diese Arbeit anzufertigen.

In erster Linie danke ich meinen Eltern für ihre bedingungslose Unterstützung während des gesamten Studiums. Sie haben es mir ermöglicht, dass ich mich jederzeit voll und ganz meinem Studium widmen konnte und haben mir bei allen anfallenden Problemen mit ganzer Kraft weitergeholfen.

Mein großer Dank gilt Priv.-Doz. Dr. Axel Pelster, der mir die Gelegenheit gegeben hat, diese Arbeit anzufertigen. Während der gesamten Zeit stand er jederzeit voller Enthusiasmus für Diskussionen zur Verfügung und hat mir die Teilnahme an zahlreichen interessanten Schulen und Konferenzen ermöglicht.

Des Weiteren danke ich Prof. Dr. Artur Widera dafür, dass er diese Arbeit durch die Zusammenarbeit mit seinem Experiment unterstützt hat. Hier sind natürlich auch die gesamten experimentellen Kollegen des Fermi-Labors zu nennen, denen ich ausdrücklich für die Vielzahl an Diskussionen danke, die maßgeblich dazu beigetragen haben, mein Verständnis für die experimentellen Problemstellungen zu verbessern. Besonders danke ich Sian Barbosa und Dr. Benjamin Nagler für das zur Verfügung stellen der experimentellen Daten, die in dieser Arbeit präsentiert und diskutiert werden konnten.

Ich danke außerdem Prof. Dr. Michael Fleischhauer für die Bereitstellung des Büroarbeitsplatzes und der Möglichkeit an seinem Gruppenseminar teilzunehmen, sowie seiner gesamten Arbeitsgruppe für die freundliche und hilfsbereite Umgebung.

Zudem danke ich Enrico Stein für die angenehme Arbeitsatmosphäre in unserem gemeinsamen Büro. Nicht nur bei physikalischen Problemen konnte er mir durch seine Expertise weiterhelfen, er hat sich auch als wahrer Kenner für Tee erwiesen.

Schließlich geht mein Dank an Marcel Burgard, der mir während des gesamten Studiums über beistand und mir dabei geholfen hat, die Laufzeit meiner Python Programme um ein Vielfaches zu reduzieren.

Selbstständigkeitserklärung

Hiermit erkläre ich, dass ich diese Arbeit selbstständig verfasst und keine anderen als die angegebenen Quellen und Hilfsmittel verwendet, sowie Zitate kenntlich gemacht habe.

Kaiserslautern, den 29. März 2021

André Becker